RÉPUBLIQUE FRANÇAISE
Liberté Égalité Fraternité

Université de Toulouse

Doctorat de l'Université de Toulouse

délivré en co-tutelle avec Universidad de Concepción

préparé à Toulouse INP

Site isole-nanoparticules de métal noble supportées sur des nanotubes d'oxyde de titane comme catalyseurs pour la production d'amines aromatiques à partir de l'hydrogénation catalytique de nitroarènes

---

Thèse présentée et soutenue, le 16 mars 2026 par

Edgardo LEAL

École doctorale
SDM - SCIENCES DE LA MATIERE - Toulouse

Spécialité
Chimie Organométallique et de Coordination

Unité de recherche
LCC - Laboratoire de Chimie de Coordination

Thèse dirigée par
Philippe SERP et Cristian Hugo Alberto Campos Figueroa

Composition du jury
Mme Paula OSORIO VARGAS, Rapporteure, Universidad de Talca
M. Cyril GODARD, Rapporteur, Universitat Rovira i Virgili: Tarragona
Mme Catherine SEPULVEDA MUñOZ, Examinatrice, Universidad de Concepción
Mme Sophie HERMANS, Examinatrice, UCLouvain Institut IMCN
Mme Veronica JIMENEZ CURIHUAL, Examinatrice, Universidad Andres Bello
M. Pham Minh DOAM, Examinateur, IMT Mines d'Albi
M. Philippe SERP, Directeur de thèse, Institut National Polytechnique de Toulouse
M. Luis ARTEAGA PEREZ, Co-directeur de thèse, Universidad de Concepcion

Membres invités
M. Cristian Hugo Alberto Campos Figueroa, Universidad Nacional Andres Bello

Universidad de Concepción

Facultad de Ciencias Químicas

Doctorado en Ciencias con mención en Química

Single Site-Nanoparticles of Noble Metal Supported on Titanium Nanotubes as Catalysts for the Production of Aromatic Amines from the Catalytic Hydrogenation of Nitroarenes

Thesis Presented to the Faculty of Chemical Sciences of the University of Concepción in fulfillment of the requirements for the degree of Doctor in Chemical Sciences

Presented by:

EDGARDO ADOLFO LEAL VILLARROEL

Thesis advisors:

Dr. Luis E. Arteaga Pérez, Universidad de Concepción, Chile

Dr. Cristian H. A. Campos Figueroa, Universidad Andrés Bello, Chile

Pr. Dr. Philippe Serp, National Polytechnic Institute of Toulouse, France

Concepción, Chile, 2026

Se autoriza al reproducción total o parcial, con fines académicos, por cualquier medio o procedimiento, incluyendo la cita bibliográfica del documento.

Total or partial reproduction for academic purposes is authorized by any means or procedure, including bibliographic citation of the document.

La reproduction totale ou partielle à des fins académiques est autorisée, par tout moyen ou procédé, y compris la citation bibliographique du document.

To the little child who looked out of the bus
window at the tower clock,
searching for a dream that came true.

ACKNOWLEDGEMENTS

These pages may not be enough to express my gratitude to all the people who supported me throughout this journey. With this thesis, an important path comes to an end. I am deeply grateful to my thesis supervisor and true friend, Dr. Cristian H. Campos, who saw potential in me, trusted in my abilities, and taught me much more than research.

I would like to thank Dr. Philippe Serp for his constant support, guidance, and invaluable contributions to my scientific training, and Dr. Luis Arteaga, who never hesitated to help whenever we needed it. To my three thesis supervisors, thank you very much for all your corrections, advice, and contributions to my development as a researcher, and for helping make this thesis a truly satisfying work.

To my Chilean team Cecilia, Tatiana, Carlos, Mario, John, and María José thank you for your help, your guidance, and for always being available to solve a problem or share a glass in the "operations center". You made every step of the PhD journey a wonderful experience. To Santiago, who never says no to any plan or request even when it meant getting lost in Eastern Europe thank you.

To the French team Matthieu, Eduardo, and Quentin thank you for welcoming me for more than a year, for all your help, and for everything you taught me. I would like to give special thanks to Abbas for all the bizarre conversations and his understanding; to Seema, for being a spectacular friend; and to Clément, my gym bro, colleague, and friend, for all the scientific discussions, after-work moments, and for welcoming me into your home with Céline. Thank you very much for your support in France.

I would also like to dedicate special words to my friend and colleague Dr. Daniela González who made laboratory work an incredibly enjoyable time. Thank you for the partnership, the pasta, the unforgettable trips, and those still to come and for never running out of wine and gossip.

Finally, during these four years, you have been a strong and constant support for me, my beloved Cristian R. I dedicate these words to you for all your help, emotional support, understanding, wisdom, and for always encouraging me to give my best.

Finally, this thesis has not been the same without the economic support, thanks to programa de cooperación cientifica ECOS-ANID 210036 and ECOS Sud-ANID (project ECOS n◦ C21E03), scholarship ANID-Subdirección de Capital Humano/Doctorado Nacional/2022-21220327

TABLE OF CONTENT.

TABLE OF CONTENT. iv
INDEX OF FIGURES. vi
INDEX OF TABLES. xi
I. RESUMÉ xvi
II. RESUMEN xxii
III. ABSTRACT xxvii
1. INTRODUCTION 1
1.1 Single site-based heterogeneous catalysts 1
1.2 Titanium oxide-based support for single site-based catalysts 3
1.3 Single site and nanoparticles cooperative effects in hydrogenation reactions 7
1.4 Building block valorisation via hydrogenation reactions 8
2. HYPOTHESIS AND OBJECTIVES 16
2.1 Hypothesis 16
2.2 Main objective 17
2.2.1 Specific objectives 17
3. EXPERIMENTAL SECTION 18
3.1 Synthesis of supports 18
3.2 Synthesis of the catalysts 18
3.3 Materials characterization 19
3.4 Catalytic evaluation 22
4. RESULTS AND DISCUSSION 26
4.1 Synthesis of the supports 26
4.2 Supports characterization 26
4.3 Synthesis of the catalysts 29
4.4 Catalyst characterization 29
4.5 Catalytic activity assays for NB hydrogenation and reductive amination 36
4.5.1 Nitrobenzene hydrogenation 36
4.5.1.1 Metal loading effect 36
4.5.1.2 Recyclability 39
4.5.1.3 Substituted nitroarenes hydrogenation 44

4.5.2 One-pot synthesis of N-furfurylaniline by reductive amination of nitrobenzene and furfural. 49
4.5.2.1 Metal loading effect 49
4.5.2.2 Complementary characterization 54
4.5.2.3 Proposed reaction scheme 57
4.5.2.4 Recyclability 61
4.5.2.5 Evaluation of substituted nitroarenes in the one-pot reductive animation to produce N-furfurylanilines 64
4.5.3 One-pot synthesis of 3-methyl indole via reductive amination of NB and acetol. 67
4.5.3.1 Effect of Pt metal loading. 67
4.5.3.2 Structure-reactivity correlation of Pt(1.000)/TNT-R in NB reductive amination 70
4.5.3.3 Proposed reaction scheme for NB and AC reductive amination 77
4.5.3.4 Recyclability 81
4.5.3.5 Evaluation of substituted nitroarenes in the one-pot reductive animation to produce 3-methyl-indoles 83
5. CONCLUSIONS. 87
6. SCIENTIFIC PRODUCTION. 90
7. SUPPORTING INFORMATION. 93
8. REFERENCES 118

INDEX OF FIGURES.

Figure 1. Deactivations of heterogeneous metal supported catalyst. Extracted from [15]. 3

Figure 2. Schematic showing the proposed dynamic evolution of Pt_{iso}/TiO_2 catalysts following oxidation, mild reduction and harsh reduction (shown left to right, respectively). Structures were derived from DFT calculations and are consistent with experimental data. Ti, O, Pt and H atoms are blue, red, white and light-pink spheres, respectively. Extracted from [43]. 4

Figure 3. The most favorable adsorption sites for Pt on (a) stoichiometric rutile (110), (b) stoichiometric anatase (101), (c) reduced rutile (110), and (d) reduced anatase (101). Also shown in (e(and (f) are the most favorable geometries for Pt_2 adsorbed on reduced rutile (110) and anatase (101), respectively. The white, red, and light gray circles represent Ti, O, and Pt atoms, respectively. BrO denotes bridging oxygen. Extracted from [50]. 5

Figure 4. Schematic reaction pathways for nitroarenes hydrogenation [19]. Green colour is the direct-route and red colour is the condensation-route. The H_2 addition and H_2O elimination are not included. Extracted from [81]. 9

Figure 5. Schematic reaction pathways for one-pot nitrobenzene and FUR reaction. In dotted square the initial substrate and target furfurylaniline. The H_2 addition and H_2O elimination are not included. Adapted from [101]. 11

Figure 6. Synthesis of 3-ML from NB and Acetol. Self-elaborate. The H_2 addition and H_2O elimination are not included. 14

Figure 7. Synthesis of the different Pt(%)/TNT-R catalyst. 19

Figure 8. Schema of the synthesis of the TNT-C and TNT-R materials. Self-elaboration. 26

Figure 9. HR-TEM of the TNTs, (A) TNT-C micrography, (B) TNT-R micrography, (C) TNT-C internal diameter (D) TNT-R internal diameter; (E) TNT-C external diameter, (F) TNT-R external diameter.....27

Figure 10. N_2 physisorption isotherms at -196°C analysis for TNT-C and TNT-R materials. 29

Figure 11. HR-TEM of the different Pt(%)/TNT-R catalyst. (A) Pt(0.125)/TNT-R. (B) Pt(0.250)/TNT-R. (C) Pt(0.500)/TNT-R. (D) Pt(1.000)/TNT-R. The platinum single sites are indicated in yellow circles.....31

Figure 12. EPR spectra for the as-synthetized materials.....34

Figure 13. FTIR-CO at -80°C for the TNT-C and Pt(0.125)/TNT-R catalyst. 35

Figure 14. NB conversion for Pt(%)/TNT-R catalysts. Reaction conditions: 30°C, 30 mL EtOH, 10 bar H_2, 700 rpm and NB:Pt. 6000:1.....37

Figure 15. Arrhenius plot for the NB hydrogenation over Pt(0.125)/TNT-R catalyst. 30-90°C, 10 bar H_2, 700 rpm, 50 mg of catalyst, 30 mL EtOH, Pt:NB 1:6000. 38

Figure 16. Recyclability of the Pt-based catalysts for the hydrogenation of NB at 180 min. (A) recycles for Pt(0.125)TNT-R and (B) Pt(0.125)/TNT-C. Reaction conditions: mass of

catalysts 0.025 g, 10 bar H_2 pressure, 30°C, 30 mL of ethanol, and stirring speed of 700 rpm and Pt:NB 1:6000. 41

Figure 17. HR-TEM by atomic force microscopy of the used catalyst after the recycling experiment Pt(0.125)/TNT-R. 43

Figure 18. Correlation between log $k_{ap,\ exp}$ and log $k_{ap,\ model}$ for p-substituted nitroarenes hydrogenation on Pt(0.125)/TNT-R catalyst. Conditions: a batch reactor, T = 30 °C, 10 bar of H_2 pressure, 30 mL EtOH, Pt:substrate 1:6000 49

Figure 19. Simplified proposed reaction scheme for the one-pot reductive amination of NB and FUR to produce FFA.....52

Figure 20. FT-IR of absorbed Py for the Pt(0.125)/TNT-C and Pt(0.125)/TNT-R, recording following a brief outgassing of at 150°C. 55

Figure 21. (A) ratio between the LPy acid sites and HPy acid sites in the catalyst, (b) deconvolution of the mix signal of LPy and HPy. (B) IR band position and the relativity intensities (LPy/HPy). 56

Figure 22. Temperature effect over the reaction NB and FUR. (A) Arrhenius plot for the hydrogenation of just NB, NB and FUR, and hydrogenation of the ANI (B) Product distribution at at NB isoconversion = 50% , X_{NB} and X_{FUR} at 360 min employing different temperatures. 10 bar H_2, Pt(0.125)/TNT-R 50 mg, Pt:NB:FUR 1:6000:6000. 59

Figure 23 Recycling experiment for one-pot reductive amination of NB and FUR. The selectivity at isoconversion of 20 %, and conversion of NB and FUR at 180 min of reaction time. Pt(0.125)/TNT-R, 50 mg, 30°C, 10 bar H_2, NB:FUR:Pt 6000:6000:1. 62

Figure 24. (A) High resolution microscopy post recycling test of Pt(0.125)/TNT-R for one-pot reductive amination of NB + FUR to produce FFA and (B) Particles distribution histogram for the HR-TEM characterization. 63

Figure 25. Hammet plot for the study of different p-nitroarenes in the one-pot reaction between NB and FUR, correlation of $\log(k_{ap})$ versus the σ^{+}_{p}. Conditions: a batch reactor, T = 30 °C, 10 bar of H_2 pressure, 30 mL EtOH, Pt:substrate 1:6000, 700 rpm.....67

Figure 26. One pot simplified reaction schema for the synthesis of 3-ML from NB and Acetol. Self-elaboration. 68

Figure 27. Low temperature FT-IR (FT-IR CO) for (A) Pt(1.000)/TNT-R, (B) Pt(1.000)/TNT-C. 71

Figure 28. XPS analyses for the Pt(1.000)/TNT-R (A), (C) and (E) for Pt(1.000)/TNT-C. (B), (D) and (F). 73

Figure 29. FT-IR spectra of adsorbed pyridine (A) Pt(1.000)/TNT-R and Pt(1.000)/TNT-C recording following a brief outgassing of at 150°C. (C-D) IR band position and the relativity intensities (LPy/HPy) 76

Figure 30. Proposed mechanism for the one-pot reaction between NB and AC for the obtention of 3-ML. Adapted from [188]. 80

Figure 31. Recyclability experiments for the system Pt(1.000)/TNT-R. 10 bar of H_2 pressure, 100°C of temperature, 50 mg of catalyst with a molar ratio nitrobenzene/Pt = 1000. 81

Figure 32. (A) High resolution microscopy post recycling test of Pt(1.000)/TNT-R for one-pot reductive amination of NB + AC to produce 3-ML and (B) Particles distribution histogram for the HR-TEM characterization. 83

INDEX OF TABLES.

Table 1. Textural properties of the preparate Pt(%)/TNT-R catalyst. 30

Table 2. Exploratory NB hydrogenation reactions employing Pt(%)/TNT-R catalyst. ...37

Table 3. Values of E_{aa} reported for NB hydrogenation over supported heterogeneous catalyst.....39

Table 4. Influence of water addition in the NB hydrogenation over Pt(0.125)/TNT-R catalyst.....43

Table 5. Kinetic parameters of *p*-substituted nitrobenzenes hydrogenation over Pt(0.125)/TNT-R catalyst. Hammet sigma constant (σ^{+}_{p}) and the solvation free energy of the substrate (ΔG_{sov}) as predictor variables were used from reported data [123]. 45

Table 6. Kinect parameter for the Pt(%)/TNT-R catalysts in the different solvents. 51

Table 7. Kinect parameter for the Pt(0.125)/TNT-R and Pt(0.125)/TNT-C catalysts in the one-pot reductive amination of NB and FUR to produce FFA. 61

Table 8. Kinetic parameters for the one-pot reductive amination of p-substituted nitrobenzenes and FUR to produce p-FFA over Pt(0.125)/TNT-R catalyst. 65

Table 9. Results of the catalytic activity for the obtention of 3-ML from NB and acetol, for the different Pt(%)/TNT-R catalyst. 69

Table 10. High resolution XPS band for Pt, Ti & O for the Pt(1.000)/TNT-R catalyst...72

Table 11. Catalytic data for the obtention of 3-ML from the one-pot synthesis of NB and AC. 79

Table 12. Kinetic parameters for the one-pot reductive amination of p-substituted nitrobenzenes and AC to produce 5,3-ML over Pt(1.000)/TNT-R catalyst. 85

ABBREVIATIONS

In alphabetic order.

SSCs	Single site catalysts
$\Delta G_{solv.}$	Solvation free energy
3-ML	3-methhylindole.
A	Frecuency factor.
AC	Acetol.
AN	Aniline.
ANI	Imine intermediate; furfuryl-N-phenylmethanimine.
APIs	Active pharmaceutical ingredients.
Au_1	Gold single atom.
C_3N_4	Carbon nitride.
CAE	Constant analyzer energy.
CB	Carbon balance.
CNTs	Carbon nanotubes.
DFT	Density functional theory.
D_p	Pore diameter.
e^-	Unpaired electrons.
E_{aa}	Apparent activation energy.
EPR	Electron paramagnetic resonance spectroscopy.
EtOH	Ethanol.
FEG	Field emission gun.
FFA	N-furfurylaniline.
FT-IR	Fourier transform infrared.
FTIR-CO	Fourier transform infrared spectroscopy - CO adsorption.
FTIR-Py	Fourier transform infrared spectroscopy - Pyridine adsorption.
FUR	Furfural.
GC	Gas chromatography.
GC-MS	Gas chromatography-mass spectrometry.

H-NP	Hydrogen on nanoparticle species.
HPy	Protonated pyridine.
HR-TEM	High-resolution transmission electron microscopy.
ICP-OES	Inductively coupled plasma optical emission spectroscopy.
ID	Internal diameter.
IUPAC	International union of pure and applied chemistry.
JCPDS	Joint committee on powder diffraction standards.
k_{ap}	Pseudo-first order rate constant.
LOHC	Liquid organic hydrogen carrier.
LPy	Lewis acid sites.
MeOH	Methanol.
NB	Nitrobenzene.
NM-NPs	Noble metals nanoparticles.
N-PHA	N-phenyl-hydroxylamine.
NPs	Nanoparticles.
O_{1s}	Oxygen 1s spectra.
O_{br}	Oxygen bridging.
O_V	Oxygen vacancies.
Pt	Platinum.
Pt^0	Metalic platinum.
R-NH_2	aryl-amine product.
R-NHOH	N-(aryl)-hydroxylamine intermediary.
R-NO	Nitroso-arene intermediary.
RS	Recyclability stability.
Ru	Ruthenium.
S	Selectivity.
S_{BET}	Surface area calculated by Brunauer, Emmett & Teller method.
SEA	Substitution electrophilic aromatic
STM	scanning tunnelling microscopy.
TEM	Transmission electron microscopy.

THF	Tetrahydrofuran.
Ti_{6C}	Sixfold coordinated Ti.
TiO_2	Titanium dioxide.
TiO_x	Titanium oxide species.
TNT	Titanium oxide nanotubes.
TNT-C	Titania nanotubes control material.
TNT-R	Titania nanotubes partially reduced.
TOF	Turnover frequency.
TPD-NH_3	Temperature programmed desorption – ammonia.
V_p	Pore volume.
X	Conversion.
XANES-EXFAS	X-ray absorption near edge structure/Extended X-ray absorption fine structure.
XPS	X-ray photoelectron spectroscopy.
XRD	X-ray diffraction.
σ^+_p	Hammet sigma positive constant.

I. RESUMÉ

La catalyse hétérogène à base de métaux est essentielle à environ 80 % des procédés de production industrielle, ce qui crée une demande pour des matériaux catalytiques plus efficaces et durables. Étant donné que la plupart des réactions se produisent à la surface des métaux, il est crucial de maximiser le nombre d'atomes métalliques accessibles. Dans ce contexte, les catalyseurs à sites isolés (SSC), composés d'atomes métalliques isolés ou de sites métalliques subnanométriques (moins de 1,0 nm) stabilisés sur des supports, se sont imposés comme une stratégie efficace. Comparés aux catalyseurs traditionnels à base de nanoparticules (NPs), ces catalyseurs permettent une utilisation maximale du métal et une meilleure sélectivité, ce qui se traduit par une efficacité accrue.

L'hydrogénation est un procédé catalytique hétérogène largement utilisé, qui repose sur des NPs pour activer H_2 et faciliter le débordement (spillover) d'hydrogène. Les interactions synergiques entre les NPs et les espèces à atome unique ou à site unique permettent des voies catalytiques difficiles à obtenir avec un système à base de NPs uniquement. Cette coopérativité implique l'activation du H_2 sur les NPs, le débordement d'hydrogène à travers le support pour former des espèces hydrures H-site unique, et la réaction se produisant sur ces sites très actifs et sélectifs.

L'instabilité intrinsèque des atomes et sites métalliques isolés pose un défi majeur en raison de l'agglomération et de la lixiviation du métal. Il est donc nécessaire de disposer d'environnements de coordination robustes pour stabiliser ces atomes et sites dans les SSC. Cette étude s'est concentrée sur des nanotubes de dioxyde de titane (TNT), qui

génèrent des lacunes d'oxygène (O_V) et offrent des effets de confinement grâce à leur structure tubulaire, permettant une stabilisation efficace des sites individuels. Pour augmenter le nombre de lacunes d'oxygène, les TNT ont été réduits par pyrolyse assistée par $NaBH_4$, produisant ainsi des TNT-R. Ce procédé crée des O_V et des défauts Ti^{3+} paramagnétiques, qui forment des sites d'ancrage déficients en électrons pour les précurseurs métalliques. Ces sites stabilisent les atomes de Pt isolés et empêchent leur migration et leur coalescence. De plus, la morphologie tubulaire des TNT offre des effets de nano-confinement qui favorisent une dispersion homogène de la phase active et peuvent faciliter la diffusion des molécules à travers leurs canaux internes.

L'hypothèse centrale de cette thèse est la suivante : *« Les catalyseurs combinant des sites isolés de Pt et des nanoparticules de Pt supportés sur des nanotubes de TiO_2 présenteront une activité, une sélectivité et une recyclabilité accrues dans l'hydrogénation des nitroarènes pour obtenir les amines aromatiques correspondantes, par rapport aux catalyseurs traditionnels principalement constitués de nanoparticules métalliques. La nature chimique des nanotubes et leurs lacunes d'oxygène, ainsi que la charge métallique nominale, contrôleront le rapport site isolé/nanoparticule métallique à la surface du support, ainsi que leurs propriétés catalytiques respectives. »*

Une série de catalyseurs Pt(%)/TNT-R a été synthétisée avec différentes charges métalliques (0.125 % à 1.000 % en poids) afin de contrôler systématiquement la population de sites isolés par rapport aux nanoparticules. Une caractérisation approfondie a confirmé la formation et la stabilisation réussies de la phase active.

La microscopie à force atomique a confirmé que la synthèse a permis d'obtenir la configuration souhaitée d'atomes uniques et de sites uniques. Le catalyseur Pt(0,125)/TNT-R présentait une distribution dominée par des sites uniques de Pt et des amas subnanométriques (< 1.0 nm), tandis que le Pt(1.000)/TNT-R contenait principalement des NPs de Pt plus grandes. L'analyse XPS de l'échantillon Pt(1,000)/TNT-R a révélé la présence d'espèces Ti^{3+} (457.83 eV) et Pt^{2+} (72.29 eV), ce qui soutient la stabilisation des atomes de Pt isolés par coordination avec les défauts du TNT-R.

La spectroscopie RPE a confirmé la présence de défauts dans le TNT-R en montrant un signal fort à g = 1.9797 G, associé à une augmentation des O_V et à la présence de centres Ti^{3+} paramagnétiques. La FTIR-CO à basse température (-80°C) a révélé une bande à 2151 cm^{-1} pour le Pt(0.125)/TNT-R, caractéristique d'espèces $Pt^{\delta+}$ fortement oxydées, confirmant ainsi la formation et l'isolement électronique des atomes et sites de Pt uniques.

Les catalyseurs ont été évalués dans l'hydrogénation du nitrobenzène pour produire de l'aniline. Malgré sa faible charge métallique, le catalyseur Pt(0.125)/TNT-R, contenant à la fois des sites uniques et des NPs, a montré la plus grande activité (TOF: 164 min^{-1}), surpassant le Pt(1.000)/TNT-R, qui contient principalement des NPs (TOF: 44 min^{-1}). Ces résultats confirment la présence d'un effet coopératif entre les sites uniques et les NPs, améliorant ainsi la performance catalytique.

Le mécanisme proposé implique l'activation du H_2 sur les NPs de Pt, suivie d'un débordement d'hydrogène sur le support où l'hydrogénation se produit sur des espèces H–

site unique très actives. La réaction suit une cinétique du pseudo-premier ordre, avec une énergie d'activation apparente de 40.7 kJ mol^{-1} pour le Pt(0.125)/TNT-R. Des tests avec des nitrobenzènes para-substitués ont montré que les groupes attracteurs d'électrons augmentent la vitesse d'hydrogénation, tandis que les groupes donneurs d'électrons la diminuent. Cette forte dépendance électronique indique un intermédiaire limitant la vitesse et déficient en électrons, conforme au mécanisme de Haber.

Les tests de recyclabilité du catalyseur ont révélé une désactivation modérée après réutilisation. La principale cause de désactivation était l'agglomération des atomes et sites de Pt uniques en NPs plus grandes, sans détection de lixiviation du métal lors de l'hydrogénation du nitrobenzène. L'eau produite comme sous-produit de la réaction a favorisé le mûrissement d'Ostwald en éliminant les O_V qui ancrent les atomes uniques, permettant ainsi leur mobilité et leur agrégation en NPs de Pt plus grandes.

La valorisation de la biomasse a été étudiée par la synthèse en une seule étape de la N-furfurylaniline (FFA) à partir de nitrobenzène (NB) et de furfural (FUR), en utilisant un catalyseur Pt(0.125)/TNT-R optimisé. Ce processus implique l'hydrogénation du NB en aniline, la condensation AN/FUR en imine et l'hydrogénation ultérieure de l'imine en FFA. L'analyse FTIR-Py a révélé que le TNT-R possède une concentration plus élevée de sites acides de Brønsted faibles que le TNT-C témoin, améliorant la réactivité du FUR et atteignant une sélectivité maximale en FFA de 66.3 %. Des études à différentes températures n'ont montré aucune compétition entre le NB et le FUR pour les sites d'hydrogénation. Le catalyseur est resté actif jusqu'à six cycles, la désactivation étant

principalement due à l'agglomération des atomes et sites uniques en NPs plus grandes, favorisée par la formation d'eau.

La synthèse du 3-méthylindole (3-ML) a été réalisée par amination réductrice du nitrobenzène et de l'acétol en un procédé en une seule étape, mettant en lumière le défi du contrôle de la sélectivité dans les réactions en cascade. Le catalyseur Pt(1.000)/TNT-R a présenté la plus grande sélectivité en 3-ML, à 55,8 %. Comparé au Pt(1.000)/TNT-C, le TNT-R a fourni les sites acides faibles nécessaires pour promouvoir la cyclisation, tandis que la forte acidité de Lewis du TNT-C a inhibé la réaction en adsorbant fortement l'acétol et en réduisant la formation de 3-ML. Les tests de recyclabilité pour la synthèse du 3-ML ont révélé une désactivation modérée due à l'effet combiné des hautes températures (100°C) et de la production importante d'eau (4 mol H_2O par mol de 3-ML). Ces conditions ont provoqué le frittage du Pt, entraînant une taille moyenne de particule de 7.1 ± 3.6 nm après 10 cycles. Cela confirme que les environnements hydrothermaux générés par la production d'eau sont la principale limitation à la durabilité du catalyseur.

Ces résultats démontrent les avantages de la catalyse coopérative entre atomes/sites uniques et NPs pour l'hydrogénation des nitroarènes et l'amination réductrice en une seule étape d'aldéhydes issus de la biomasse, établissant une méthodologie simple pour la préparation de catalyseurs Pt à sites uniques-NPs supportés sur des TNT à défauts contrôlés. La principale voie de désactivation implique l'agglomération des atomes et sites uniques en NPs plus grandes, ce qui perturbe la coopérativité et réduit le nombre de sites actifs d'hydrogénation. Ce processus est favorisé par la formation d'eau via la solvatation

des O_V. Dans l'ensemble, ce travail promeut l'utilisation de catalyseurs à base de nanotubes de TiO_2 et apporte des éclairages sur le développement de SSC mono- ou bimétalliques recyclables, stabilisés par des lacunes d'oxygène pour les transformations organiques.

II. RESUMEN

La catálisis heterogénea es una de las herramientas más utilizadas en la industria química y petroquímica; se estima que cerca del 80 % de los procesos emplea catalizadores metálicos soportados en al menos una etapa de producción. Dado que la mayoría de las reacciones ocurren en superficies metálicas, es crucial maximizar la cantidad de átomos accesibles a las moléculas reactivas. Los *single sites catalysts* (SSCs) se han consolidado como una estrategia clave para disminuir la carga de metales nobles y mejorar la eficiencia catalítica. Estos se definen como catalizadores heterogéneos donde cada átomo metálico o agregado (< 1.0 nm) se encuentra aislado y disperso en un soporte, ofreciendo mayor utilización del metal activo, alta selectividad y mayores velocidades de reacción que los sistemas convencionales de nanopartículas (NPs). Sin embargo, su inestabilidad intrínseca plantea desafíos asociados al control de la sinterización (efecto Ostwald) y la lixiviación de la fase activa.

Una de las reacciones catalíticas más estudiadas e implementadas industrialmente es la hidrogenación la cual requiere nanopartículas metálicas (NP) para activar el H_2 y posibilitar el fenómeno de *H-spillover*. La cooperatividad del sistema involucra: i) la activación de H_2 en las NP, ii) la formación de H-*spillover* en el soporte y especies H–*single site*, y iii) la reacción catalítica de estas especies con el sustrato, las cuales presentan mayor actividad y selectividad que las especies NP–H.

Para preparar sistemas SSCs–NP es fundamental diseñar un entorno coordinante que estabilice átomos individuales sobre el soporte. Esta investigación se centra en nanotubos

de titanio (TNT) por su capacidad de generar vacancias de oxígeno (O_V) como sitios de anclaje. Las O_V se indujeron mediante la reducción pirolítica con $NaBH_4$, generando defectos como O_V y especies Ti^{3+} en TNT-R. Estos defectos actúan como sitios estables para átomos y SS de Pt, evitando su migración y coalescencia. Además, la morfología tubular favorece el nanoconfinamiento, la dispersión homogénea de la fase activa y la difusión molecular.

La hipótesis central de esta tesis es que "La combinación de sitios del tipo *single sites*-nanopartículas en catalizadores de Pt soportados en nanotubos de TiO_2 elevará la actividad, selectividad y reciclabilidad en la hidrogenación de nitroarenos hacia aminas aromáticas, en comparación con catalizadores constituidos exclusivamente por nanopartículas de Pt. La naturaleza química de los nanotubos de TiO_2 y sus respectivas vacancias de oxígeno, así como la carga metálica nominal, permitirán modular la proporción *single sites*-nanopartículas metálicas en la superficie del soporte determinando sus propiedades catalíticas diferenciadoras"

Se sintetizó una serie de catalizadores Pt(%)/TNT-R con cargas entre 0.125 y 1.000 % en masa. La microscopía de fuerza atómica confirmó configuraciones SSCs–NP: Pt(0.125)/TNT-R presentó predominio de *single sites* y clústeres < 1.0 nm, mientras que Pt(1.000)/TNT-R mostró principalmente NPs > 1.2 nm, el XPS confirmó la presencia de Ti^{3+} y Pt^{2+}, coherente con la estabilización de Pt aislado por defectos del TNT-R. La espectroscopia paramagnética EPR evidenció un aumento de las O_V y Ti^{3+} paramagnético, y FTIR-CO mostró en Pt(0.125)/TNT-R una banda a 2151 cm^{-1} asociada a la coordinación

de CO con especies $Pt^{\delta+}$ altamente oxidadas, el conjunto de técnicas permitió corroborar directa e indirectamente la obtención de la configuración SSCs-NP de Pt.

El catalizador se evaluó en la hidrogenación de nitrobenceno (NB) a anilina (AN). El catalizador Pt(0.125)/TNT-R, que contiene SS y NPs, mostró mayor actividad (TOF: 164 min^{-1}) que Pt(1.000)/TNT-R (TOF: 44 min^{-1}), dominado por NPs, lo que valida el efecto cooperativo entre ambas especies. La reacción siguió una cinética de pseudo-primer orden, con una energía de activación aparente de 40.74 kJ mol^{-1} para Pt(0.125)/TNT-R. La versatilidad del sistema se comprobó con distintos nitrobencenos sustituidos, observándose una marcada dependencia de la velocidad con la naturaleza electrónica del sustituyente: los grupos electrosustractores aceleraron la reacción, mientras que los electrodonadores la disminuyeron. Esta sensibilidad electrónica indica que la etapa determinante de la velocidad involucra un intermediario deficiente en electrones, en concordancia con el mecanismo de Haber.

Las pruebas de reciclabilidad mostraron una desactivación moderada tras siete ciclos catalíticos. La principal causa fue la aglomeración de átomos aislados de Pt en nanopartículas mayores, sin evidencias de lixiviación del Pt durante la hidrogenación del nitrobenceno. Se determinó que el agua generada como subproducto promueve el efecto Ostwald al solvatar las vacancias de oxígeno (O_V) que anclan los átomos aislados, facilitando su movilidad y posterior agregación en nanopartículas de mayor tamaño.

Se evaluó la valorización de compuestos derivados de biomasa (furfural y acetol) mediante un enfoque *one-pot* de aminación reductiva. El sistema Pt(0.125)/TNT-R mostró

el mejor desempeño para la síntesis de N-furfurilanilina (FFA) a partir de NB y furfural (FUR), a través de una secuencia que involucra la hidrogenación de NB a AN, la condensación AN/FUR a imina (ANI) y su posterior hidrogenación a FFA. La caracterización FTIR-Py reveló que Pt(0.125)/TNT-R presenta mayor proporción de sitios ácidos Bronsted débiles (HPy) que el catalizador control Pt(0.125)/TNT-C, dominado por sitios Lewis (LPy) (LPy:HPy = 0.88 vs. 5.85). Esta acidez Bronsted resultó clave para aumentar la reactividad del FUR frente al ataque nucleofílico del AN, alcanzándose una selectividad máxima a FFA del 66.3 %. El efecto de la temperatura indicó ausencia de competencia entre FUR y NB por los sitios de hidrogenación. Además, el catalizador mantuvo actividad hasta seis reciclos, siendo la desactivación atribuida a la aglomeración y colapso de los sitios aislados de Pt en nanopartículas grandes, promovidos por la generación de agua.

En cuanto a la síntesis del compuesto farmacéutico 3-metilindol (3-ML) a partir de NB y acetol (AC), destaca el desafío de controlar la selectividad en reacciones en cascada. El catalizador Pt(1.000)/TNT-R alcanzó la mayor selectividad al producto objetivo (55.8 %). La comparación con Pt(1.000)/TNT-C evidenció diferencias clave en la función del sitio catalítico: la presencia de acidez Bronsted débil (HPy) en Pt(1.000)/TNT-R fue esencial para promover la ciclación hacia 3-ML, mientras que el predominio de sitios Lewis en Pt(1.000)/TNT-C inhibió la reacción al favorecer la adsorción fuerte e irreversible del acetol a través del grupo –OH, reduciendo la conversión a 3-ML. La reciclabilidad mostró una desactivación moderada atribuida a la temperatura (100°C) y a la generación de agua (4 mol H_2O/mol 3-ML), lo que indujo sinterización del Pt (tamaño medio 7.1 ± 1.5 nm

tras 10 ciclos), confirmando la influencia de procesos hidrotermales en la estabilidad del catalizador.

Estos resultados establecen una metodología para obtener catalizadores de Pt SSCs-NP soportados en TNT-R con capacidad para catalizar múltiples reacciones. El estudio confirma las ventajas de la catálisis cooperativa entre *single sites* y NPs en la hidrogenación de nitroarenos y en la síntesis one-pot de aminas aromáticas secundarias a partir de aldehídos derivados de la biomasa. En todos los sistemas, la principal causa de desactivación fue la aglomeración de los single sites en NPs mayores, lo que redujo la cooperatividad y los sitios activos para la movilidad del hidrógeno. Además, el agua formada como subproducto favorece estos procesos mediante la solvatación de las O_V.

Estos resultados representan un avance en el diseño de catalizadores basados en nanotubos de TiO_2 para reacciones de hidrogenación. Se espera que esta información motive el desarrollo de nuevas formulaciones de nanocatalizadores mono- y bimetálicos empleando soportes con estabilización por vacancias de oxígeno (O_V). Este enfoque permitirá producir SSCs utilizando nanomateriales naturales o sintéticos de bajo costo basados en TiO_2, como sistemas prácticos y reciclables para la transformación eficiente y selectiva de moléculas orgánicas de interés.

III. ABSTRACT

Metal-based heterogeneous catalysis is fundamental to around 80 per cent of industrial production processes, creating a demand for more efficient and sustainable catalytic materials. Since most reactions occur on metal surfaces, it is crucial to maximise the number of accessible metal atoms. In that context, single site catalysts (SSCs), consisting of isolated metal atoms or subnanometric metallic sites (less than 1.0 nm) stabilised on supports, have emerged as an effective strategy. Compared to traditional nanoparticle-based catalysts, these catalysts provide maximum metal utilisation and improved selectivity, resulting in higher efficiency.

Hydrogenation is a widely used heterogeneous catalytic process that relies on metal nanoparticles (NPs) to activate H_2 and facilitate hydrogen spillover. Synergistic interactions between NPs and single site species enable catalytic pathways that would be difficult to achieve with only NP system. This cooperativity involves H_2 activation on the NPs, hydrogen spillover through the support to form H–single site species and the reaction occurring on these highly active and selective sites.

The intrinsic instability of isolated atoms and metal sites poses major challenges due to agglomeration and metal leaching. Therefore, robust coordination environments are required to stabilize single sites in SSCs. This study focused on partially reducible titania nanotubes (TNTs), which generate oxygen vacancies (O_V) and provide confinement effects through their tubular structure, enabling the effective stabilization of individual sites. To increase the number of O_V, TNTs were reduced using $NaBH_4$-assisted pyrolysis

to produce TNT-R. This process O_V and paramagnetic Ti^{3+} defects, which create electron-deficient anchoring sites for cationic metal precursors. These sites stabilize isolated Pt atoms and prevent their migration and coalescence. Furthermore, the tubular morphology of the TNTs provides nano-confinement effects that promote the homogeneous dispersion of the active phase and may facilitate the diffusion of molecules through its internals channels.

The central hypothesis of this thesis is "the combination of Pt single site and nanoparticle catalysts supported on TiO_2 nanotubes will exhibit enhanced activity, selectivity, and recyclability in the hydrogenation of nitroarenes to obtain the corresponding aromatic amines, compared with traditional catalysts that are constituted mainly by metal nanoparticles. The chemical nature of the nanotube and its respective O_V, as well as the nominal metal loading, will control the single site-to-metal nanoparticle ratio on the support surface and their respective catalytic properties".

A series of Pt(%)/TNT-R catalysts were synthesized with different metal loadings (0.125 wt% to 1.000 wt%) to systematically control the population of isolated sites to nanoparticles. Comprehensive characterization was performed to confirm the successful formation and stabilization of the dual active phase.

Atomic force microscopy confirmed that the synthesis achieved the desired single site configuration. The Pt(0.125)/TNT-R catalyst exhibited a distribution dominated by Pt single sites and sub-nanometre clusters (<1.0 nm), whereas Pt(1.000)/TNT-R primarily contained larger Pt NPs. XPS analysis of Pt(1.000)/TNT-R revealed Ti^{3+} (457.83 eV) and

Pt^{2+} (72.29 eV) species, which supports the stabilization of isolated Pt atoms through coordination with TNT-R defects.

EPR spectroscopy confirmed the presence of engineered defects in TNT-R by showing a strong signal at g = 1.9797 G, which is associated with an increase in O_V and the presence of paramagnetic Ti^{3+} centres. Low-temperature FTIR-CO (−80°C) revealed a 2151 cm^{-1} band for Pt(0.125)/TNT-R, which is characteristic of highly oxidized $Pt^{\delta+}$ species. This confirms the formation and electronic isolation of Pt sites.

The catalysts were evaluated in the hydrogenation of nitrobenzene to produce aniline. Despite its low metal loading, the Pt(0.125)/TNT-R catalyst, which contains both single sites and NPs, showed the highest activity (TOF: 164 min^{-1}), outperforming the Pt(1.000)/TNT-R catalyst, which mainly contains NPs (TOF: 44 min^{-1}). These results confirm the presence of a cooperative effect between single sites and NPs that enhances catalytic performance.

The proposed mechanism involves H_2 activation on Pt NPs, followed by hydrogen spillover onto the support where hydrogenation occurs on highly active H–single site species. The reaction follows pseudo-first-order kinetics, with an apparent activation energy of 40.74 kJ mol^{-1} for Pt(0.125)/TNT-R. Tests with para-substituted nitrobenzenes showed that electron-withdrawing groups increase the hydrogenation rate, while electron-donating groups decrease it. This strong electronic dependence indicates an electron-deficient rate-determining intermediate, consistent with the Haber mechanism.

Tests on catalyst recyclability showed moderate deactivation upon reuse. The main cause of deactivation was the agglomeration of Pt single sites into larger NPs, while no metal leaching was detected during nitrobenzene hydrogenation. The water produced as a by-product of the reaction was found to promote Ostwald ripening by dissolving O_V that anchor single sites, thereby enabling their mobility and subsequent aggregation into larger Pt NPs.

The valorisation of biomass was investigated through the one-pot synthesis of N-furfurylaniline (FFA) from nitrobenzene (NB) and furfural (FUR), using an optimized Pt(0.125)/TNT-R catalyst. This process involves the hydrogenation of NB to aniline, the AN/FUR condensation to an imine and subsequent hydrogenation to FFA. FTIR-Py analysis revealed that TNT-R possesses a higher concentration of weak Bronsted acid sites than the TNT-C control, enhancing FUR reactivity and achieving a maximum FFA selectivity of 66.3%. Temperature studies revealed no competition between NB and FUR for hydrogenation sites. The catalyst remained active for up to six cycles, with deactivation primarily resulting from the agglomeration of single sites into larger NPs, which was promoted by water formation.

The synthesis of the pharmaceutical scaffold 3-methylindole (3-ML) was achieved through the reductive amination of nitrobenzene and acetol in a one-pot process, which highlights the challenge of controlling selectivity in cascade reactions. The Pt(1.000)/TNT-R catalyst exhibited the greatest 3-ML selectivity, at 55.8%. In comparison to Pt(1.000)/TNT-C, TNT-R provided the weak acid sites required to promote cyclisation,

whereas TNT-C's high Lewis's acidity inhibited the reaction by strongly adsorbing acetol and reducing 3-ML formation.

Recyclability tests for 3-ML synthesis revealed moderate deactivation resulting from the combined impact of high temperatures (100°C) and substantial water production (4 mol H_2O per mol of 3-ML). These conditions caused Pt to sinter, resulting in a mean particle size of 7.1 ± 3.6 nm after 10 cycles. This confirms that hydrothermal environments generated by water production are the main limitation to catalyst durability.

These results demonstrate the advantages of cooperative catalysis between single sites and NPs for nitroarene hydrogenation and the one-pot reductive amination of biomass-derived aldehydes, establishing a simple methodology for preparing Pt single site–NP catalysts supported on defect-engineered TNTs. The main deactivation pathway involves the agglomeration of sites into larger NPs, which disrupts cooperativity and reduces the number of active hydrogenation sites. This process is promoted by the formation of water through the solvation of O_V. Overall, this work promotes the use of TiO_2-nanotube-based catalysts and provides insights into developing recyclable mono- or bimetallic SSCs stabilised by O_V for organic transformations.

1. INTRODUCTION

1.1 Single site-based heterogeneous catalysts

During the last two centuries, catalysis has made a significant contribution to improving quality of life through its applications in the health, environmental, agricultural, and pharmaceutical fields. [1]. Heterogeneous catalytic systems are the most widely applied, as approximately 80% of industrial production processes, corresponding to a global market of around €1 trillion, rely on solid catalysts [2, 3]. Most heterogeneous catalysts are based on metal/metal oxide, and especially noble-metal catalysts. The critical importance of supported catalysis has motivated significant research efforts to better understand catalytic behaviour and to use this knowledge to design and deploy more efficient processes.

In this context and according to the necessity of decreasing the amount of noble-metal employed in the design of heterogeneous metal supported catalyst, the single sites catalysts (SSCs) have recently emerged as novel materials to produce active, selective and recyclable catalysts for a wide range of chemical processes [4]. A SSCs is defined as a heterogeneous catalyst in which each active metal atom or cluster is homogeneously isolated on the support surface [5]. This novel strategy to produce heterogeneous catalysts offers advantages over traditional supported nanoparticle (NP) catalysts. Among several, SSCs offers a maximum utilization of the active metal, enhanced selectivity, increased reaction rates, and reduced metal usage to achieve comparable catalytic performance to traditional heterogeneous metal supported catalyst. This breakthrough has impacted

multiple research areas [6-8], particularly due to SSCs versatility and the potential to use noble metals, which are generally avoided due to their high cost [9].

Despite these advantages, SSCs face significant challenges, primarily associated with the instability of atom- or cluster-deposited configurations, particularly when the catalysts are used in the liquid phase [10, 11]. Isolated metallic atoms or clusters naturally presented unbalanced forces and surface instability, leading to sintering, leaching or poisoning as displayed in Figure 1 [12-15]. Among the typical deactivation pathways, sintering and leaching are the most common processes observed for heterogeneous catalysts operating in the liquid phase. These phenomena are associated with the detachment of the active metal phase from the support, resulting from weak metal-support anchoring and/or insufficient stabilization under prolonged operation at elevated pressure and temperature [16, 17]. Indeed, the restructuring of metallic sites can occur in different ways, principally motivated for the elevated surface energy and the migration and coalescence into large particles via the Ostwald ripening phenomena [18]. In addition, the reorganization due to the modification of the coordination environment can induce the sintering of the single site into metallic NPs leading to a decrease of the catalytic activity [19, 20].

To overcome these disadvantages, considerable research efforts have been directed toward the development of novel, cost-effective, and reproducible methods for the preparation of SSCs, with the aim of enhancing the coordination and stabilization of isolated atoms or single sites through the use of appropriate supports [14, 21, 22].

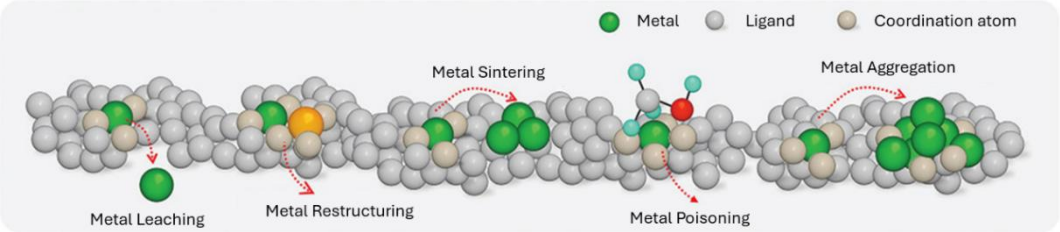

Figure 1. Deactivations of heterogeneous metal supported catalyst. Extracted from [15].

Depending on the synthesis method, these coordination sites often include the use of supports that possess surface stabilizers as carbides [23-25], nitrides [26, 27], hybrid organo-inorganic materials [28, 29] or natural defects-vacancies of the inorganic materials [4, 28, 30]. Thus, the creation of an appropriate coordination environment has emerged as a key consideration in the rational design of single site catalysts, as it represents an effective and economically viable strategy to prevent catalyst deactivation [28, 29, 31]. To this purpose, supports as carbon-based materials [12, 25, 26, 32-35] or partially reducible oxides as TiO_x [20, 32, 36-38] and CeO_x [39-41], among others, enabled the possibility to control the surface chemistry providing adequate environments to the preparation of these type of catalysts.

1.2 Titanium oxide-based support for single site-based catalysts

The titanium oxide-based materials are good candidates for the defect engineering because they provide the possibility to produce TiO_x partially reduced species by different physicochemical treatments [42]. Different authors have reported the use of TiO_x as support and stabilizing agents for single sites active phases. DeRita *et al.* studied by high-resolution microscopy (HR-TEM), Fourier transform infrared spectroscopy (FTIR-CO),

X-ray absorption spectroscopy (XAS) and density functional theory (DFT) calculations, the deposition of Pt in single site configuration, and demonstrated that predilected site for the atomic metal deposition are the defects of TiO_2 anatase like terraces and steps [42]. The characterization and theorical calculation that the Pt atom in mild reduction conditions is stabilized by bonding to two oxygen atoms, also in oxidation media they found that Pt_1 is hosted in the crystalline network by replacing a sixfold coordinated Ti (Ti_{6c}), they argue that varying the treatment conditions a wide range of coordination configuration can be obtained (Figure 2) [43]. Wan *et al.* [44] studied the stabilization of Au_1 single site on TiO_2 nanosheet partially reduced under H_2 flow at different temperatures to induce the generation of O_V defects. The authors achieved a controlled deposition of Au_1 by the formation of Ti-Au-Ti structure. Kropp *et al.* used DFT calculations to show that Pd and Pt can form stable single site species anchored at oxygen vacancies (O_V), with metal binding strength governed by the O_V formation energy of the oxide support. [45].

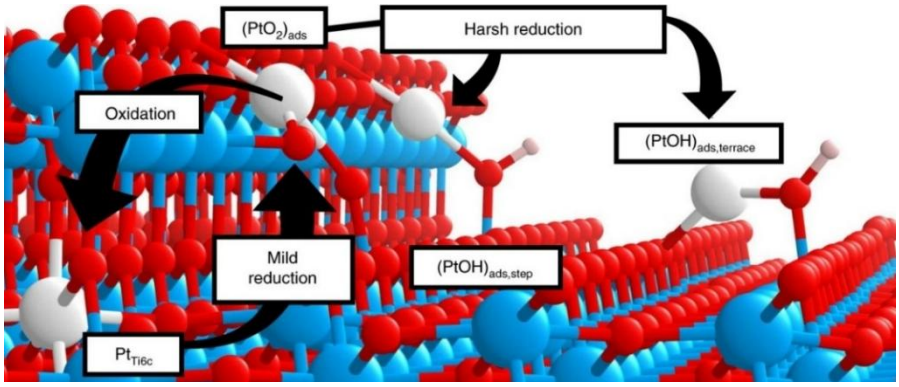

Figure 2. Schematic showing the proposed dynamic evolution of Pt_{iso}/TiO_2 catalysts following oxidation, mild reduction and harsh reduction (shown left to right, respectively). Structures were derived from DFT calculations and are consistent with experimental data. Ti, O, Pt and H atoms are blue, red, white and light-pink spheres, respectively. Extracted from [43].

The O_V formation on TiO_2-based support can be induced and controlled by different physicochemical processes [46-49]. DFT studies have revealed that the most favourable Pt_1 adsorption is the basal O_V generated by the oxygen binding to two Ti atoms bellow the TiO_2 network (called oxygen bridging, O_{br}), located in the subsurface positions relative to the top surface bridging oxygen as illustrated in Figure 3 [50-52]. The Ov has been observed experimentally by scanning tunnelling microscopy (STM) [53, 54], also in the generation of Ov the theory has proven the creations of Ti^{3+} centres or unpaired electrons (e^-), which could lead to the creation of donor levels in TiO_2 electronic structure contributing to the stabilization of Pt_1 [55-57].

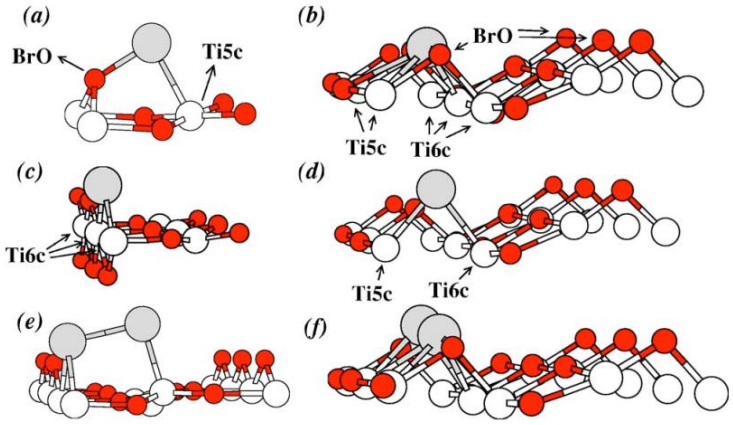

Figure 3. The most favorable adsorption sites for Pt on (a) stoichiometric rutile (110), (b) stoichiometric anatase (101), (c) reduced rutile (110), and (d) reduced anatase (101). Also shown in (e(and (f) are the most favorable geometries for Pt_2 adsorbed on reduced rutile (110) and anatase (101), respectively. The white, red, and light gray circles represent Ti, O, and Pt atoms, respectively. BrO denotes bridging oxygen. Extracted from [50].

It is universally acknowledged that the size/morphology of supports plays an important role in influencing catalytic activity of supported noble metal NPs catalysts [58, 59]. In

this regard, previous reports in our research group, have demonstrated that Pt-based NPs supported on TiO_2 nanotubes support exhibit different catalytic activities with respect to the same metal deposited on TiO_2 particles [20]. This superior catalytic performance can be attributed to the unique "confinement effect" of immobilized noble metal NPs onto nanotubular materials [32, 35]. The nano-confinement effects in nanotubular materials can be understood by the following reasons:

a) Spatial restriction, where the size and shape of NPs can be affected within the nanospace of nanotubes. As a result, NPs can be dispersed there more homogeneously, with a uniform size.

b) Enrichment of molecules: the nanochannels exhibit hydrophobic properties, in addition to the electron-deficient environment. Thus, it can be expected that hydrophobic and nucleophilic molecules will tend to adsorb and accumulate inside the channels.

c) Facilitated diffusion, transport of gas molecules in pores usually follows Knudsen diffusion via collisions with the pore walls. However, when the pore diameter approaches the kinetic diameter of the confined molecules, transport transitions to a configurational (activated) diffusion regime, where molecular motion is strongly influenced by confinement effects and specific molecule–wall interactions.

Currently, TiO_2 nanotubes (TNTs) have been explored to reduce the bandgap of this semiconductor and enable the absorption of visible and infrared radiation by the production of Ti^{3+} and O_V species on the surface of this material. In 2011, Chen *et al.* reported the synthesis of partially reduced titania with a shifted absorption from ultraviolet

to near-infrared due to the introduction of disorder in the surface layers of the nanomaterial after a reduction treatment [60]. Since then, several studies have reported the synthesis of partially reduced TNT under different conditions [61], including the thermal decomposition of sodium borohydride ($NaBH_4$) to generate in situ H_2 and the treatment with noble gases [62, 63]. Both processes lead to surface defects such as O_V and Ti^{3+} centres, which are responsible for the displacement of light absorption to wavelengths > 400 nm. Partially reduced TNT displayed unique advantages make it an ideal material to produce SSCs, combining its intrinsic O_V capacity with the potential of mesoporous materials to produce heterogeneous catalysts in a controlled and sustained manner.

1.3 Single site and nanoparticles cooperative effects in hydrogenation reactions

For hydrogenation reactions, where the limitans step in the reaction consist in the activation of dihydrogen and the rupture of the H-H bond, the metallic Pt present optimal relationship between the metal – H_2 interaction [64-66]. Nevertheless, in the field of metal single site catalysts, the presence of isolated active species with particle sizes below 1.0 nm is not sufficient for hydrogenation reactions. The presence of nanoparticles with particle sizes larger than 1.5 nm is mandatory [67] to chemisorb and dissociate molecular hydrogen, thereby enabling a unique cooperative system [40, 68-70]. The clusters enable the dissociative activation of H_2 and the migration of hydrogen species over the support via the hydrogen spillover phenomenon, facilitated by the presence of single site species. [71, 72]. This intimate relationship between single site species and nanoparticles offers several advantages, including enhanced stability and reduced metal loading in catalytic

formulations, thereby enabling ultrahigh catalytic activities (high TOF) and improved selectivity [73]. The use of single site-NPs system also prevent the poisoning of the catalyst due to the increase of the mobilization of the species on the catalyst surface [74]. SSCs represent a new frontier in catalysis research; however, the high cost, stringent technological requirements for their synthesis, and the need for advanced characterization techniques to unequivocally demonstrate their formation remain significant challenges for the scientific community. [75]. In this thesis, the main objective is to develop a methodology to produce catalysts based on Pt single site-NPs supported on TNTs with increased activity, selectivity and recyclability for catalytic hydrogenation reactions.

1.4 Building block valorisation via hydrogenation reactions

The pharmaceutical industry has focused their efforts on the valorisation of new bio-based building blocks employing environmentally friendly synthetic pathways [76, 77]. Among them, 90% of the synthesis of active pharmaceutical ingredients (APIs) is produced by catalytic process [78, 79]. Aromatic amines and their derivatives are among the most important building blocks in the pharmaceutical industry, with approximately 43% of active pharmaceutical ingredients containing an aromatic amine moiety [80]. The aromatic amines are mainly produced by the hydrogenation of their corresponding nitroarenes. Catalytic hydrogenation of nitroarenes is mediated by a nucleophilic attack to the $-NO_2$ group produced by a hydrogen chemisorbed on a metallic centre [81]. The hydrogenation of nitroarenes can follow two possible routes as shown in Figure 4.

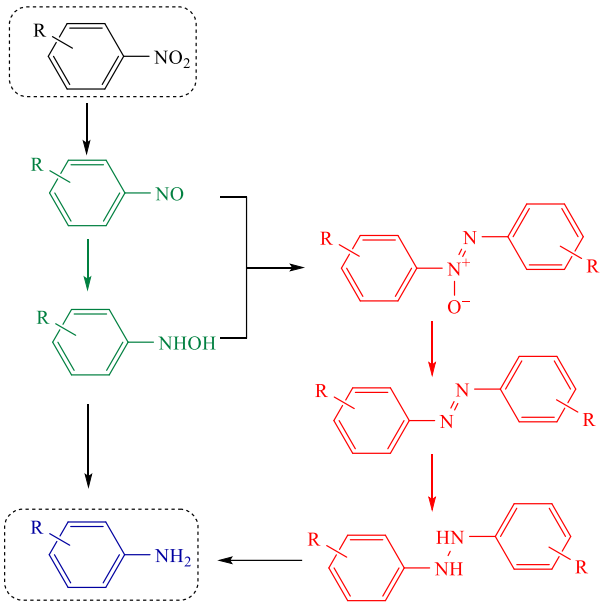

Figure 4. Schematic reaction pathways for nitroarenes hydrogenation [19]. Green colour is the direct-route and red colour is the condensation-route. The H_2 addition and H_2O elimination are not included. Extracted from [81].

The first one corresponds to the direct route (green colour) that takes place mediated by the consecutive formation of the nitroso-arene and N-(aryl)-hydroxylamine intermediaries to give aryl-amine as final product. The second one is called the condensation route that corresponds to the recombination of the nitroso-arene and N-(aryl)-hydroxylamine intermediates to form side products like azo, azoxy and/or hydrazo derivates (red one). In this context, the challenge of the catalytic hydrogenation has been focused in obtaining catalytic systems that operate exclusively through the direct reaction route, able to accelerate the hydrogenation of both nitroso-intermediary (R-NO) and N-(aryl)-hydroxylamine intermediary (R-NHOH) to produce the aryl-amine product (R-NH_2), with the highest yields and selectivity. In the other hand, over-hydrogenation could lead to the

hydrogenation of the aromatic ring, losing the aromaticity of the molecule. This issue becomes more pronounced for substituted nitrobenzene derivatives, which contain additional functional groups susceptible to hydrogenation or hydrotreatment of the substituents [82, 83].

In the recent years, to improve the atom economy and produce "green and efficient" industrial process, the one-pot synthesis is defined as a *"strategy to improve the efficiency of a chemical reaction, whereby a reactant is subjected to successive chemical reactions in just one reactor"* [84, 85]. In this way, one-pot synthesis eliminates batchwise operations and significantly reduces the number of separation-reaction-purification cycles, thereby minimizing material losses, an especially important advantage when dealing with high-value products, such as those in the pharmaceutical industry.

The use of product derived from biomass valorisation by hydrogenation-coupled process such as furfural (FUR) [86] and acetol (AC) [87, 88] has gained significant attention due to their role as versatile platform molecules in the synthesis of more complex chemicals. These compounds act as strategic building blocks for the development of corresponding high-value aromatic amines-based compounds with applications across diverse industrial sectors, including pharmacology [89-93], solvents [90], energetic [94] and specialty chemicals [91, 95, 96].

The N-furfurylaniline (FFA) is a key intermediate with broad applications in pharmaceutical, agriculture and fine chemistry [97]. The classical approach to preparing FFA is the reductive amination of aldehydes employing aniline and H_2 like reductant in

flow heterogeneous catalytic systems [86, 98-100]. The use of nitrobenzene (NB) as a nitrogen source allowed to generate a new approach in batch chemistry, decreasing the reaction condition and the complexity of the process, opening a pathway to the catalytic synthesis of secondary amines. In the reductive amination, the coupling of the amine with FUR and the H_2 activation are crucial for promoting secondary amine formation. It has been reported that zero-valent metal species serve as the active sites for hydrogen activation, while electronically deficient metal species ($M^{\delta+}$) enhance catalytic activity in reductive amination by promoting the hydrogenation of the corresponding imine intermediate, as shown in Figure 5 [98, 101].

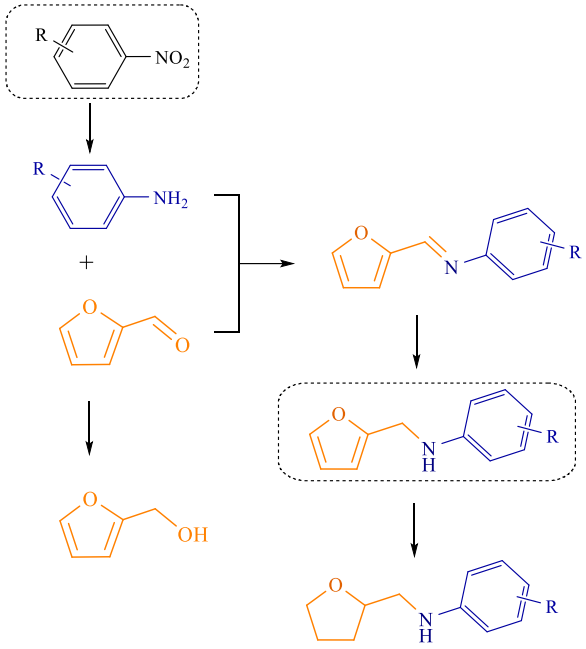

Figure 5. Schematic reaction pathways for one-pot nitrobenzene and FUR reaction. In dotted square the initial substrate and target furfurylaniline. The H_2 addition and H_2O elimination are not included. Adapted from [101].

The one-pot production of FFA from NB and FUR involve the selective hydrogenation of NB to produce aniline (AN) followed by the condensation of FUR and AN to produce the (E)-1-(furan-2-yl)-N-phenylmethanimine (INA), which is further hydrogenated to produce FFA. However, this process is not straightforward as it also involves undesired reactions such as the hydrogenation of FUR to produce furfuryl alcohol, 2-methyl-furane, among others or the over-hydrogenation of FFA to produce aliphatic derivates such as N-tetrahydrofurfurylaniline, N- tetrahydrofurfuryl-cyclohexylamine or others.

The one-pot synthesis of FFA from NB and FUR has not yet been widely reported under mild experimental conditions of temperature and pressure [102], whereas the conventional and extensively studied approach involves batch reactions in the liquid phase using aniline and FUR as reactants [103-105]. Accordingly, the evaluation of a one-pot strategy starting from NB and FUR is presented as a novel route for the production of FFA. Singh *et al*. [103] investigated the synthesis of furfurylaniline over Pd catalysts supported on carbon nanotubes (CNTs), Al_2O_3, and hydrotalcite using a hydrogen-borrowing approach, in which formic acid was employed as the hydrogen source. All catalysts contained Pd NPs and, when operated at 120°C (1 mmol FUR, 1 mmol AN, 1 wt.% Pd, 50 mg catalyst) in methanol, they achieved complete substrate conversion with 100% selectivity toward furfurylaniline. The Pd/CNTs catalytic system exhibited the best catalytic performance, which according to the authors was due to its acid properties. In another study, Subha *et al.* [104] explored the one-pot approach employing FUR and benzylamine as the N source under ambient conditions (1mmol of FUR). They observed that a bimetallic catalyst $PdNi/Nb_2O_5$ reach the 98% of conversion of FUR with near 100% of selectivity to the

secondary amine. The authors attributed the high catalytic performance to electronic effects arising from charge transfer between Pd and Ni, and further demonstrated that the catalyst exhibited versatility toward a range of furfural and benzylamine derivatives. Fernández *et al*. [105] investigated the synthesis of N-furfurylaniline from FUR and aniline over a bifunctional $Pd/ZrO_2–TiO_2$ catalyst under low H_2 pressure. They demonstrated that partial substitution of Ti by Zr modifies the acidity of the catalyst, which plays a key role in the reaction by promoting adsorption of the imine intermediate on Lewis's acid sites. However, the performance of single site catalysts, as compared to NP-based systems, has not yet been explored for the one-pot synthesis of N-furfurylaniline. Given their tuneable metal coordination environment, single site catalysts emerge as promising candidates for achieving high activity and selectivity under mild reaction conditions.

The 3-methylindole (3-ML) is distinguished by its extensive range of applications in the field of medicine, functioning as a highly sought-after pharmacophore, against a variety of drugs like antibiotics, analgesics, antidiuretics, anti-inflammatory, anticancer drugs and so on [106-113]. 3-ML is traditionally obtained by Fischer synthesis, using radical chemistry reactions, coupling cyclization, among others [114-116]. Few studies have shown that catalytic vapor- and liquid-phase syntheses are the most employed strategies for producing 3-ML from AN and glycerol. [117-120]. In this context, heterogeneous catalysis and liquid phase one-pot reductive amination of AC and NB is an economic and environmentally friendly approach to produce 3-ML employing renewable resources. AC is a valuable product generated as a secondary product of the biodiesel industry [121]. The

implementation of a one-pot synthesis employing NB and AC in a one-pot reaction (Figure 6) is scarcely reported previously, making it a novel strategy and opening a new front in 3-ML research.

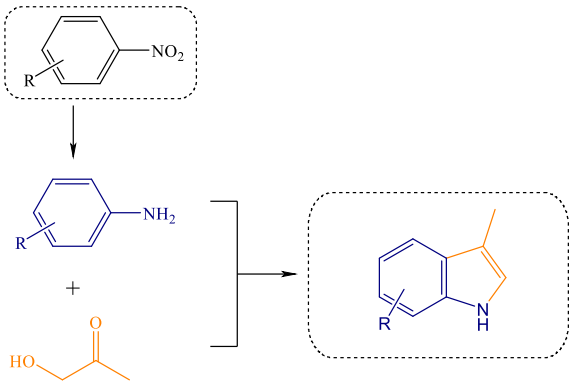

Figure 6. Synthesis of 3-ML from NB and Acetol. Self-elaborate. The H_2 addition and H_2O elimination are not included.

It has been shown that heterogeneous catalytic systems comprising metals such as Cu, Zn, Ni and Co, supported on various supports, are effective in facilitating this type of reaction under harsh reactions conditions [122]. Therefore, the development of active and selective catalysts that operate stably under mild reaction conditions is essential for the environmentally friendly synthesis of 3-ML. In this context, single site catalysts, in which metals are dispersed as isolated atomic species, have emerged as promising materials due to their high atom efficiency and potential for one-pot synthesis.

Based on the above considerations, this thesis aims to develop active and stable single site catalysts for application in hydrogenation and one-pot reductive amination reactions of biomass-derived platform molecules. Based on the literature survey, TNTs were identified

as a promising support for Pt due to their high O_V density, redox properties, intrinsic acidity, and favourable textural characteristics.

A major limitation of conventional preparation methods is the simultaneous formation of Pt single sites and nanoparticles, which complicates the establishment of clear structure-reactivity relationships and hinders mechanistic understanding. To address this issue, partially reduced TNTs (TNT-R) were employed as support for stabilizing Pt single site species, primarily through H_2-assisted thermal reduction of Pt precursors. This work focuses on the strict control of preparation conditions to tune the relative population of Pt single sites and NPs. Accordingly, catalysts with Pt loadings ranging from 0.125 to 1.0 wt.% were synthesized to identify the optimal metal composition. Comprehensive structural and morphological characterizations were conducted to correlate catalyst properties with catalytic performance. Hydrogenation and one-pot reductive amination reactions toward high-value chemicals were used as probe reactions to evaluate and optimize activity and selectivity. In addition, catalyst recyclability was assessed over at least five consecutive reaction cycles to verify stability and recoverability. This systematic approach enabled the evaluation of potential synergistic effects between Pt single sites and nanoparticles in governing the enhanced catalytic performance of the proposed systems.

2. HYPOTHESIS AND OBJECTIVES

2.1 Hypothesis

The combination of Pt single site and nanoparticle catalysts supported on TiO_2 nanotubes will exhibit enhanced activity, selectivity, and recyclability in the hydrogenation of nitroarenes to obtain the corresponding aromatic amines, compared with traditional catalysts that are constituted mainly by metal nanoparticles. The chemical nature of the nanotube and its respective oxygen vacancies, as well as the nominal metal loading, will control the single site-to-metal nanoparticle ratio on the support surface and their respective catalytic properties.

2.2 Main objective

To design of Pt-based catalysts supported on TNTs with tailored populations of single site and NP species, and to evaluate their catalytic performance and stability in the hydrogenation of nitroarenes and one-pot synthesis of aromatic amines

2.2.1 Specific objectives

(i) To develop Pt-based catalytic systems supported on TNTs with controlled populations of single site species and NPs.

(ii) To systematically analyse the physicochemical properties of the prepared catalysts to establish clear structure–activity relationships.

(iii) To evaluate the catalytic performance and operational recyclability of the most active catalyst in nitrobenzene hydrogenation under optimized reaction conditions.

(iv) To assess the capability of the best-performing Pt-based catalysts to produce aromatic amines of pharmaceutical interest through one-pot hydrogenation and reductive amination of nitroarenes with biomass-derived aldehydes, such as acetol and furfural.

3. EXPERIMENTAL SECTION

3.1 Synthesis of supports

Titania nanotubes were synthesized following the previous reported procedures [123]. In a typical synthesis 1.25 g of anatase TiO_2 was dispersed in 63 mL of freshly prepared NaOH 10 $molL^{-1}$ solution. After dispersion, the solution was treated in a hydrothermal reactor at 110°C for 24 h. Then, the solid recovered by filtration and washed with deionized water to neutral pH. Thereafter, the remaining solid was redispersed in HNO_3 a solution (0.1 mol L^{-1}) for 24 h and filtrated again. The obtained material was dried at 110°C for 12 h and calcinated under synthetic air to 300°C for 1h (30 mL min^{-1}, 10°C min^{-1}). The material was labelled as TNT-C.

To generate partially reduced TNT-R and induce the desired defects in TNT-C, pristine TNT-C was subjected to pyrolysis and in situ reduced by $NaBH_4$ [36, 56, 124]. Firstly, the TNT-C and $NaBH_4$ were mechanically mixed (50:50 w/w) to generate a solid solution which was pyrolyzed for 1 h at 300°C under N_2 flow (30 mL min^{-1}, 10°C min^{-1}). The resultant solid was washed with degasified water-acetone mixture (50:50 v/v) five times or until no more hydrogen was released from the remaining $NaBH_4$. The remaining solid was labelled as TNT-R.

3.2 Synthesis of the catalysts

Platinum (II) acetylacetonate was used as metal precursor which was impregnated onto TNT-C or TNT-R, for catalysts preparation. In a typical synthesis, 1.00 g of freshly prepared TNT-C or TNT-R was impregnated with a solution of platinum (II)

acetylacetonate in 100 mL of degassed acetone, using the appropriate precursor amount to obtain Pt loadings of 0.125, 0.250, 0.500, and 1.000 wt.%. Then, the mixture was sonicated for 1 h and the solvent evaporated. Finally, the solid was dried overnight at 50°C and subject thermal reduction treatment under H_2 at 150°C (30 mL min^{-1}, 10°C min^{-1}) to obtain the catalyst as resumed in Figure 7. As control catalysts, Pt(%)/TNT-C was prepared for the systems containing 0.125 and 1.000 %wt. of metal loading following an wet impregnation of the metal precursor in acetone and reduced to the similar temperature in order to avoid the well-known strong metal support interaction (SMSI) effect [125, 126] that can perturb the electronic nature of the control catalysts in compares with the proposed Pt(%)/TNT-R systems.

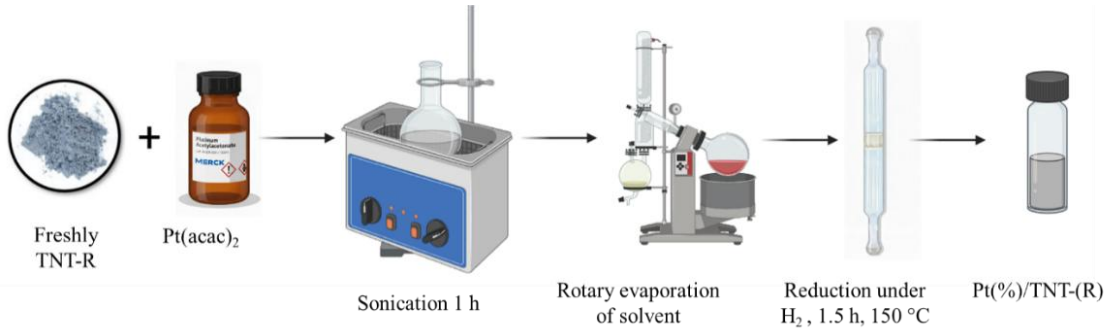

Figure 7. Synthesis of the different Pt(%)/TNT-R catalyst.

3.3 Materials characterization

To measure the specific surface area (S_{BET}) and porosity of the prepared materials, N_2 physisorption measurements at -196°C were conducted. Prior to the analysis, all the samples were heated under N_2 flow at 120°C for 2 h. The analysis was carried out using a

Micromeritics® Tristar II (Micromeritics Instrument Co., Norcross, GA, USA) the adsorption-desorption isotherms was constructed with 42 points in a range of pressure 0.33 - 0.98 p/p^0, the Brunauer–Emmett–Teller (BET) was employed to calculate the specific surface. For pore volume BJH adsorption t plot was used.

The metal content was measured by inductively coupled plasma optical emission spectroscopy (ICP-OES). A Thermo Scientific® ICAP 6300 was employed, after mineralization of the samples in a mixture of HNO_3/HCl at 190°C in an inert autoclave for one day.

High resolution spectroscopy was used for the identification of atomic platinum species, a JOEL-ARM200F cold, equipped with a field emission gun (FEG) working at 200 kV, with a punctual resolution superior to 1.9 Å. For the processing of the micrograph the program ImageJ was employed, the distribution of particle size was determined by manual counting > 300 particles and 10 different pictures. The TEM results were used to calculate the metal dispersion according to the equation 1 [127]. All the analysis were performed at Raimond Castaing micro characterization center, Toulouse, France.

$$D_{TEM}(\%) = \frac{1.01}{d_{TEM}(nm)} \times 100 \quad (1)$$

where D corresponds to the ratio of the number of surface metal atoms to the total number of metal atoms, d_{TEM} is the average particle size determined from TEM images and 1.01 is the geometric factor for platinum relating particle volume to surface area, derived assuming spherical metal nanoparticles.

The Raman spectra was obtained from a Micro-Raman apparatus, Una Labram HR800 Jobin Yvon equipped with a laser λ:532 nm as excitation fount, with a maximum intensity of 7 mW.

Powder XRD patterns were acquired using Cu Kα1 radiation (λ = 1.5418 Å) with a Rigaku diffractometer (Rigaku, Tokyo, Japan). A range of angles from 2θ = 20◦ to 90◦ analysis was performed at the Centre for Applied Economic Geology at the University of Concepción, Chile.

Electron paramagnetic resonance (EPR) spectroscopy was studied in a Bruker EMX spectrometer operating in the X-Band (frequency ~ 9.5 GHz), with a QE Cavity. The sample was disposed of around 50 mg in the tube, and the experiment was performed at ambient temperature. The optimized parameter the centre field a 3200 G, with a Sweep Wide 6000 G, 90 s of Sweep time, with a gain of 40 dB, amplitude of 10 and 10 scan by measure.

X-ray photoelectron spectroscopy (XPS) was recorded in a Thermo Fischer® Electron Kα apparatus with a base pressure of $5x10^{-9}$ mbar, the incident photon energy was 1487 eV (Al Kα). For high resolution acquisition, the analyser was set in CAE mode with pass energy of 20 eV. The data processing and fitting adjustment was due to CASA XPS software. Due to the low percentage of platinum, only for the Pt(1.000)% catalyst was successfully recorded.

Pyridine adsorption was studied to identify the nature of acid sites using a Nicolet iS10 Thermo Scientific Fourier transform infrared (FTIR) spectrometer in diffuse reflectance

mode. The samples were pretreated at 250°C for 12 hours under vacuum conditions, then cooled to 150°C and the reference spectrum was taken. Subsequently, the pyridine was brought into contact with the sample for 10 minutes until saturation of the surface is reached. Thereafter, desorption measurements were carried out at three temperatures (150, 250 and 350°C) using 30 min equilibrium at each temperature.

The CO adsorption at low temperature (-80°C) was studied in a transmission cell with KRS-5 windows coupled to a Nicolet iS50 FTIR spectrometer equipped with a DTGS detector. The sample was activated in situ at 100°C (5°C min^{-1}) under a H_2 gas flow (30 mL min^{-1}) for 30 min. Subsequently, the cell was evacuated to 10-4 mbar in dynamic vacuum at the same activation temperature for 1h. Finally, the temperature was lowered to -80°C and the CO was dozed. The spectra were collected continuously during the adsorption and desorption of CO. The Omnic 9.1® software was used to process the spectra.

The FTIR and CO FTIR experiments were carried out under cooperation with the professor Marcelo Domine at the chemistry technological institute at Polytechnique University of Valencia, Spain.

3.4 Catalytic evaluation

The catalytic assays of hydrogenation and one-pot reductive amination were performed in a stainless steel (150 mL) Parr-type batch reactor. The experiments were carried out in a kinetically-controlled regime, which was confirmed by the Mears and Weiss-Prater criteria [128]. In a typical experiment, the catalyst, solvent, and substrate were loaded into

the reactor and stirred under a He atmosphere until the reaction temperature was reached. Subsequently, the He flow was switched to H_2 and the reaction pressure was set, considering this as t = 0. No catalytic activity for pure TNT-C and TNT-R and without catalyst were confirmed during blank tests. Concentration vs time curves for reactants and products were constructed by taking aliquots of the reaction mixture at specific times, which were analysed *ex situ* by gas chromatography coupled to mass spectrometry and flame ionization detectors (FID). The analytical quantification was carried out in a GC Nexis GC-2030 equipped with a capillary column: Rtx-5 Amine, 30 m, 0.53 mm ID, 3.00 μm, using He as carrier gas and a FID detector. The unknown products were identified by GC-MS in equipment Nexis GCMS-QP2020 NX employing the same column and gas carrier. The variation in the concentration of the reactants and products was determined from calibration curves previously made with standards of compounds. The conversion (X) and selectivity (S) were calculated according to the Eqs. 2 and 3.

$$X_{substrate} = \left(\frac{[Substrate]_0 - [Substrate]_t}{[Substrate]_0} \right) \cdot 100\% \quad (2)$$

$$S_{product} = \left(\frac{[Product]_t}{\sum [Product]_t} \right) \cdot 100\% \quad (3)$$

The turnover frequency (TOF) of the catalyst was calculated according to Eq. 4 [129]:

$$TOF(min^{-1}) = \frac{k_{ap} * n_{product}}{n_{Pt} * D} \quad (4)$$

where k_{ap} is the pseudo-first order rate constant (min^{-1}), $n_{product}$ is the total number of moles of the target product produced, n_{Pt} is the number of Pt moles in each catalysis charge and D is the dispersion calculated by TEM analysis.

The carbon mass balance (CB) was determined for FUR [130] according to the Eq. 5:

$$CB(\%) = \frac{\left(\sum n_i + n_{FUR,t}\right)}{n_{FUR,0}} \quad (5)$$

where n_i are the moles of the FUR-based products, $n_{FUR,t}$ are the mol of unreacted FUR at the time (t) corresponding to the maximum of conversion, and $n_{FUR,0}$ correspond to the initial moles of FUR.

The kinetics of all the reaction systems was determined by a pseudo-first order power law Eq. 6, while the effect of temperature was computed by determining the apparent activation energy (E_{aa}) using the Arrhenius expression Eq. 7:

$$\frac{dC_i}{dt} = -k_{ap} * C_i \quad (6)$$

$$\ln k_{ap} = \ln A - \frac{E_{aa}}{R} * \left(\frac{1}{T}\right) \quad (7)$$

where A is the frequency factor, E_{aa} is the apparent activation energy (kJ/mol), T is the reaction temperature (K), R is the universal gas constant (8.31 J/mol/K) and C_i is the concentration of the substrate.

The recyclability of the catalyst exhibiting the best performance was evaluated by testing its activity over consecutive reaction cycles. After each run, the catalyst was recovered by filtration, washed twice with the solvent to remove adsorbed organic species, and reused in the subsequent cycle. The spent catalysts were characterized to investigate leaching, sintering, and other deactivation phenomena.

4. RESULTS AND DISCUSSION

4.1 Synthesis of the supports

The TNTs were successfully prepared according to the procedure described in the EXPERIMENTAL SECTION and resumed in the Figure 8. The material show a change of colour from white to light blue attributed to the reduction of the Ti^{4+} to Ti^{3+} species [131]. The material was characterized by HR-TEM and N_2 physisorption analysis to assure the obtention of nanotube structure before and after the pyrolysis treatment.

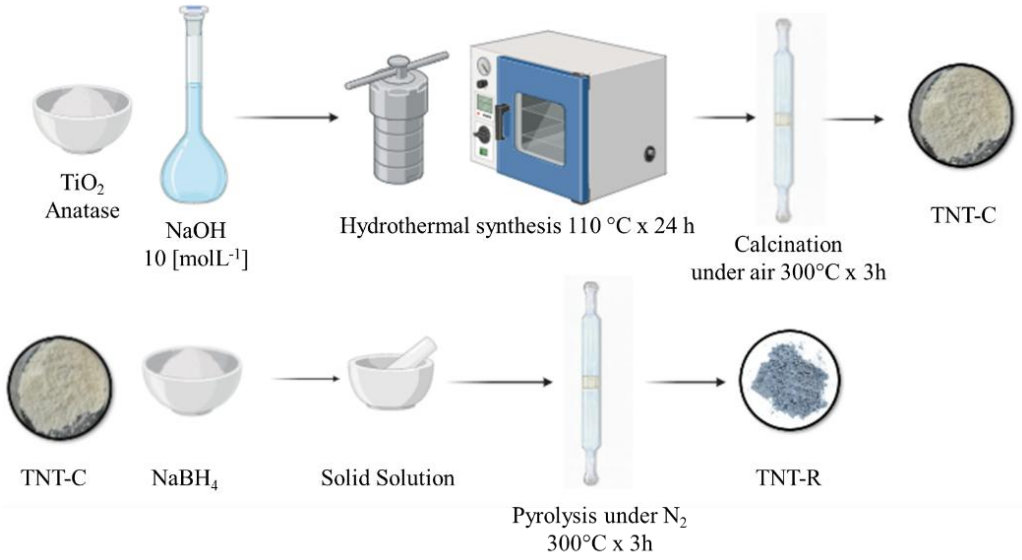

Figure 8. Schema of the synthesis of the TNT-C and TNT-R materials. Self-elaboration.

4.2 Supports characterization

The result of the HR-TEM analysis is shown in Figure 9 for TNT-C and TNT-R. Morphology of the TNT-C system displayed a well-defined tubular structure with average

internal diameter of 4.03 ± 1.20 nm and external diameter of 4.91 ± 1.31 nm (Figure 9A, C and D).

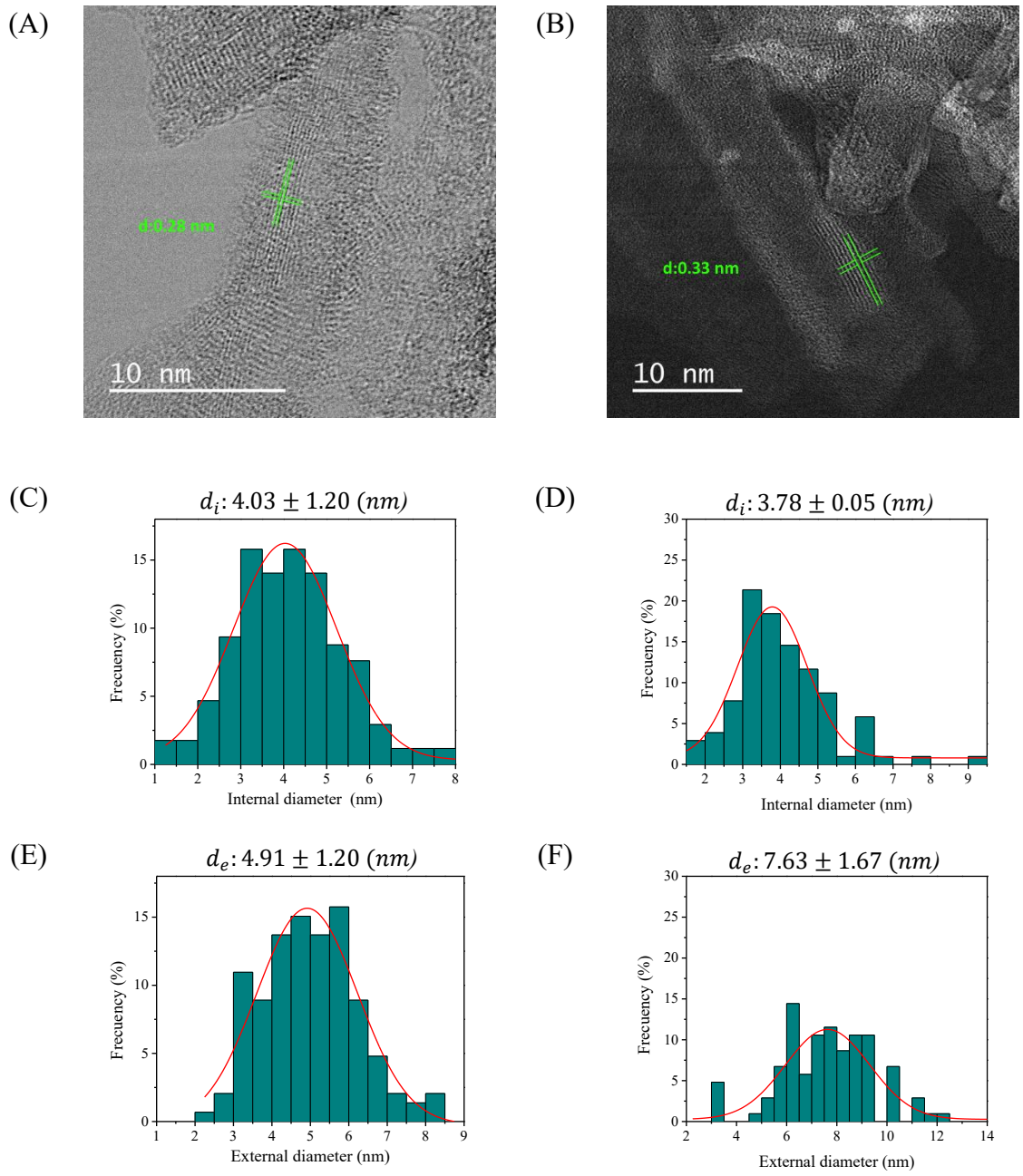

Figure 9. HR-TEM of the TNTs, (A) TNT-C micrography, (B) TNT-R micrography, (C) TNT-C internal diameter (D) TNT-R internal diameter; (E) TNT-C external diameter, (F) TNT-R external diameter.

No remains of TiO_2 NPs were detected in the micrograph, thus proving the high yield of TNT-C. In addition, the micrographs demonstrate that the pyrolytic treatment with $NaBH_4$ does not destroy the tubular nanostructure of the TNT-C. The major changes after the pyrolytic treatment are the modification in the tube diameter (Fig 9 D and F), decreasing the internal diameter to 3.78 ± 0.05 nm whereas the external diameter increased to 7.63 ± 1.67 nm. Moreover, an increment of the interlaminar space from 0.26 nm to 0.33 nm is detected, which is in line with production of TiO_2 anatase phase [38, 132, 133]. These results are in line with Tan *et al.* [62] who found that over 50 min and 300°C the layer of TiO_2 become thicker due to the loss of the crystallinity on the surface **(**~ 1nm).

To complement the HR-TEM results, N_2 physisorption at −196 °C was carried out for both supports as displayed in Figure 10. The TNT-C and TNT-R showed a typical type IV isotherms according to the IUPAC classification, corresponding to a mesoporous material with cylindrical pores. The hysteresis loop revealed the existence of large pores that are not being filled and intermediate mesopores of H1 and H3 types [123]. The TNT-C support displayed a specific area calculated from the BET method of 397 $m^2\ g^{-1}$, with an average pore diameter of 9.20 nm determined from the BJH method, and a total pore volume of 0.99 $cm^3\ g^{-1}$ measured at $P/P^0 = 0.99$. However, the TNT-R displayed a S_{BET} of 276 $m^2 g^{-1}$, a pore diameter to 6.23 nm and total pore volume of 0.44 $cm^3\ g^{-1}$ attributed to the reduction treatment, which agrees with the evidence of the constriction of the nanotube's walls detected by HR-TEM. The textural properties of supports were considered appropriate to proceed with the incorporation of single sites and NPs of Pt to produce

different catalytic systems, which will be further applied in hydrogenation and reductive amination reactions.

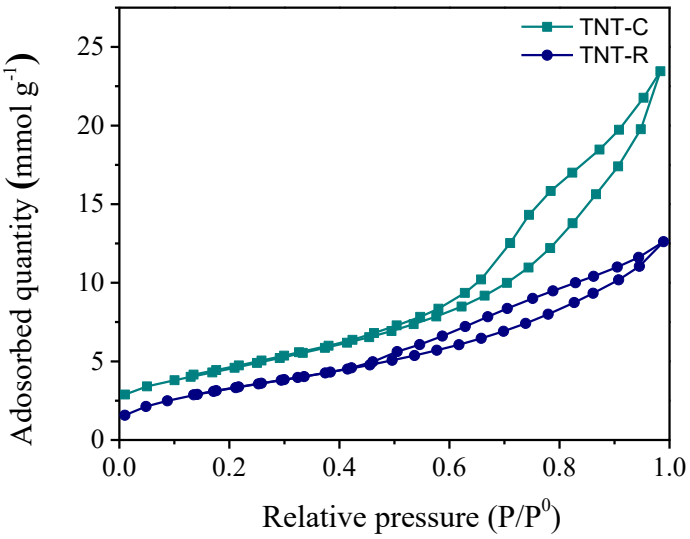

Figure 10. N_2 physisorption isotherms at -196°C analysis for TNT-C and TNT-R materials.

4.3 Synthesis of the catalysts

The ability of the TNT-R to support Pt in single site configurations was tested by preparing 4 catalysts containing different ratios of platinum single site and NPs. These ratios were tuned by changing the metal loadings during catalysts synthesis.

4.4 Catalyst characterization

The metallic content of all the catalyst was determined by the ICP-OES, and it confirmed the nominal values calculated by mass balance during the synthesis (Table 1).

The formation of the Pt single site and NPs onto catalysts surfaces was inspected by HR-TEM analysis as shown in Figure 11. The particle size was determined as the length of the segment connecting the two ends of a particle and passing through its mass centre. The mean particle size, obtained from the statistical distribution of particle counts in TEM images (d_p, TEM), is reported in Table 1 along with textural, compositional and structural properties of the four catalytic systems.

Table 1. Textural properties of the preparate Pt(%)/TNT-R catalyst.

Catalyst	%Pt ICP	d_p HR-TEM (nm)	S_{BET} (m^2g^{-1})	D_p (nm)	V_p (cm^3g^{-1})	D_{TEM}[b] (%)
Pt(0.125)/TNT-R	0.108	0.93 ± 0.47	266	9.7	0.7	100[a]
Pt(0.250)/TNT-R	0.204	1.30 ± 0.60	276	9.5	0.7	85
Pt(0.500)/TNT-R	0.392	1.26 ± 0.34	273	9.6	0.6	87
Pt(1.000)/TNT-R	0.779	1.57 ± 0.35	261	9.3	0.6	70

[a]For d_p < 1.0 nm the D_{TEM} ~ 100%, dp: Pt particle size determined by HR-TEM analysis, D_p, porous diameter of the support determined by N_2 physisorption analysis

The HR-TEM micrographs reveal well-defined nanotube structures, with no noticeable changes in morphology or size after metal deposition (Figures 10A-10D). The uniform dispersion and narrow particle size distribution of Pt in Pt(0.125)/TNT-R catalysts indicate the formation of single site nanocrystals (Figure 10A). The majority of Pt species are smaller than 1.0 nm (Figure S1), which can be attributed to single site species, as confirmed by EDX analysis (Figure S2).

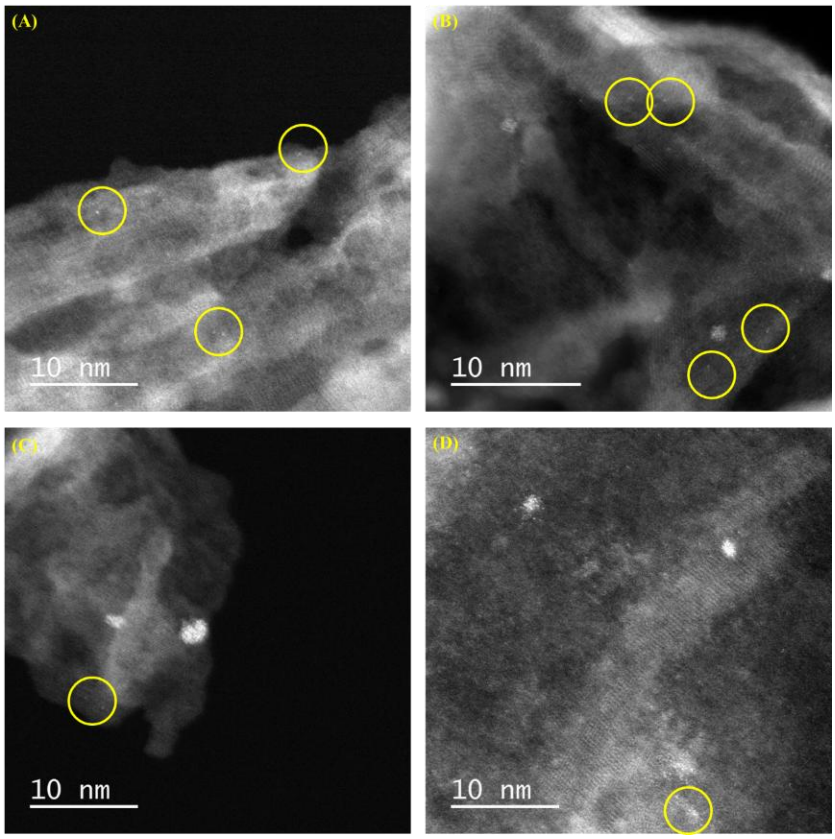

Figure 11. HR-TEM of the different Pt(%)/TNT-R catalyst. (A) Pt(0.125)/TNT-R. (B) Pt(0.250)/TNT-R. (C) Pt(0.500)/TNT-R. (D) Pt(1.000)/TNT-R. The platinum single sites are indicated in yellow circles.

In contrast, a different trend was observed in the Pt particle size for systems with higher metal loadings, from Pt(0.250)/TNT-R to Pt(1.000)/TNT-R as shown in Figure 11 B-D. This result makes us suppose that at low metal loadings, the deposition of Pt^{2+} species on the TNT-R surface was mediated by O_V, thus leading to a highly dispersed system of Pt species < 1.0 nm species.

The increase in Pt loading increased the incorporation of Pt^{2+} species, which besides the effect previously reported could enhance the nucleation around the nanocrystals in a

similar manner as was previously reported by Dinamarca *et al* [134]. However, the Pt particles size distribution displayed a narrow value for Pt(0.250)/TNT-R and Pt(0.5000)/TNT-R whereas the system Pt(1.000)/TNT-R displayed mainly Pt-NPs.

The N_2 physisorption isotherms at -196°C presented a similar trend as the TNT-R support (Table 1), which indicates the deposition of metal and catalysts precursor and H_2-assited reduction did not affect significantly the surface and shape of the TNT-R support. Similarly, the S_{BET} of TNT-R slightly decreased with the increase of metal loading, which is consistent with the decrease of the pore volume and may be associated with Pt deposition inside the pores.

X-ray diffraction was employed to confirm the crystallographic contribution of the TiO_x species as shown in Figure S3. Characteristic diffractions lines for TiO_2-anatase phase were not observed at 2θ = 25.4°, 37.9° and 48.2° [135], whereas broader peaks, with characteristics diffraction patters at 2θ = 25°, 29.9° and 48°, which are associated to the trititanate phase of the solid [136, 137].

In the case of the Pt-based catalysts, XRD patterns (Figure S3) reveal that the support structure remains unaltered after the deposition of Pt deposition. The increase in the size of metallic Pt displayed the absence of diffraction peaks attributed to a metallic Pt reported for the typical Miller indices of (1 1 1) and (2 0 0) (JCPDS No. 04-0802).

Raman spectroscopy was used to characterize the materials and catalysts to identify the present crystalline phases, as shown in Figure S4. The Raman spectrum displays multiple signals, most of which are attributed to the anatase phase present in all materials, with

characteristic peaks at approximately 15, 200, 380, and 520 cm^{-1} [138-141]. A minor but relevant contribution from the rutile phase is also detected, with peaks at 220 and 450 cm^{-1} [138, 139]. This is due to the synthesis of TNTs and the reduction of the support with $NaBH_4$, implying the formation of sodium compounds. Additionally, a minor contribution attributed to sodium perturbations was detected, with peaks at ~130 cm^{-1} for Na-O bonds [9] and at 280 cm^{-1} for Na-O-Ti [138]. A signal at ~160 and 840 cm^{-1} was assigned to the tubular structure of the support [139]. No signal was found in the area corresponding to amorphous or crystalline PtO [142, 143].

EPR spectroscopy is a sensitive and selective tool for probing paramagnetic compounds and materials, characterized by non-zero spin or orbital moment. TiO_2 materials contain point defects, mostly O_V and Ti^{3+}. Therefore, EPR analysis was employed to investigate the formation of the O_V and Ti^{3+} and to confirm the formation of Pt single site in the Pt(0.125)/TNT-R catalysts as displayed in Figure 12. The EPR spectra of anatase-TiO_2 and TNT-C support showed a characteristic weak signal at g: 1.998 G and g: 2.0042 G, which is associated with the presence of natural O_V [144]. For TNT-R, a significant increase in EPR resonance signal intensity is observed at g = 1.9797 G confirming the increase in the population of O_V and paramagnetic Ti^{3+} species as a consequence of the assisted-$NaBH_4$ reduction treatment [145-147]. For the Pt(0.125)/TNT-R catalyst, two less intense peaks are detected at g = 1.9816 G and 2.0026 G. This change is attributed to the presence of two Ti^{4+} species: (1) remnant Ti^{3+} species close to the O_V, and (2) Ti^{4+} species strongly interacting with Pt or O_V (Ti^{4+}-O_V-Ti^{4+}-OH^-) on the support [148].

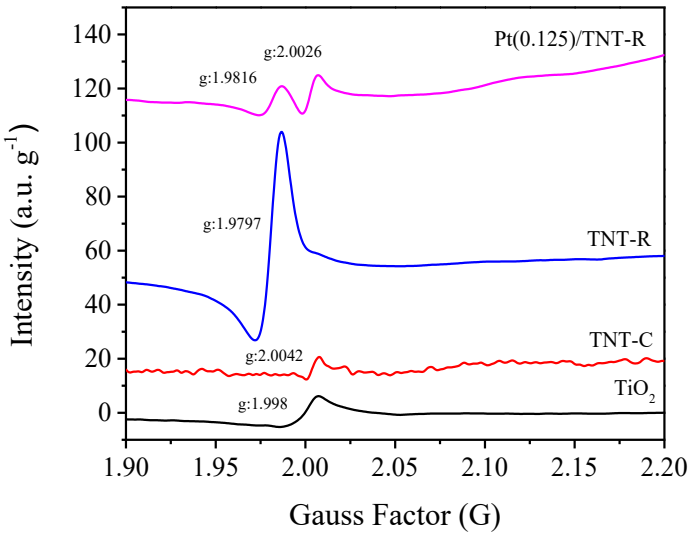

Figure 12. EPR spectra for the as-synthetized materials.

The EPR characterization demonstrates the formation of the desired O_V due to the assisted-$NaBH_4$ reduction process. To complement this characterization, adsorption of CO at –80°C coupled to Fourier Transform Infrared spectroscopy (FTIR-CO) was carried out as displayed in Figure 13. This technique detects the characteristic vibrational modes of CO when coordinated to single sites, providing insights into the electronic state of the metal and its local coordination environment. Figure 13 displayed the typical CO adsorption on the TNT-C support and the respective catalysts that have been studied. The presence of the characteristic Ti^{4+}-CO adsorption band at 2181cm^{-1} on the TNT-C support is detected, the signal is originated to the adsorption of carbonyl with the superficial Ti^{4+} species [149]. Nevertheless, for the Pt(0.125)/TNT-R catalyst, the Ti^{4+}-CO signal is shifted to lower wavenumbers at *ca.* 2165 cm^{-1}.

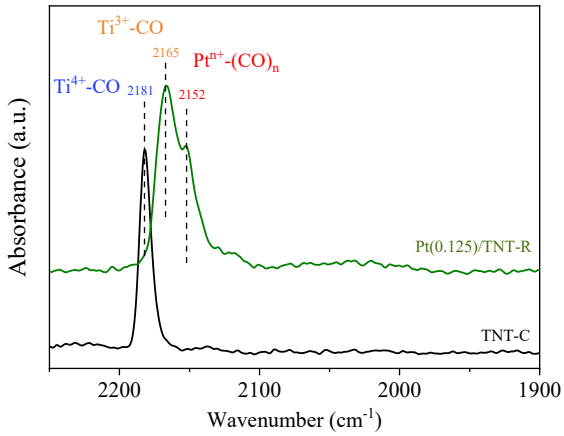

Figure 13. FTIR-CO at -80°C for the TNT-C and Pt(0.125)/TNT-R catalyst.

This shift is attributed to a change in the oxidation state of the titanium species from Ti^{4+} to Ti^{3+}, as the band at 2165 cm^{-1} is characteristic of Ti^{3+}-$(CO)_n$ [150]. This result aligns with the EPR that show the presence of Ti^{3+}. In the zone of electronic deficient $Pt^{\delta+}$ species a signal at 2152 cm^{-1} is indicative of the coordination of CO by highly oxidized $Pt^{\delta+}$ species, exhibiting different coordination types of $Pt^{\delta+}$-$(CO)_x$ [149, 151, 152]. This finding serves to reinforce the presence of single site species within the catalyst. This evidence is in line with the presence of single sites species as detected by HR-TEM and complemented by the EPR results. The CO adsorption evolution at different coverages for TNT-C and Pt(0.125)/TNT-R are displayed in the Figure S5.

All the characterization results demonstrated that the assisted-$NaBH_4$ reduction process of TNT-C promotes the formation of O_V and Ti^{3+} species enabling the formation of a

coordination environment capable of allowing the deposition of Pt species in isolated single site and NPs configurations.

4.5 Catalytic activity assays for NB hydrogenation and reductive amination

4.5.1 Nitrobenzene hydrogenation

4.5.1.1 Metal loading effect

The hydrogenation of NB was initially employed as a test reaction to evaluate the catalytic hydrogenation capability and to assess the effects of Pt SSCs and Pt NPs supported on TNT-R. Figure 14 displays the NB conversion over time for the different materials, with all catalysts achieving full NB conversion into aniline (100% selectivity). The data was fitted to a pseudo-first order kinetic model, and the results of the fitting are reported in Table 2. The k_{ap} and TOF values measured in all the catalysts follows the order Pt(0.125)/TNT-R > Pt(0.250)Pt/TNT-R > Pt(0.500)Pt/TNT-R > Pt(1.000)Pt/TNT-R, which indicate that the efficiency of the catalyst for NB hydrogenation is affected by the size distribution of the Pt, single site and NPs species on the catalysts surface [69-71, 153-155]. The Pt(0.125)/TNT-R displayed the major contribution on and singles sites Pt-based exhibiting enhanced catalytic activity for NB hydrogenation. The kinetic effect observed for this catalyst and confirmed by the highest k_{ap} and TOF values, is associated to a cooperative effect between single site with NPs [68, 69].

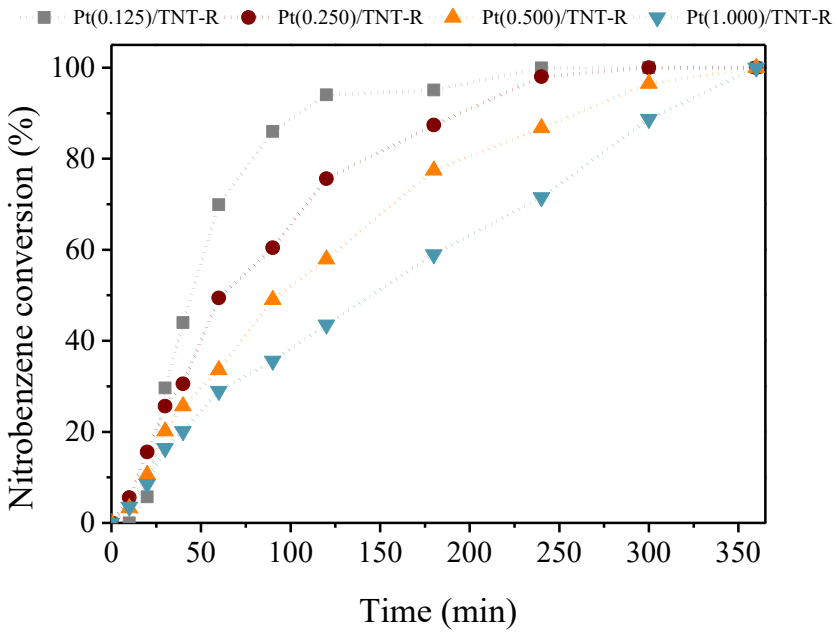

Figure 14. NB conversion for Pt(%)/TNT-R catalysts. Reaction conditions: 30°C, 30 mL EtOH, 10 bar H_2, 700 rpm and NB:Pt. 6000:1.

Table 2. Exploratory NB hydrogenation reactions employing Pt(%)/TNT-R catalyst.

Catalyst	k_{ap} (min^{-1})	TOF (min^{-1})	Yield %[a]	
			AN	Others
Pt(0.125)/TNT-R	0.0274	164	99.4	0.6
Pt(0.250)/TNT-R	0.0113	80	99.6	0.4
Pt(0.500)/TNT-R	0.0086	59	99.5	0.5
Pt(1.000)/TNT-R	0.0051	44	99.1	0.9

[a]Yield at 10% of conversion. The pseudo-first order adjustment is displayed in Figure S6.

Specifically, the observed cooperativity effect involves: (i) H_2 activation on NPs, (ii) hydrogen spillover onto the support, enabling the formation of H-single site species, and (iii) the catalytic reaction on these H-single site species, which are significantly more active than H-NP species. In this context, Pt(0.125)/TNT-R exhibits an induction period of approximately 10 minutes, attributed to the time required for H_2 activation on the Pt cluster to initiate the hydrogenation process[67].

Based on the previous results, the Pt(0.125)/TNT-R system was selected for a more detailed catalytic study. Figure 15 shows the Arrhenius plot of NB hydrogenation measured for this catalyst between 30 and 90°C, which shows a linear behavior (R^2 = 0.99) and led to a E_{aa} of 40.7 kJ mol^{-1}. The value of E_{aa} is in the same order as those previously reported for NB hydrogenation over catalytic systems based on noble and transition metals (Table 3).

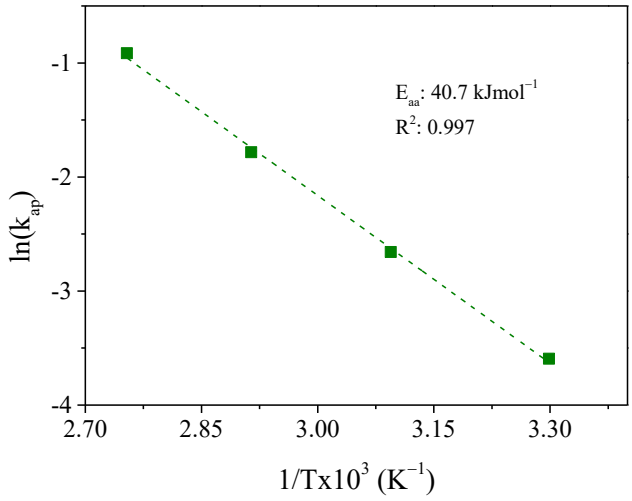

Figure 15. Arrhenius plot for the NB hydrogenation over Pt(0.125)/TNT-R catalyst. 30-90°C, 10 bar H_2, 700 rpm, 50 mg of catalyst, 30 mL EtOH, Pt:NB 1:6000.

In addition, the product distribution remained consistent at all evaluated temperatures, indicating that the formation of secondary products is temperature independent. These results highlight the potential of the Pt(0.125)/TNT-R catalyst for nitroarene reduction under moderate reaction conditions.

Table 3. Values of E_{aa} reported for NB hydrogenation over supported heterogeneous catalyst.

Catalyst	Solvent	T°C	H_2 pressure (bar)	E_{aa} $kjmol^{-1}$	Ref
Pd(3%)/C	MeOH	30-70	20	35.0	[156]
Ni(10%)/CarbonBlack	EtOH	100-160	15	42.6	[157]
Ni(10%)/Al_2O_3	EtOH	100-160	15	66.0	[157]
Ni-5/$SiO_{2\text{-}EN}$	EtOH	70-90	10	54.5	[158]
PtPdCoCuNi/SiO_2	Cyclohexane	25-80	30	28.9	[159]
PtPd/SiO_2	Cyclohexane	25-80	30	37.4	[159]
Ru(1.5)Pd(1.5)/C_3N_4	THF	50-80	30	26.3	[160]

4.5.1.2 Recyclability

The recyclability of the Pt(0.125)/TNT-R catalyst for NB hydrogenation was investigated. For comparison, recycling experiments were conducted using the control catalyst Pt(0.125)/TNT-C. All the characterization techniques of this catalyst are reported in the SUPPORTING INFORMATION. Also a blank test of the hydrogenation of NB only with

the support without metal impregnation was performed, no conversion to aniline was displayed by both materials (Figure S8).

To evaluate whether the support modification improved activity and recyclability, a control catalyst with the same Pt loading as Pt(0.125)/TNT-C was synthesized. For the fresh catalysts, the NB consumption over time was fitted to a pseudo-first-order kinetic model with k_{ap} of 0.0116 min^{-1} for Pt(0.125)/TNT-C and 0.0274 min^{-1} for Pt(0.125)/TNT-R. The TOF values were 44 min^{-1} for Pt(0.125)/TNT-C and 164 min^{-1} Pt(0.125)/TNT-R, indicating that the proposed Pt single site and NPs displayed an improved performance 3.7-fold higher than the control system. The NB conversion and AN selectivity as functions of the number of experimental runs are shown in Figure 16. In addition, the recycling stability (RS) was measured by**:**

$$RS\ (\%) = \frac{k_{ap,x}}{k_{ap,F}} \cdot 100 \tag{8}$$

where $k_{ap,x}$ corresponds to the pseudo-kinetic constant at every run and $k_{ap,F}$ is the pseudo-kinetic constant for the fresh catalyst. The recyclability tests for the Pt(0.125)/TNT-R catalyst demonstrated moderate stability, with performance remaining unchanged after 6 cycles; the catalyst maintained > 60 % NB conversion and > 97 % AN selectivity after 180 min. Furthermore, the RS decreased throughout the catalytic cycles reaching 31.5% in the final cycle. However, Pt(0.125)/TNT-C exhibited significantly lower stability after 180 min of reaction, achieving a maximum of 63% NB conversion and > 97% AN selectivity in the second cycle (Figure 16 (B)). Also, a substantial decrease in relative RS

was observed, reaching 3 % in the final cycle compared to the first cycle. These findings confirm continuous catalyst deactivation during the recyclability studies.

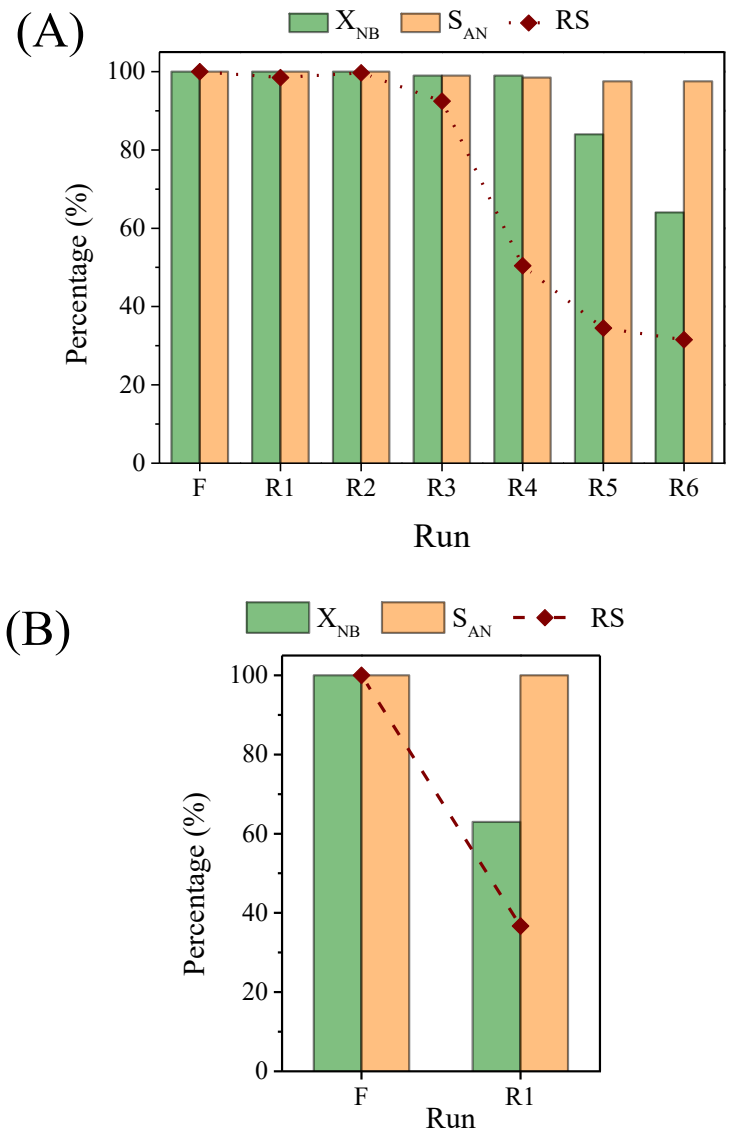

Figure 16. Recyclability of the Pt-based catalysts for the hydrogenation of NB at 180 min. (A) recycles for Pt(0.125)TNT-R and (B) Pt(0.125)/TNT-C. Reaction conditions: mass of catalysts 0.025 g, 10 bar H_2 pressure, 30°C, 30 mL of ethanol, and stirring speed of 700 rpm and Pt:NB 1:6000.

To analyse the possible cause of deactivation of the Pt(0.125)/TNT-R a series of post-reaction characterization were carried out for the recover catalyst. The metal leaching was confirmed by hot-filtration test after the third cycle (Figure S9). After catalyst separation, both the Pt(0.125)/TNT-R catalyst did not exhibit important change in the conversion level. The postreaction Pt content was determined by ICP-OES analysis of the catalyst recovered after the final cycle. The Pt content remains constant after the last catalytic cycle (Pt approx. 0.109 wt%), discarding the leaching of Pt from the catalyst into the liquid phase.

HR-TEM analysis of the spent catalysts (Figure 17) revealed an increase in the size of Pt-NPs (2.4 ± 0.6 nm) compared to the fresh catalyst (Figure 11). This result indicates that the Pt(0.125)/TNT-R catalyst was deactivated owing to the sintering of Pt single sites. A plausible explanation for particle sintering could be associated with the formation of H_2O as a coproduct of the hydrogenation process (NB hydrogenation generates 2 mol of H_2O per 1 mol of AN produced). Despite the mild temperature (30°C) and moderate H_2 pressure (10 bar), H_2O adsorption on the TNT-R surface may have promoted the metal sintering by Ostwald ripening effect by the hydration of the O_V enabling the coalescence of the Pt single sites to form Pt-NPs. In addition, we performed complementary experiments to evaluate the implications of H_2O in the NB hydrogenation over Pt(0.125)/TNT-R catalyst using a different H_2O dosage on the ethanolic liquid phase as displayed in Table 4.

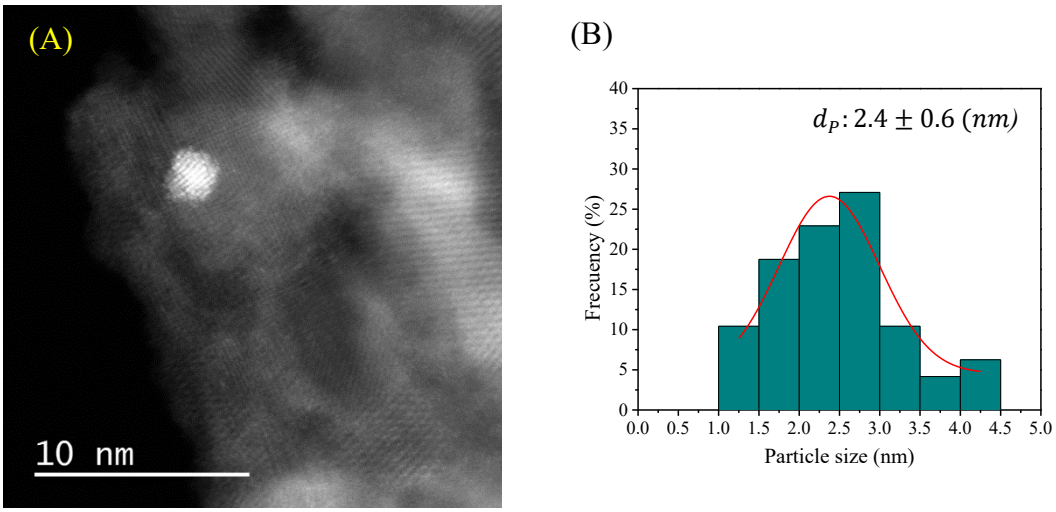

Figure 17. HR-TEM by atomic force microscopy of the used catalyst after the recycling experiment Pt(0.125)/TNT-R.

Table 4. Influence of water addition in the NB hydrogenation over Pt(0.125)/TNT-R catalyst.

Entry	Molar Ratio NB:H_2O	X_{NB} (%)	S_{AN} (%)	$S_{N\text{-}PHA}$ (%)	k_{ap} (min^{-1})	TOF_{AN} (min^{-1})
1	0	100.00	100.00	0.00	0.0274	164
2	2	96.05	99.82	0.18	0.0206	123
3	4	94.14	94.32	5.68	0.0095	54
4	6	76.18	98.24	1.76	0.0037	22
5	8	45.17	96.52	3.48	0.0016	9

Conversion to NB at 360 min of reaction also S_{AN}. 30°C, 10 bar H_2, Pt(0.125)/TNT-R 50 mg. pseudo-first order fit Figure S10.

The effect of varying the NB:H_2O molar ratios on the catalytic performance of NB) hydrogenation was evaluated. Increasing the NB:H_2O ratio beyond 2 led to a decrease in

NB conversion and a slight reduction in AN selectivity. This was accompanied by the accumulation of N-phenylhydroxylamine (N-PHA), identified as an intermediate, while no condensation by-products were detected in any of the experiments. These findings are consistent with previous reports by Corma *et al.* [161], who identified the hydrogenation of N-PHA to AN as the rate-determining step of the Haber reaction. Furthermore, tests involving the addition of water to the liquid phase confirmed its detrimental effect on catalyst stability, leading to deactivation and resulting in reduced reactivity and selectivity in the NB hydrogenation process.

4.5.1.3 Substituted nitroarenes hydrogenation

Owing to the catalytic activity of the Pt(0.125)/TNT-R catalyst, it was further evaluated for the hydrogenation of *para* substituted nitrobenzenes to obtain insights into the structural effects that govern the catalytic hydrogenation of the -NO_2 functional group. For this reaction, we aimed to evaluate the role of electron-donating and electron-withdrawing groups in the rate of hydrogenation by using the N-sources reported in the Table 5. The operational conditions for *p*-substituted nitrobenzenes hydrogenation were identical to those used for the reduction of NB. Kinetic data revealed that all compounds exhibited pseudo-first order constants for the catalytic hydrogenation reaction, leading to the formation of the corresponding *p*-substituted anilines as major products with yields higher than 95%, and negligible proportions of detected reaction intermediates except for the hydrogenation of *p*-dinitrobenzene where the accumulation of 1,2-bis(*p*-nitrophenyl)hydrazine was detected.

Table 5. Kinetic parameters of *p*-substituted nitrobenzenes hydrogenation over Pt(0.125)/TNT-R catalyst. Hammet sigma constant (σ^{+}_{p}) and the solvation free energy of the substrate (ΔG_{sov}) as predictor variables were used from reported data [123].

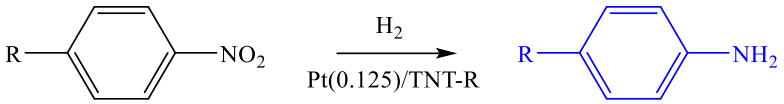

Substituent	$TOF_{p\text{-aniline}}$ (min^{-1})	$S_{p\text{-aniline}}$ (%)	k_{ap} (min^{-1})	σ^{+}_{p}	ΔG_{solv} (kcal/mol)	CB (%)
NO_2	121	85.3*	0.0466	0.79	-5.74	>99
CN	216	99.8	0.0361	0.66	-6.35	>99
CHO	183	99.5	0.0306	0.73	-5.61	>99
Cl	184	99.1	0.0310	0.11	-3.96	>99
H	163	99.4	0.0274	0.00	-4.04	>99
CH_3	138	99.5	0.0231	-0.31	-4.25	>99
OCH_3	95	98.8	0.0160	-0.78	-4.48	>99
NH_2	81	98.4	0.0137	-1.30	-7.74	>99
OH	53	97.5	0.0091	-0.92	-6.75	>99

*The condensation product 1,2-bis(4-nitrophenyl)hydrazine is detected. $S_{p\text{-aniline}}$ at isoconversion = 20%. Reaction conditions: mass of catalysts 0.050 g, 10 bar H_2 pressure, 30°C, 30 mL of ethanol, and stirring speed of 700 rpm and Pt:substrate 1:6000.

Under the reactions conditions (T= 30°C and P = 10 bar of H_2), the electron-withdrawing effect of -NO_2 on the *para* position increase the reactivity of the *p*-nitroso-nitrobenzene intermediary enhancing the condensation with the N-(*p*-nitrophenyl)hydroxylamine intermediary to produce the undesired product [162, 163]. Nevertheless, significant variations were observed in the conversion of the reactant to the desired product, and in the rate of hydrogenation as the electronic nature of the substituent group was modified, which evidenced a strong influence of electronic effects on this reaction (Table 5). Kinetic data revealed that electron-withdrawing groups activated the hydrogenation reaction, whereas electron-donating groups drastically reduced the rate of reaction compared to nitrobenzene. Within electron-withdrawing substituents, -NO_2 group exerted the largest increase in the rate constant compared to -CN, -CHO and -Cl moieties, which exhibited similar activating profiles. In the case of electron-donating groups, all species displayed reduced rate constants compared to NB, following the sequence single -CH_3 > -OCH_3 > -NH_2 > -OH. The largest deactivating effect was displayed by the -OH substituent, with the lowest kinetic constant and a minimum TOF to *p*-aminophenol (Table 5). Strong electron-donating groups such as single -OCH_3 and -NH_2 induced also a decreased conversion to the corresponding *p*-substituted anilines, with TOF ~ 100 min^{-1}. The weak electron-donating single -CH_3 group exhibited a less pronounced effect in conversion showing a similar TOF than NB.

The strong dependence of the hydrogenation rate on the nature of the substituents in the series of *para*-substituted nitrobenzenes under study can be rationalized by the proposed Haber reaction mechanism. In this mechanism, the rate-limiting step involves the

hydrogenation of N-phenylhydroxylamine (N-PHA) to the corresponding AN, accompanied by the loss of a water molecule. During the transition state of this step, an increase in electron density on the nitrogen atom is expected [123], which can be stabilized by electron-withdrawing groups on the aromatic ring. Conversely, electron-donating groups destabilize the transition state, thereby reducing the reaction rate. These effects explain the observed sensitivity of the hydrogenation reaction to substituent electronic properties. It is worth noting that when the catalyst support exhibits Lewis acidity, such as in the case of partially reduced Ti-based oxides, electron donation from the support can facilitate the hydrogenation process. This occurs through coordination to the intermediate reaction, effectively stabilizing the transition state and enhancing the overall hydrogenation rate, even in the presence of electron-donating substituents on the aromatic ring.

To provide a quantitative description of the structural dependence of hydrogenation rates, a multilinear regression model was constructed using two molecular descriptors: the Hammett σ^{+}_{p} constant of the substituent and the solvation free energy (ΔG_{solv}) of the substrate. The σ^{+}_{p} constants were used as established indicators of the electronic properties of para-substituents, while ΔG_{solv} values described the affinity of each substrate for the solvent (ethanol). This parameter is relevant because highly solvated species are less available to adsorb onto the catalyst surface, which can reduce their reactivity. ΔG_{solv} values in ethanol were obtained from previously reported DFT calculations [123]. The multilinear regression was calculated in Origin® software indicating the $\log k_{ap}$ calculated

from the experimental data as dependent variable and the σ_p^+ and ΔG_{solv} as independent variables, the resulting model shows that the experimental pseudo-first-order rate constants (k_{ap}) for hydrogenation of para-substituted nitrobenzenes are well described by the following regression equation:

$$\log k_{ap(model)} = 0.2571\sigma_p^+ + 0.030\Delta G_{solv} - 1.444 \qquad r^2: 0.968 \tag{9}$$

A high correlation was observed between the experimental and predicted values (r^2 = 0.970), as shown in Figure 18. Variance analysis indicates that σ^+_p is the most significant variable, highlighting the dominant role of electronic effects in controlling the hydrogenation rate. This supports a mechanism in which negative charge builds up on the nitrogen atom during the rate-limiting hydrogenation of N-phenylhydroxylamine (N-PHA) to AN, accompanied by water elimination.

The positive regression coefficient associated with σ^+_p can be interpreted as a Hammett ρ parameter in the range $0 < \rho < 1$, which is consistent with a moderately structure-sensitive reaction. The contribution of ΔG_{solv}, while less significant, indicates that stronger solvation decreases the reaction rate, as expected. This suggests that hydrogenation of nitrobenzenes may proceed more efficiently in less polar solvents, a relevant insight given that such reactions are typically performed in alcohols like ethanol.

Overall, this theoretical analysis provides a framework for understanding how both electronic and solvation effects influence catalytic performance in the Pt(0.125)/TNT-R system and offers guidance for the rational design of improved reaction conditions.

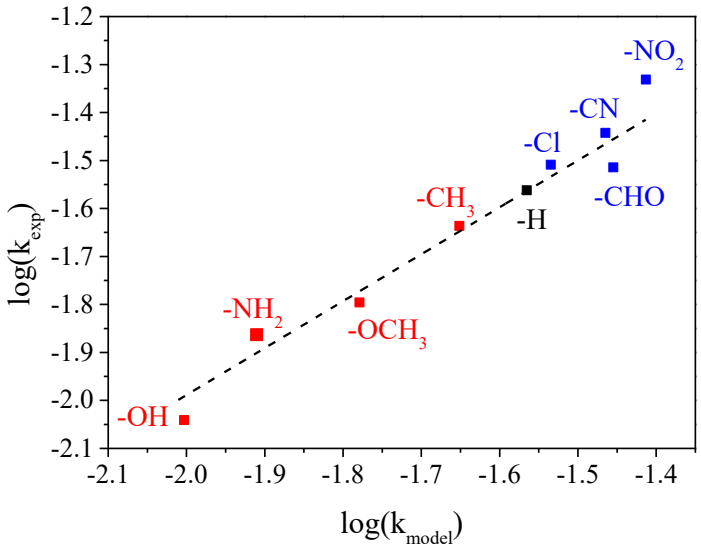

Figure 18. Correlation between log $k_{ap,\ exp}$ and log $k_{ap,\ model}$ for *p*-substituted nitroarenes hydrogenation on Pt(0.125)/TNT-R catalyst. Conditions: a batch reactor, T = 30 °C, 10 bar of H_2 pressure, 30 mL EtOH, Pt:substrate 1:6000

4.5.2 One-pot synthesis of N-furfurylaniline by reductive amination of nitrobenzene and furfural.

4.5.2.1 Metal loading effect

The synthesis of N-furfurylaniline (FFA) has traditionally been achieved through the hydrogenation of furfural-derived intermediates such as furfural phenylhydrazone, furfural oxime, or furfuryl azide. Although effective, these approaches generally require

harsh operating conditions and involve a high energy demand, particularly during product separation and purification steps [128]. In response to these limitations, the heterogeneously catalysed one-pot reductive amination of FUR has emerged as an attractive alternative to produce aromatic amines.

In this process, the one-pot reductive amination of FUR proceeds through a sequence of interconnected steps, as illustrated in Figure 5. Nitrobenzene is initially hydrogenated to AN, which subsequently acts as the nitrogen source for the condensation with the carbonyl group of FUR, leading to the formation of the imine intermediate furfuryl-N-phenylmethanimine (ANI). The hydrogenation of the C=N bond in ANI then yields the desired product, N-furfurylaniline (FFA). However, competing reactions may occur during this transformation, including the formation of furfuryl alcohol (FOL) from FUR or the over-hydrogenation of ANI and FFA, which can negatively affect product selectivity.

In this study, Pt(x)/TNT-R catalysts are proposed as efficient systems for promoting the one-pot reductive amination of FUR and NB toward FFA. Control experiments conducted using TNT-C and TNT-R supports in the absence of Pt confirmed that NB hydrogenation does not occur without the metallic phase (Figure S8), demonstrating the essential role of Pt in activating hydrogen. The catalytic performance of Pt(x)/TNT-R was further evaluated using ethanol and ethyl acetate as solvents, as summarized in Table 6, with the aim of identifying conditions that favour the formation of the desired products.

Table 6. Kinect parameter for the Pt(%)/TNT-R catalysts in the different solvents.

Catalyst	Ethanol					Ethyl Acetate				
	$k_{ap,NB}$ (min^{-1})	$k_{ap,ANI}$ (min^{-1})	S_{FFA}[a] (%)	TOF_{FFA}[b] (min^{-1})	CB_{FUR} (%)	$k_{ap,NB}$ (min^{-1})	$k_{ap,ANI}$ (min^{-1})	S_{FFA}[a] (%)	TOF_{FFA}[c] (min^{-1})	CB_{FUR} (%)
Pt(0.125)/TNT-R	0.0036	0.0022	23	3.0	> 98	0.0031	0.0025	11	0.9	> 98
Pt(0.250)/TNT-R	0.0025	0.0018	9	2.5	> 98	0.0026	0.0023	12	2.1	> 98
Pt(0.500)/TNT-R	0.0014	---	15	---	> 98	0.0013	---	3	---	> 98
Pt(1.000)/TNT-R	0.0018	---	24	---	> 98	0.0012	---	13	---	> 98

Reaction conditions: 30°C, 10 bar H_2, NB:FUR:Pt 6000:6000:1. [a]at isoconversion X_{NB} = 20%.[b]at the concentration of FFA for $\frac{dC_{ANI}}{dt} = 0$

Solvent effects were carefully considered, as ethanol can participate in nucleophilic addition to the carbonyl group of FUR, potentially leading to the formation of hemiacetals or acetals [99]. Despite this possibility, the consumption of NB over time followed a pseudo-first-order kinetic behaviour in both solvents, showing comparable trends (Figure S11). Regardless of the solvent employed, the reaction predominantly produced AN, ANI, and FFA, while the formation of furfuryl alcohol was detected only in negligible amounts. Based on the observed product distributions (Figure S12 and Figure S13), a general reaction scheme is proposed in Figure 19.

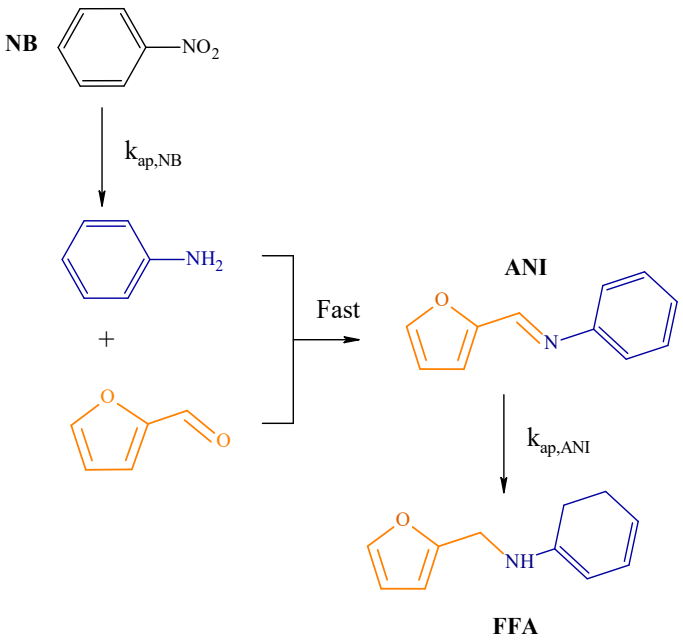

Figure 19. Simplified proposed reaction scheme for the one-pot reductive amination of NB and FUR to produce FFA.

In agreement with previous reports by Andrade *et al* [128] on the direct reductive amination of AN and FUR under non-catalytic conditions, a reaction pathway is proposed

in which NB is first hydrogenated to AN, followed by rapid condensation with FUR to form the ANI intermediate through an apparently non-catalytic step [164]. The subsequent hydrogenation of ANI to FFA is then promoted by hydrogen activated on Pt NPs. This simplified mechanistic description also provides the basis for a kinetic model involving two consecutive pseudo-first-order steps, corresponding to the hydrogenation of NB and ANI, respectively [165]. This model was applied here to estimate $k_{ap,NB}$ and $k_{ap,ANI}$ taking into account the initial rates ($\frac{dC_{ANI}}{dt} = 0$), and re-arranging the equations the parameters characterizing the reaction kinetics can be estimated from the following equations[165]:

$$t_{ANI,max} = \frac{\ln\left(k_{ap,NB}/k_{ap,ANI}\right)}{k_{ap,NB} - k_{ap,ANI}} \tag{10}$$

$$C_{AN,max} = C_{NB,0}\left(\frac{k_{ap,NB}}{k_{ap,ANI}}\right)^{\left(k_{ap,ANI}/k_{ap,ANI}-k_{ap,NB}\right)} \tag{11}$$

Here, $k_{ap,NB}$ represents the pseudo-first-order kinetic constant for NB hydrogenation, while $k_{ap,ANI}$ corresponds to the subsequent pseudo-first-order kinetic constant for ANI hydrogenation. $C_{ANI,max}$ denotes the maximum concentration of ANI, $t_{AN,max}$ is the time required to reach $C_{AN,max}$ and $C_{NB,0}$ refers to the initial NB concentration.

Based on the product distribution profiles (Figure S12 & Figure S13), the proposed kinetic model could only be reliably applied to the Pt(0.125)/TNT-R and Pt(0.250)/TNT-R catalysts, which allowed the estimation of the corresponding kinetic parameters. The pseudo-first-order constants for the hydrogenation of ANI to form FFA were found to be lower than those for NB hydrogenation, indicating that the reduction of the nitro group (-NO_2 to -NH_2) is kinetically favoured over the reduction of the imine group (C=N).

The turnover frequency (TOF) for FFA formation followed the order Pt(0.125)/TNT-R > Pt(0.250)/TNT-R in both solvents, as shown in Table 6. These results suggest that catalyst efficiency for the one-pot reductive amination to FFA is influenced by the Pt particle size distribution, similarly to what is observed in the NB hydrogenation. Additionally, the solvent plays a significant role: the use of ethanol led to higher selectivity toward FFA compared to ethyl acetate.

4.5.2.2 Complementary characterization

The chemical nature of the metal-support interface plays a critical role in catalysis, as it influences not only the hydrogenation capacity of the active sites but also the acid-base properties of the material, which can, in turn, promote undesired side reactions. To better understand these effects, FT-IR spectroscopy of adsorbed pyridine (FT-IR-Py) was performed to characterize the surface acidity of Pt(0.125)/TNT-R and the control catalyst Pt(0.125)/TNT-C, as shown in Figure 20. Both catalysts exhibited characteristic bands associated with Lewis acid sites (LPy) at 1445, 1489, 1574, and 1606 cm^{-1}. In addition, bands at 1440 and 1591 cm^{-1} were assigned to protonated pyridine (HPy), indicative of

weaker acidic sites [163–165]. A small band at 1542 cm^{-1}, corresponding to Brønsted acid sites, was observed only for the control catalyst (Pt(0.125)/TNT-C), suggesting that these sites are either absent or negligible in the reduced support.

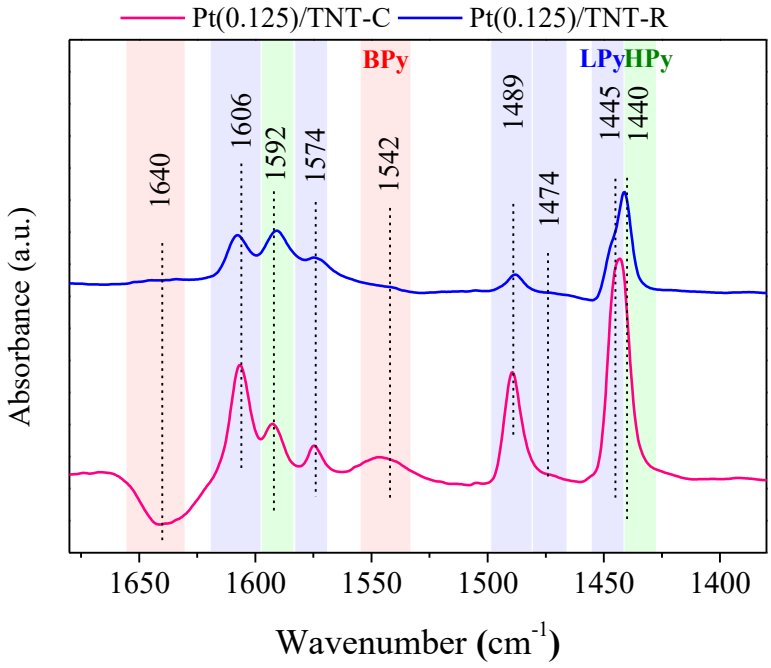

Figure 20. FT-IR of absorbed Py for the Pt(0.125)/TNT-C and Pt(0.125)/TNT-R, recording following a brief outgassing of at 150°C.

To estimate the relative abundance of Lewis (LPy) and protonated weak acid sites (HPy), the ratio of the absorbance at 1606 cm^{-1} (LPy) and 1591 cm^{-1} (HPy) was calculated. For accurate comparison, identical sample quantities were used for both measurements. As shown in Figure 21, the Pt(0.125)/TNT-R catalyst exhibited an LPy:HPy ratio of 0.88, indicating a slightly higher proportion of HPy-type (weaker) acid sites. In contrast,

Pt(0.125)/TNT-C displayed a ratio of 5.85, clearly demonstrating that Lewis's acid sites dominate in this material.

This trend is further supported by the deconvolution of the region around 1440 cm^{-1} (Figure 21(B)), which highlights the relative contribution of each type of acidic site. For Pt(0.125)/TNT-R, the areas corresponding to LPy and HPy are comparable, whereas in Pt(0.125)/TNT-C, the LPy signal is significantly more intense, confirming the predominance of Lewis acidity in the control sample.

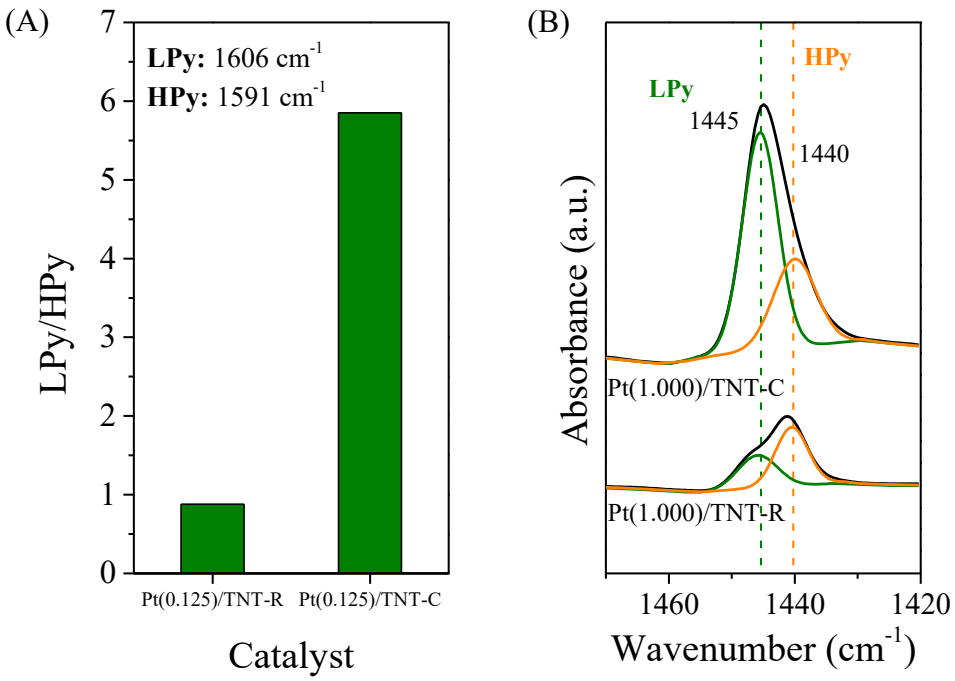

Figure 21. (A) ratio between the LPy acid sites and HPy acid sites in the catalyst, (b) deconvolution of the mix signal of LPy and HPy. (B) IR band position and the relativity intensities (LPy/HPy).

To complement the FTIR-Py results, ammonia TPD (TPD-NH_3) was performed (Figure S14). The desorption temperature of ammonia depends on the strength at which it adsorbs on the acid site, so the surface acidity can be classified as weak (100-300°C), medium (300-500°C), and strong (above 500°C) [45]. Considering that both catalysts displayed the main desorption peak below 300°C, their acidity is predominantly weak [166, 167]. The total acidity estimated for Pt(0.125)/TNT-R was 5.53 $mmol_{NH_3}$ g^{-1} with an acid density of 13.9 μmol_{NH_3} m^{-2} given mainly by protonated weak acid sites and a small contributions of Lewis sites whereas Pt(0.125)/TNT-C catalyst displayed 4.03 $mmol_{NH_3}$ g^{-1} with an acid density of 10.1 μmol_{NH_3} m^{-2} given mainly by Lewis's acid sites.

4.5.2.3 Proposed reaction scheme

To propose a preliminary reaction scheme consistent with the reductive amination of FUR, a temperature-dependent kinetic study was carried out to compare the apparent activation energies associated with NB hydrogenation and the one-pot reductive amination of NB with FUR. Reactions were evaluated over the temperature range of 30-90°C, as shown in Figure 22. NB conversion data were satisfactorily described by a pseudo-first-order kinetic model (Figure S15). As expected, increasing the reaction temperature led to higher conversions and apparent rate constants (k_{ap}) for both NB and FUR, reaching complete NB conversion and approximately 98 % FUR conversion at the highest temperature. Importantly, no over-hydrogenated products derived from FUR, its intermediates, or the aromatic ring were detected within the explored temperature range.

As shown in Figure 22(A), the Pt(0.125)/TNT-R catalyst exhibited an apparent activation energy of 40.7 kJ mol^{-1} for NB hydrogenation, while a slightly higher value of 43.2 kJ mol^{-1} was obtained for the one-pot reductive amination reaction. The close similarity between these values indicates that the presence of FUR does not significantly hinder $–NO_2$ hydrogenation under the investigated conditions, although it does not necessarily imply that both processes share an identical rate-determining step.

To further explore the reaction sequence, a consecutive reaction model was evaluated using product distribution data collected at different temperatures (Figure S16). From this analysis, the apparent rate constant for imine hydrogenation ($k_{ap,ANI}$) was determined and fitted to the Arrhenius equation, yielding a higher apparent activation energy of 50.2 kJ mol^{-1}. This trend suggests that, within the one-pot reductive amination process, hydrogenation of the C=N bond is kinetically more demanding than the initial $–NO_2$ reduction step. However, the observed deviation from linearity in the Arrhenius plot indicates that the kinetics of this step are likely influenced by changes in surface coverage, competitive adsorption of intermediates, and metal-support interactions, rather than being governed by a single elementary step.

Product distributions were strongly affected by temperature, as illustrated in Figure 22(B), Aniline, the imine intermediate (ANI), and furfuryl aniline (FFA) were identified as the main reaction products. Furfuryl alcohol was detected only at temperatures above 70°C and at high NB conversion, pointing to secondary hydrogenation of FUR.

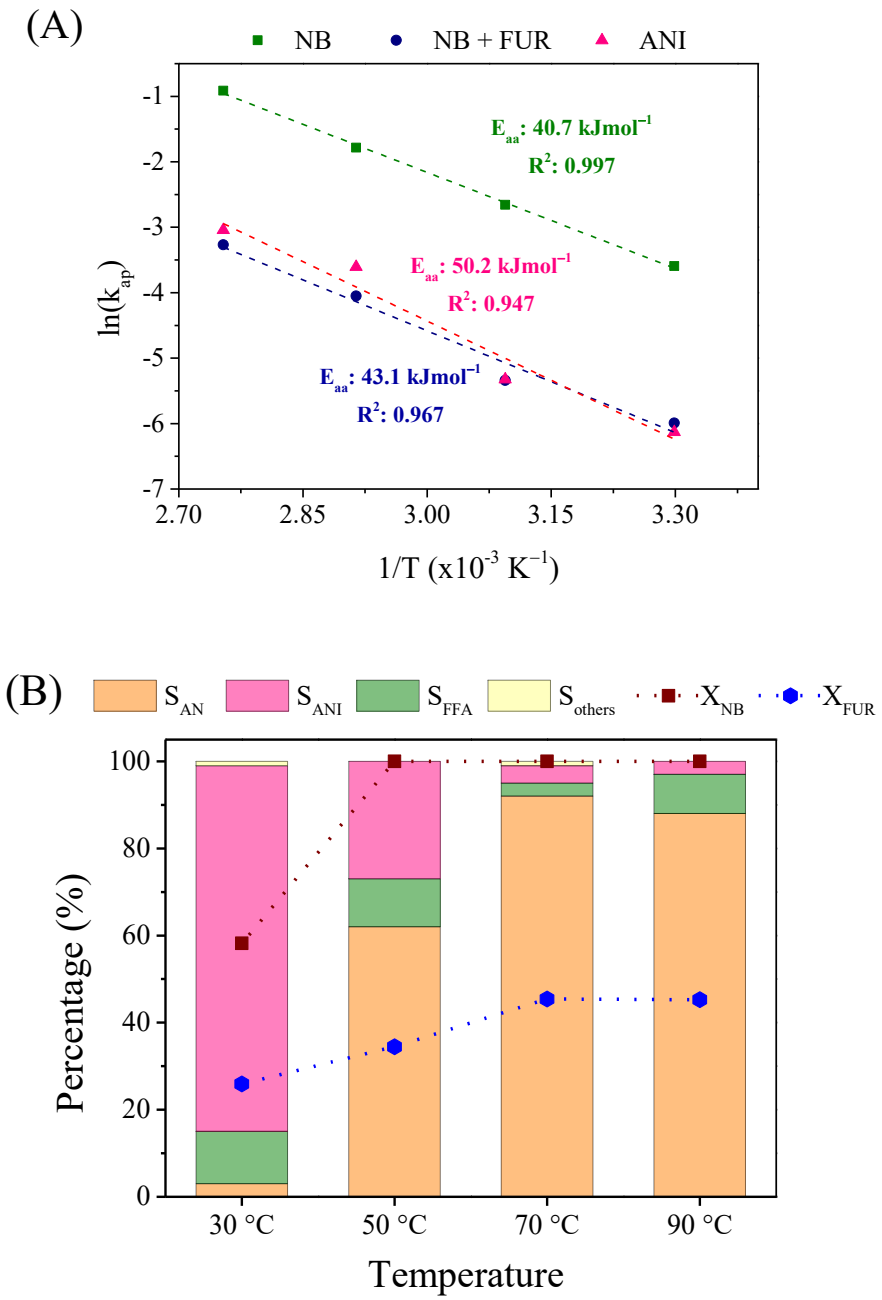

Figure 22. Temperature effect over the reaction NB and FUR. (A) Arrhenius plot for the hydrogenation of just NB, NB and FUR, and hydrogenation of the ANI (B) Product distribution at at NB isoconversion = 50% , X_{NB} and X_{FUR} at 360 min employing different temperatures. 10 bar H_2, Pt(0.125)/TNT-R 50 mg, Pt:NB:FUR 1:6000:6000.

Carbon balance values remained close to 98 % over the entire temperature range, confirming the absence of significant polymer formation or undetected by-products, even at 90°C.

Interestingly, at a fixed isoconversion level of 50 %, increasing the temperature led to a decrease in FFA selectivity, suggesting a delicate balance between imine formation, stabilization, hydrogenation, and desorption processes. To further investigate the contribution of non-catalytic pathways to this behaviour, the direct reductive amination of AN with FUR was examined under homogeneous, non-catalytic conditions, following the methodology reported by Fernández-Andrade *et al.* [125]. These authors [125] demonstrated that FUR and AN undergo condensation without the need of a catalyst, which was in line with the enthalpy (ΔH) and entropy (ΔS) values calculated from experimental and theoretical data. According to the evidence, we propose that the AN accumulation observed here could be attributed to the displacement of the chemical equilibrium to the formation of ANI. Then, in the second stage, the ANI is hydrogenated to FFA with the H activated over Pt-NPs sites as previously reported for similar reactions [168].

In addition, the Pt(0.125)/TNT-C catalyst exhibited a lower selectivity to FFA, lower TOF and 10% less conversion of NB than Pt(0.125)/TNT-R. Moreover, the product distribution of this catalyst did not include the formation of FFA, Table 7. The lower production of FFA over Pt(0.125)/TNT-C catalyst could be explained by a strong interaction of FUR with the Lewis acid sites on the support. These acid sites enable the strong adsorption of

C=O with the surface decreasing the ability to form ANI as well as did not perturb the hydrogenation assisted by Pt-NPs to produce AN, also another hypothesis is the covering of the catalyst surface by the generated aniline by acid-base Lewis interaction, affecting the sites balance and limiting the FFA generation. Although these results demonstrate that it is non-feasible to hydrogenate the C=O of FUR under the conditions studied, the absence of furfuryl alcohol in the one-pot reductive amination products suggests a selective hydrogenation of C=N bonds rather than C=O adsorbed on the supports. Thus, our results provide the basis to confirm the benefits of the use of this kind of support in the one-pot reductive amination of FUR with nitroarenes.

Table 7. Kinect parameter for the Pt(0.125)/TNT-R and Pt(0.125)/TNT-C catalysts in the one-pot reductive amination of NB and FUR to produce FFA.

Exp	Catalyst	$k_{ap,NB}$ (min^{-1})	$k_{ap,ANI}$ (min^{-1})	X_{NB} (%)	X_{FUR} (%)	S_{FFA}[a] (%)	TOF_{FFA} (min^{-1})	CB (%)
1	Pt(0.125)/TNT-C	0.0020	0.0021	56	55	15	2.2	>98
2	Pt(0.125)/TNT-R	0.0036	0.0022	68	65	23	3.0	>98

Reaction conditions: 30°C, 10 bar H_2, NB:FUR:Pt 6000:6000:1, 30 mL of ethanol as solvent. [a]30% of conversion [b]360 min. Reaction conditions: 30°C, 10 bar H_2, NB:FUR:Pt 6000:6000:1. [a]at isoconversion X_{NB} = 20%.[b]at the concentration of FFA for $\frac{dC_{ANI}}{dt} = 0$

4.5.2.4 Recyclability

The recyclability of the Pt(0.125)/TNT-R catalyst during the one-pot reductive amination of FUR and NB was investigated. The NB conversion, FUR conversion and FFA selectivity as functions of the number of experimental runs are shown in Figure 23. The

recyclability tests for the Pt(0.125)/TNT-R catalyst demonstrated deactivation after the first run. However, after the second run, the NB conversion, selectivity to FFA and the RS (equation 8, section 0) reached a plateau. On the same way, the carbon balance remained between 94-98% during all the catalytic cycles, suggesting a negligible carbon loss. The slight loss of carbon observed is attributed to the formation of byproducts such as FUR-based polymers. Other undesired products such as furfuryl alcohol or over-hydrogenated amines from FFA were not detected.

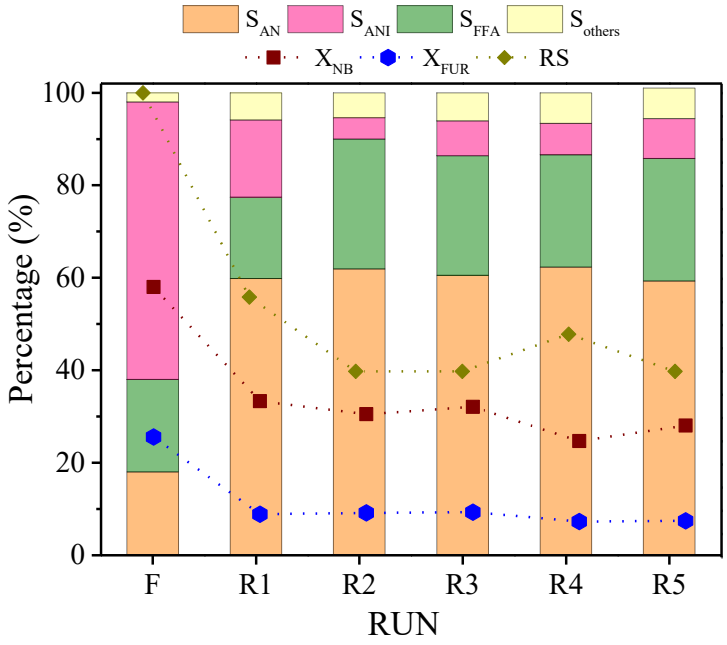

Figure 23 Recycling experiment for one-pot reductive amination of NB and FUR. The selectivity at isoconversion of 20 %, and conversion of NB and FUR at 180 min of reaction time. Pt(0.125)/TNT-R, 50 mg, 30°C, 10 bar H_2, NB:FUR:Pt 6000:6000:1.

To evaluate possible post-reaction deactivation pathways, the Pt content of the catalysts recovered after the final cycle was determined by ICP-OES. The Pt loading remained

essentially constant (0.098 wt%), confirming negligible leaching of Pt into the liquid phase. TEM analysis of the spent catalysts revealed a moderate increase in the Pt particle size distribution (3.5 ± 0.8 nm), with NPs being the dominant species (Figure 24). These observations indicate that deactivation of the Pt(0.125)/TNT-R catalyst is mainly associated with sintering of the metallic active phase. A plausible explanation for this behaviour was discussed in the previous section, where H_2O was proposed to promote the collapse of Pt single sites into NPs. Notably, water formation during the one-pot reductive amination of NB and FUR is substantially higher than during NB hydrogenation alone, since in this reaction 1 mol of NB and 1 mol of FUR leads to the generation of 3 mol of H_2O in the reaction medium. This enhanced water production likely accelerates Pt sintering, thereby decreasing the catalyst recycling efficiency.

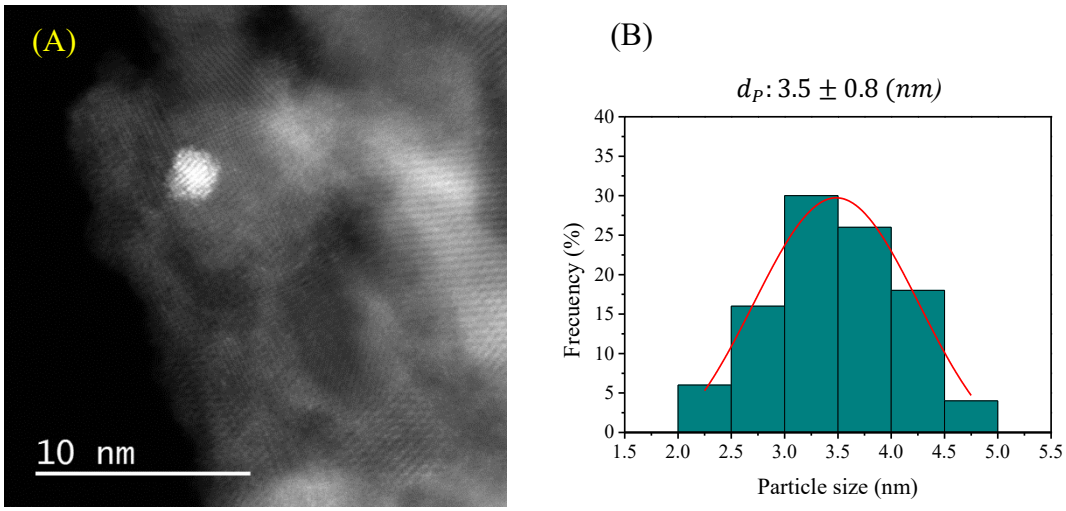

Figure 24. (A) High resolution microscopy post recycling test of Pt(0.125)/TNT-R for one-pot reductive amination of NB + FUR to produce FFA and (B) Particles distribution histogram for the HR-TEM characterization.

4.5.2.5 Evaluation of substituted nitroarenes in the one-pot reductive animation to produce N-furfurylanilines

To evaluate the versatility of the catalyst, a series of *para* substituted nitroarenes (*p*-NB) were evaluated under the same experimental conditions of the reaction of NB and FUR to obtain FFA (30°C, 10 bar H_2, Pt(0.125)/TNT-R 50 mg, Pt:*p*-NB:FUR 1:6000:6000, 700 rpm). The conversion of the nitroarene and the selectivity to the desired *p*-N-furfurylaniline product obtained during this substrate survey are displayed in Table 8. The conversion of NB and FUR is reported at 360 min, also the selectivity was determined at 10% of conversion for every substrate, and the $k_{ap,p\text{-NB}}$ was calculated according to the pseudo-first-order kinetic model for the *p*-NB hydrogenation. The conversion of *p*-NB displayed the same trend as that discussed in section 4.5.1.3. The electron-withdrawing groups increased the value of $k_{ap,p\text{-NB}}$ while the electron-donating groups decreased catalytic activity, which is attributed to the electronic effects during the hydrogenation of the $-NO_2$ group over the metal surface. The selectivity in the one-pot reductive amination of *p*-NB molecules with electron-withdrawing groups displayed slight production of *para* substituted N-furfurylaniline (*p*-FFA) and an important accumulation of the corresponding *para* substituted anilines (*p*-AN). However, the $-CH_3$ group shows a similar selectivity for the formation of *p*-AN and *p*-ANI whereas the $-OCH_3$, $-NH_2$ and -OH reached $S_{p\text{-ANI}} >$ 80% at isoconversion and negligible formation *p*-FFA. This behaviour suggests that the electronic nature of the substituent modify the reactivity of the *p*-AN to condensate and produce the corresponding *p*-FFA.

Table 8. Kinetic parameters for the one-pot reductive amination of *p*-substituted nitrobenzenes and FUR to produce *p*-FFA over Pt(0.125)/TNT-R catalyst.

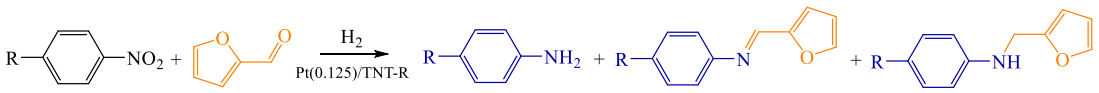

Substrate	X_{NB} (%)	X_{FUR} (%)	$S_{p\text{-AN}}$ (%)	$S_{p\text{-ANI}}$ (%)	$S_{p\text{-FFA}}$ (%)	$k_{ap,p\text{-NB}}$ (min^{-1})	CB (%)
NO_2	100	5	99[a]	<1	1	0.0522	>98
CN	100	12	99	<1	1	0.0249	>98
CHO	100	18	87	3	10	0.0163	>98
Cl	90	27	74	6	20	0.0071	>98
H	68	66	15	64	20	0.0036	>98
CH_3	64	59	49	41	10	0.0031	>98
OCH_3	28	27	<1	87	13	0.0011	>98
NH_2	13	12	<1	84	16	0.0004	>98
OH	10	8	<1	99	<1	0.0002	>98

According to the previous evidence, we propose the following reaction pathway: in the first stage, *p*-NB is hydrogenated to *p*-AN and then FUR reacts with *p*-AN by nucleophilic attack to form the *p*-ANI intermediate; the electron-withdrawing groups decrease the nucleophilic ability of the -NH_2 group to form the corresponding p-ANI product and the electron-donating groups act in an opposite way. Then, in the second stage, the *p*-ANI is hydrogenated to FFA with the H activated over Pt-NPs sites where electron-withdrawing groups increase the hydrogenation step while the electron-donating groups decreased the hydrogenation ability. A correlation between the kinetic constant (k_{ap}) and Hammet´s parameter (σ^{+}_{p}) was made (Figure 25). This correlation displayed a linear trend with R^2: 0.96, which is similar to that previously obtained for the NB hydrogenation (See section 4.5.1.3). These results indicate that the major inhibition effect on the NB hydrogenation for the reaction of NB and FUR is caused by the -OH group, while the reaction is favoured by the -NO_2 group, clearly the electronic effect of the nature of the p-group is observed as was observed for pure NB hydrogenation, the presence of FUR does not cause a considerable perturbation in the electronic behaviour of the *p*-nitrobenzene.

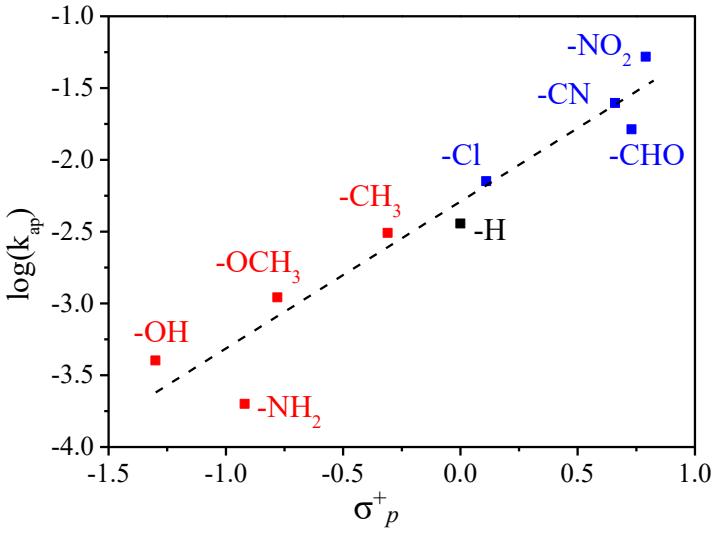

Figure 25. Hammet plot for the study of different p-nitroarenes in the one-pot reaction between NB and FUR, correlation of $\log(k_{ap})$ versus the σ^{+}_{p}. Conditions: a batch reactor, T = 30 °C, 10 bar of H_2 pressure, 30 mL EtOH, Pt:substrate 1:6000, 700 rpm.

4.5.3 One-pot synthesis of 3-methyl indole via reductive amination of NB and acetol.

4.5.3.1 Effect of Pt metal loading.

Indoles are N-heterocyclic compounds commonly employed as scaffold for the synthesis of antibiotics, analgesics, antidiuretics, anti-inflammatory drugs and cancer treatments [169, 170]. Among them, 3-methylindole (3-ML) stands out for its wide spectrum application in medicine, acting as a privileged pharmacophore. Thus, here we propose it`s synthesis via one-pot reductive amination of NB and acetol (AC), Figure 26.

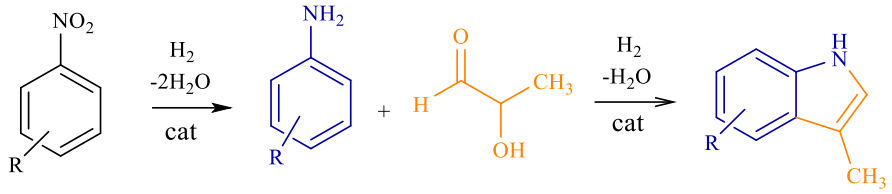

Figure 26. One pot simplified reaction schema for the synthesis of 3-ML from NB and Acetol. Self-elaboration.

Catalytic tests were performed using ethyl acetate, ethanol, and toluene as solvents, under varying substrate concentrations and temperatures. Among these, ethyl acetate exhibited the best performance at 100 °C, with a molar ratio of NB:Pt = 1000 and AC:NB = 2; consequently, all subsequent experiments were conducted using this solvent. Table 9 summarizes the catalytic performance indicators for the synthesis of 3-ML using Pt(x)/TNT-R catalysts (x = 0.125, 0.250, 0.500, 1.000 wt%).

The consumption of NB over time followed a pseudo-first-order kinetic model, with distinct rate constants for each catalyst, as shown in Figure S17 and Figure S18. Furthermore, the $TOF_{3\text{-ML}}$ values increased substantially with the Pt loading following the order 0.2, 1.4, 13.1, and 91.4 min^{-1}, indicating enhanced activity with increasing Pt particle size or surface restructuring. The carbon balance exceeded 90% for all catalysts, suggesting formation of minor unknown products. Notably, 1,2-propanediol, a typical product from AC hydrogenation, was not detected by GC-MS, while condensation products (e.g., hemiacetals, acetals) were present only in trace amounts ($S_{other} < 2.0\%$).

Table 9. Results of the catalytic activity for the obtention of 3-ML from NB and acetol, for the different Pt(%)/TNT-R catalyst.

Pt (%)	k_{ap} (min^{-1})	$TOF_{3\text{-ML}}$ (min^{-1})	Selectivity (%)[a]		CB (%)
			3-ML	AN	
Pt(0.125)/TNT-R	56.7	0.018	0.2	--	>99
Pt(0.250)/TNT-R	75.4	0.021	1.4	0.6	>99
Pt(0.500)/TNT-R	100	0.093	13.1	2.3	97.1
Pt(1.000)/TNT-R	100	0.115	91.4	25.4	74.2

Reaction conditions: ethyl acetate 50 mL, 50 mg of catalyst, 100°C, 10 bar H_2, Pt:NB 1:1000, AC:NB = 2:1, 700 rpm. [a]Reaction time: 60 min. [b]Selectivity determined at 20% of conversion.

Selectivity toward the target product 3-ML was highest for the Pt(1.000)/TNT-R catalyst, in contrast to trends observed in simple hydrogenation reactions. This suggests that hydrogenation and amination steps may occur on different active sites. Thus, the Pt(x)/TNT-R catalysts may exhibit bifunctionality, where Pt and the TNT-R support each facilitate distinct steps in the reductive amination mechanism. This functional interplay could enable the observed control over reactivity and selectivity. In the following sections, we further characterize the Pt(1.000)/TNT-R catalyst to propose a mechanistic rationale and provide a preliminary kinetic interpretation of the observed trends.

4.5.3.2 Structure-reactivity correlation of Pt(1.000)/TNT-R in NB reductive amination

To correlate the catalytic activity results with the physicochemical characteristics of the Pt(1.000)/TNT-R catalyst, a series of complementary characterization techniques was used. In addition, a control Pt(1.000)/TNT-C catalyst was prepared on the TNT-C support for comparison purposes. The HR-TEM micrographs and particle size distributions in Figure 11 & Figure S1 shows the existence of, single sites and NPs for the different catalysts, being the Pt-NPs the most relevant for Pt(1.000)/TNT-R. The mean particle size for this catalyst is 1.57 ± 0.35 nm, which was discussed previously as a consequence of the ability of O_V and Ti^{3+} species to coordinate Pt on the support surface. For the control catalyst Pt(1.000)/TNT-C, the HR-TEM characterization exhibited an average Pt particle size of 1.60 ± 0.42 (nm) (Figure S19), representing 63% of metal dispersion. Moreover, for this catalyst the ICP-OES confirmed the similarities between nominal and effective metal loadings (effective Pt loading = 0.73 Pt wt%). These similarities indicate comparable particle size between the Pt(1.000) catalysts supported on TNT-C and TNT-R. Therefore, the purpose of this comparison is to evaluate whether the $NaBH_4$-assisted reduction treatment introduces differences between the two catalysts beyond enabling the deposition of Pt as single sites. The FT-IR CO measured at –80°C was also performed for both catalysts to understand the presence of the different species of Pt and the results are presented in the Figure 27. The Pt(1.000)/TNT-R catalyst displayed a signal at 2188-2181 cm^{-1} corresponding to the mixed contribution of the -CO adsorbed linearly in terraces of Ti^{4+} and Ti^{3+} species at the support. At 2164 cm^{-1} and 2152 cm^{-1} it is seen the

characteristics band for the electronic deficient $Pt^{\delta+}$ species which depends on the coordination degree of the platinum species [152, 171, 172]. An increase in the coordination and in the oxidation state of the platinum generates a red shift to higher wavenumbers. Raw data ad different CO adsorption coverages is in Figure S20.

For Pt(1.000)/TNT-C, the most intense signal at 2177 cm^{-1} corresponds to Ti^{4+}. A shift to lower wavenumbers is attributed to the presence of Pt^0. Due to the relatively high Pt loading (1 wt%), the presence of metallic particles is significant in both materials. Signals around ~2080, 2050, and 2030 cm^{-1} are assigned, left to right, to CO adsorbed on Pt^0 particles at terrace, step, rim, and uncoordinated sites, respectively [149, 171, 173, 174].

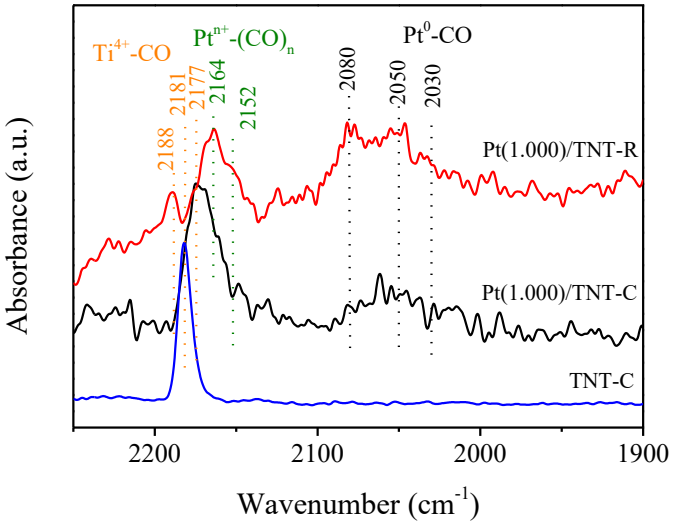

Figure 27. Low temperature FT-IR (FT-IR CO) for (A) Pt(1.000)/TNT-R, (B) Pt(1.000)/TNT-C.

The Figure 28 shows the results of the XPS analysis and the identification of the surface species in both Pt(1.000)/TNT-R and Pt(1.000)/TNT-C (See raw spectra in Figure S21 (A)). Moreover, Table 10 summarizes the binding energies and percentage of species resulting from the integrated peak areas. Both catalysts show the presence of reduced and oxidized Pt species, with a greater contribution of metallic sites.

Table 10. High resolution XPS band for Pt, Ti & O for the Pt(1.000)/TNT-R catalyst.

Catalyst	Pt $4f_{7/2}$ BE (eV)		Pt^{2+}/Pt^{0}	Ti 3s BE (eV)	Ti 2p BE (eV)		O1s BE (eV)	
	Pt^{0}	Pt^{2+}			Ti^{3+}	Ti^{4+}	O-Ti	O-H/TiO_x
Pt(1.000)/TNT-C	71.09 (79.29) 1.12[a]	72.17 (20.7) 1.60[a]	0.261	62.05	---	458.76	530.25 (97.11)	532.13 (2.89)
Pt(1.000)/TNT-R	71.12 (82.75) 1.50[a]	72.29 (17.24) 1.18[a]	0.208	62.17	457.83 (36.01)	458.43 (63.99)	529.72 (89.25)	531.79 (10.75)

In brackets the percentage of the species. [a]FWHM for the Pt $4f_{7/2}$

The peaks centred at 71.09 eV and 71.12 eV in Figure 28 (A) and (B) corresponds to the Pt $4f_{7/2}$ core level spectra of Pt. The peak at 72.29 eV for Pt(1.000)/TNT-R indicates the successful formation of stable oxidized Pt species. These species could correspond to Pt single sites, coordinated with O_V of the TiO_2 surface [175, 176].

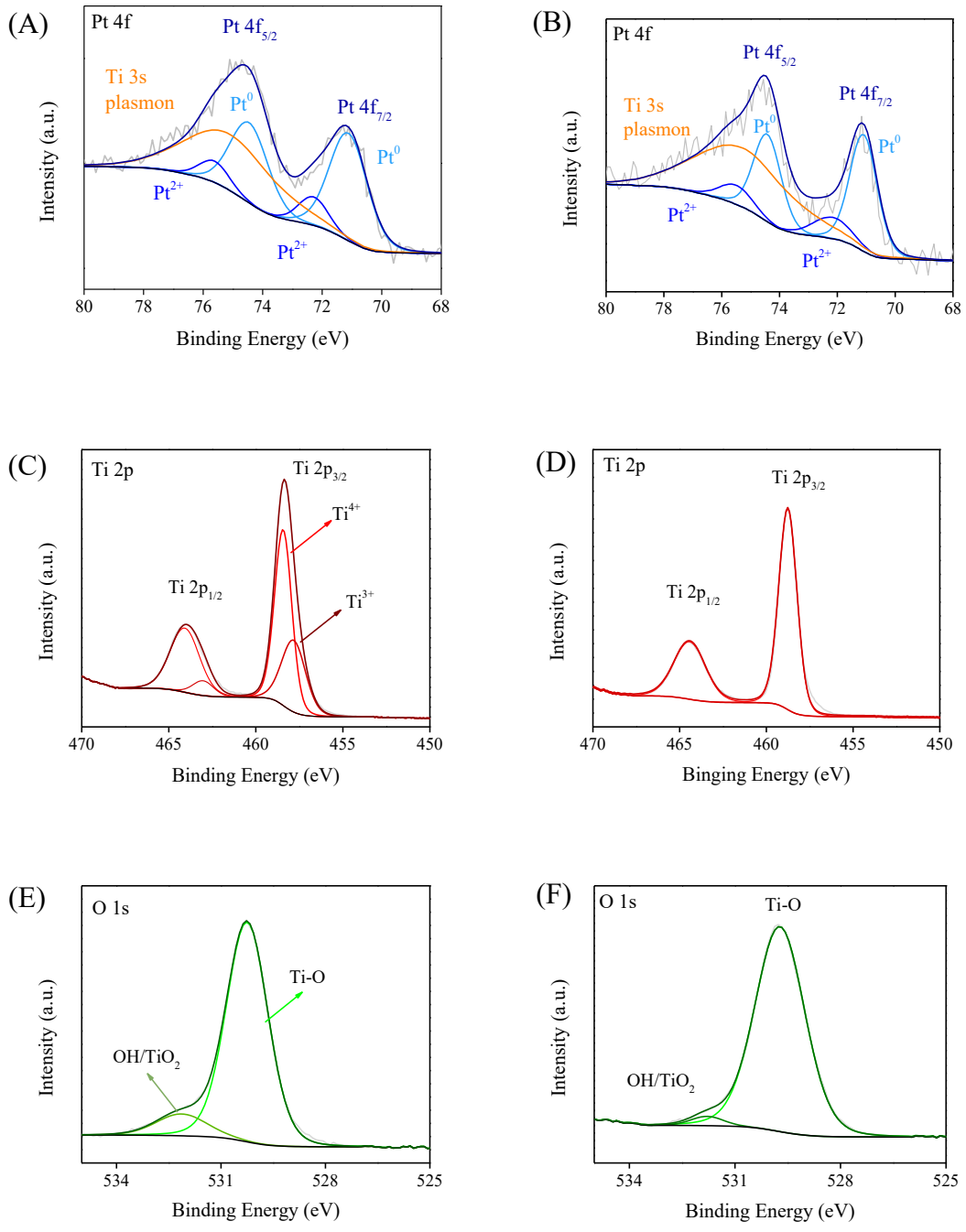

Figure 28. XPS analyses for the Pt(1.000)/TNT-R (A), (C) and (E) for Pt(1.000)/TNT-C. (B), (D) and (F).

The high-resolution Ti 2p spectra for both TNT-R and TNT-C supported catalyst are shown in Figure 28 (C) and (D). The Ti doublet of Ti $2p_{3/2}$ and $Ti2p_{1/2}$ arises from spin orbit-splitting centred at 458.76 eV 464.42 eV, assigned to Ti^{4+} species [60, 177] on TNT-C supported catalyst. After the reduction treatment (TNT-R), the spectrum shifted to lower B.E. of 458.43 eV for the Ti^{4+} species, and it showed a new contribution at 457.83 eV assigned to Ti^{3+} species on TNT-R supported catalyst. This reduction is expected due to the formation of O_V in the surface layer of the support [178].

Both systems show the shape for O1s spectra typical of titania (Figure 28 (E) and (F)). For the TNT-C supported catalyst, the main peak is located at 530.25 eV, which is in good agreement with the energy position for the O–Ti bond in TiO_2 [179]. The appearance of non-lattice oxygen OH/TiO_x is known for several oxides [180, 181], located at 532.13 eV. For the TNT-R supported catalyst, the B.E. of O-Ti species shifted slightly to 529.72 eV, whereas its area decreased to 89.25%, meanwhile an increase of 10.75% for the non-lattices was observed, in agreement with the generation of TiO_x defects. These results are consistent with the EPR (Figure 12), and FT-IR CO data (Figure 27), indicating that Ti^{3+} species and O_V play a significant role in stabilizing and promoting the formation of single Pt atoms on the catalyst supported on reduced titania. The sodium (Na 1S) was detected for both catalyst for Pt(1.000)/TNT-C a 1072.47 eV and for Pt(1.000)/TNT-R a 1072.54 eV, characteristic of cationic sodium species; no further analysis was made.

To assure a more accurate discussion of the XPS results on the Pt 4f region and to avoid an over consideration of the area of the Pt species, the contribution of the plasmon of Ti

3s was considered due to the overlapping of the plasmon with the signal of Pt 4f [182-186], a zoom to the XPS survey where the Ti 3s signal is identified is provided in Figure S21.

The FT-IR of pyridine was conducted (Figure 29) to evaluate the nature of the acid sites of the catalyst. The results indicate that the Pt(1.000)/TNT-R, contains Lewis's acid sites which are coordinated with pyridine (LPy) corresponding to the IR bands at 1606, 1574, 1489 and 1445 cm^{-1}. Moreover, characteristic bands are detected at 1591 and 1440 cm^{-1} corresponding to the presence of protonated pyridine (HPy). In the Pt(1.000)/TNT-C, apart from the LPy and HPy, the presence of Brønsted acid sites (BPy) is detected at 1542 cm^{-1} [187]. This result suggests that the Pt(1.000)/TNT-C exhibits greater propensity for acid-base interactions in comparison to the Pt(1.000)/TNT-R catalyst.

The presence of different acid sites could promote different interaction types between reactants or products with the catalyst surface, which eventually could increase the coverage of the surface and affect the activity and/or selectivity of the catalyst. Figure 29(B) presents the relationship between LPy and HPy. In this case, Pt(1.000)/TNT-R shows an LPy/HPy ratio of 0.65, indicating a lower population of Lewis acid sites, with LPy being less abundant than HPy. In contrast, Pt(1.000)/TNT-C exhibits an LPy/HPy ratio of 2.14, indicating a predominance of Lewis acid sites.

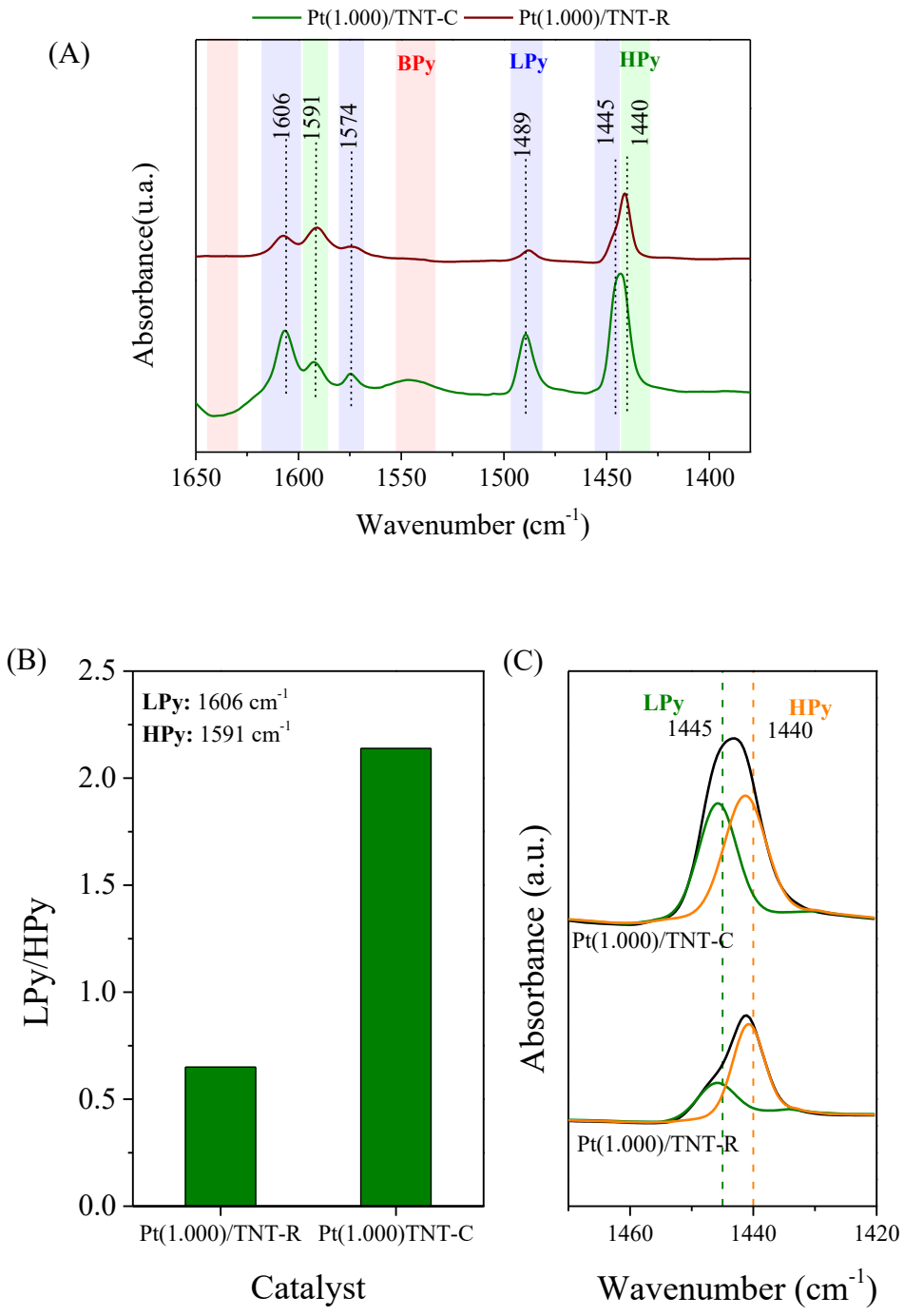

Figure 29. FT-IR spectra of adsorbed pyridine (A) Pt(1.000)/TNT-R and Pt(1.000)/TNT-C recording following a brief outgassing of at 150°C. (C-D) IR band position and the relativity intensities (LPy/HPy)

The higher presence of Lewis acid sites in Pt(1.000)/TNT-C can promote stronger and irreversible interactions with acetol through the –OH group and with aniline formed during NB conversion, thereby suppressing the condensation reaction and preventing the formation of 3-ML.

The strength of the acid sites in both catalysts was confirmed by TPD-NH_3 analyses (Figure S22). In this case, the results show that both catalyst present similar densities and strengths of acid sites, with a desorption peak at T° < 300°C corresponding to weak acidity [166, 167]. In the case of Pt(1.000)/TNT-R show a wide and small signal corresponding to a total chemisorbed ammonia of 5.24 $mmol_{NH_3}\ g^{-1}$ corresponding to 20 $\mu mol_{NH_3}\ m^{-2}$, whereas Pt(1.000)/TNT-R displayed a total chemisorbed ammonia of 4.95 $mmol_{NH_3}\ g^{-1}$ equivalent to 16.20 $\mu mol_{NH_3}\ m^{-2}$. The modification with $NaBH_4$ not only affect the deposition of the platinum due to the engineering defect generation but also modifies the acidity of the catalyst, in nature and in density. The Pt(1.000)/TNT-R display majority of protonated pyridine HPy acid sites and 3-fold acid sites density over Pt(1.000)/TNT-C who display mainly Lewis acid sites (LPy), this difference also saw for Pt(0.125)/TNT-R(C) catalyst for FFA synthesis (4.5.2.2), this difference also affect in the synthesis of 3-ML as is discussed below.

4.5.3.3 Proposed reaction scheme for NB and AC reductive amination

To propose a preliminary reaction scheme consistent with the one-pot reductive amination of NB and AC; several catalytic tests at varying temperatures were conducted using Pt(1.000)/TNT-R and the same H_2 pressure, solvent, Pt:NB:AC molar ratio and catalyst

mass as discussed before in section 4.5.3.1. The NB conversion as a function of time was evaluated in presence and absence of AC to discard a competitive role with NB for the metallic sites responsible of the hydrogenation. The Arrhenius plot in Figure S23 was constructed using the rate constants (k_{ap}) determined from a pseudo-first order kinetic model (Figure S24). The E_{aa} calculated for the NB hydrogenation in presence of AC to obtain 3-ML in a one-pot approach was 31.1 $kJ \cdot mol^{-1}$ for Pt(1.000)/TNT-R. However, the same study conducted in the absence of AC displayed an Ea_{ap} for the hydrogenation of NB of 28.0 $kJmol^{-1}$ suggesting that the AC does not interfere in the hydrogenation of NB.

For comparison purposes, the Pt(1.000)/TNT-C catalyst was used as control to evaluate the effect of the TNT support on this reaction. The NB conversion curves are shown in Figure S25 and the kinetic results are shown in the Table 11. Both systems are active in the NB hydrogenation reaching $k_{ap,NB}$ for Pt(1.000)/TNT-R 2.3-fold higher than the $k_{ap,NB}$ for the Pt(1.000)/TNT-C. However, the selectivity toward 3-ML showed a significant difference between the catalysts. The Pt(1.000)/TNT-R catalyst achieved a selectivity of 25.4% toward the target product at isoconversion (20%), whereas the Pt(1.000)/TNT-C catalyst exhibited negligible formation of 3-ML (<1.0%).

Table 11. Catalytic data for the obtention of 3-ML from the one-pot synthesis of NB and AC.

Catalyst	X_{NB} (%)[a]	$k_{ap, NB}$ (min^{-1})	$S_{3\text{-ML}}$ (%)	S_{AN} (%)[b]	$TOF_{3\text{-ML}}$ min^{-1}	CB
1% Pt/TNT-C	87.0	0.057	---	64.6[C]	--	>98
1% Pt/TNT-R	99.2	0.115	25.4	82.4	121.4	>98

Reaction conditions: ethyl acetate 50 mL, 50 mg of catalyst, 100°C, 10 bar H_2, Pt:NB 1:1000, AC:NB 2:1, 700 rpm. [a]Reaction time: 60 min. [b]Calculated at 20% conversion.[c]At lower conversion the hydrazobenzene is formed as an intermediate of the reaction.

In line with the studies of Su et al. [116] and Sun et al. [117], the synthesis of 3-ML proceeds by the reaction map represented in Figure 30. Moreover, these authors demonstrate that this reaction is promoted by the presence of weak-acid sites centres, which could explain the outstanding performance observed for Pt(1.000)/TNT-R in the one-pot reductive amination of NB and AC. In addition, both catalysts exhibited a similar distribution of Pt particles; however, Pt(1.000)/TNT-R also showed the presence of isolated Pt sites, as confirmed by HR-TEM and FTIR-CO characterization at -80°C. These findings suggest that, under conditions of weak interaction with acid sites (as indicated by HPy signals), the selectivity toward 3-ML formation is favoured. Also, the presence of isolated sites, and Pt nanoparticles appears to enhance the hydrogenation of NB.

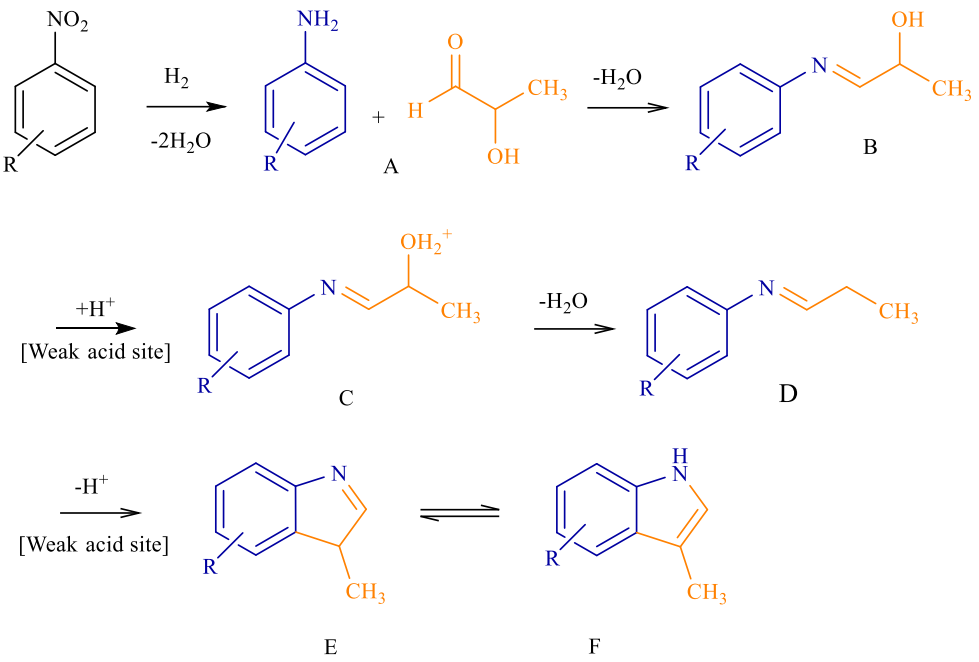

Figure 30. Proposed mechanism for the one-pot reaction between NB and AC for the obtention of 3-ML. Adapted from [188].

For the Pt(1.000)/TNT-C catalyst, the negligible formation of 3-ML is likely due to the involvement of Lewis acid sites (LPy) in the strong adsorption of AC on the catalyst surface. The AC molecule contains both a carbonyl (C=O) group and a hydroxyl (-OH) group at the α-position. Of these, the hydroxyl group acts as a stronger electron donor, while the carbonyl group is primarily electron-withdrawing. As a result, the -OH group interacts preferentially with Lewis acid sites, leading to strong and possibly irreversible adsorption. This interaction may hinder the activation of the C=O group, thereby blocking imine formation, which is a key intermediate in the synthesis of 3-ML.

4.5.3.4 Recyclability

The rational design of a catalyst must account for its long-term stability and recyclability, particularly for industrial applications. To assess this, 10 consecutive reaction cycles were carried out using Pt(1.000)/TNT-R.

The results shown in Figure 31 illustrate the NB conversion and selectivity toward AN and 3-ML during the recycling tests. The catalyst initially exhibited excellent performance, maintaining NB conversion near 98%. However, a gradual loss of activity was observed after the sixth cycle, with conversion dropping sharply from 98.03% to 23% by the tenth cycle. Selectivity towards 3-ML remained relatively stable up to the sixth cycle but then declined significantly, reaching 15% in the final cycle.

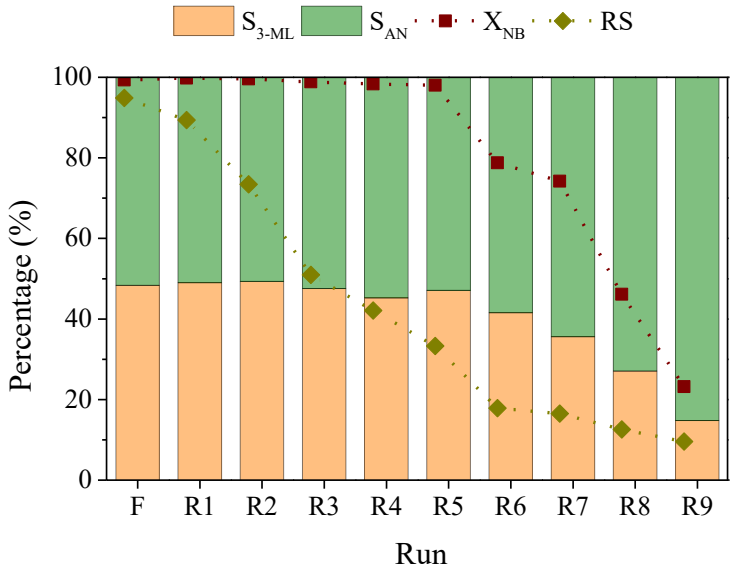

Figure 31. Recyclability experiments for the system Pt(1.000)/TNT-R. 10 bar of H_2 pressure, 100°C of temperature, 50 mg of catalyst with a molar ratio nitrobenzene/Pt = 1000.

Catalyst deactivation was further supported by recycling stability (RS, equation 8, section 0) measurements, which showed a continuous decrease, reaching a minimum of 1.90 % by the last cycle. This trend confirms a significant loss in both catalytic activity and selectivity toward 3-ML, likely due to structural or surface changes during repeated use.

To investigate the causes of catalyst deactivation, post-reaction characterizations were performed using ICP-OES and HR-TEM. These analyses allowed to rule out Pt leaching and structural changes of the single site catalysts or Pt nanoparticles, respectively. The ICP-OES results showed that the Pt content remained nearly unchanged after 10 cycles (~0.68 wt%), indicating negligible metal leaching. In contrast, the HR-TEM micrographs (Figure 32) revealed particle restructuration and a noticeable increase in Pt-NP size, with the average diameter shifting to 7.1 ± 1.5 nm. This suggests that agglomeration of isolated sites into larger Pt NPs occurred during the reaction, contributing to the observed loss in catalytic activity, particularly for the hydrogenation step.

Additionally, the reductive amination of NB with AC produces 1 mol of 3-ML and 4 mol of H_2O, respectively. As previously discussed, the presence of water under reaction conditions can promote Ostwald ripening [161], a phenomenon in which smaller metal species dissolve and redeposit onto larger particles. This process is likely driven by solvothermal, or hydrothermal conditions present at the reaction temperature and contributes to the deactivation of metal centres by promoting Pt particle growth and loss of active surface area.

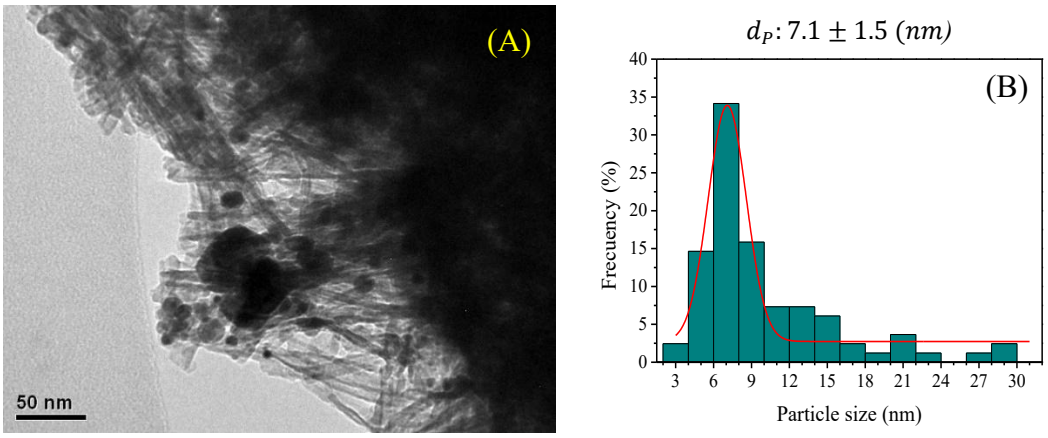

Figure 32. (A) High resolution microscopy post recycling test of Pt(1.000)/TNT-R for one-pot reductive amination of NB + AC to produce 3-ML and (B) Particles distribution histogram for the HR-TEM characterization.

Finally, as was discussed in the previous section, the Bronsted acidity promoted the formation of the 3-ML over the Pt(1.000)/TNT-R catalyst. Solvothermal/hydrothermal reactions in the liquid phase could promote the change in the support's acidity by the solid hydration or formation of other species based on Ti-OH, which could be detrimental to the production of the target product. However, other characterizations such as Raman spectroscopy, XRD, among others, are required to sustain this hypothesis.

4.5.3.5 Evaluation of substituted nitroarenes in the one-pot reductive animation to produce 3-methyl-indoles

To explore the versatility of the Pt(1.000)/TNT-R catalyst for the reductive amination of different N-sources, a substrate survey of *para* substituted nitroarenes was carried out in the one-pot reductive amination of NB and AC. The same experimental conditions as for catalysts screening and recyclability were applied for these experiments (section 4.5.3.1).

The results of these experiments are summarized in Table 12. The Pt(1.000)/TNT-R catalyst was active for the hydrogenation of all the nitroarenes, reaching almost complete conversion after 180 min. The data was adjusted to a pseudo-first kinetic order, and the apparent kinetic constant is presented in Table 12 ($k_{ap,p\text{-}NB}$).

In terms of the hydrogenation step the trend in k_{ap} and selectivity to desired amines, shows that electron-withdrawing groups favoured the hydrogenation of the *p*-NB whereas the selectivity of the target 5 substituted 3-ML (5,3-ML) product decreased, reaching negligible values for *p*-dinitrobenzene. The product distribution only displayed the formation of *p*-AN intermediate along with the 5,3-ML. Other intermediates were not detected, which let us suggest that the rate-limiting step is the production of *p*-AN. In addition, the cyclization step (intermediate E according to Figure 30) involves the electrophilic aromatic substitution (SEA) on the phenyl ring with the elimination of the H^+ where the electron-withdrawing (EWG) limited the addition in the *ortho* position respect to the $-NH_2$ group, which can provide a plausible explanation for the decrease in the $S_{5,3\text{-}ML}$. A different trend is observed in the case of -F, $-CH_3$ and $-OCH_3$ for the hydrogenation of *p*-NB and the production of the target 5,3-MLs. The presence of -F decreased the $k_{ap,p\text{-}NB}$ compared to NB hydrogenation for the formation of target product, while the selectivity increased reaching $S_{5,3\text{-}ML} > 40\%$. Fluorine substituent is highly electronegative, pulling electron density away from the benzene ring through the sigma σ bond, making the ring electron-poor and slowing down SEA step in the formation of the target product [189, 190].

Table 12. Kinetic parameters for the one-pot reductive amination of *p*-substituted nitrobenzenes and AC to produce 5,3-ML over Pt(1.000)/TNT-R catalyst.

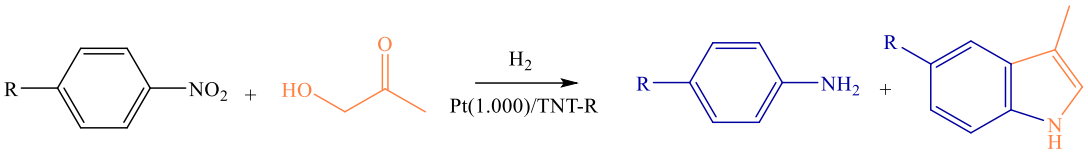

Substituent	$X_{Nitroarene}$ (%)[a]	$S_{5,3\text{-ML}}$ (%)[b]	S_{AN} (%)[b]	$k_{ap,NB}$ (min^{-1})	$TOF_{5,3\text{-ML}}$ (min^{-1})	CB (%)
NO_2	100	--	94.7[c]	0.492	--	>99
CN	100	0.3	85.6	0.303	1.4	>99
Cl	100	2.6	88.2	0.256	9.6	>98
F	98.4	40.5	59.9	0.133	94.1	>98
H	100	25.4	74.2	0.115	91.4	>98
CH_3	71.9	68.1	30.9	0.069	67.1	>97
OCH_3	47.2	82.2	17.5	0.009	10.6	>98

Reaction conditions: 10 bar of H_2 pressure, 100°C of temperature, 50 mg of catalyst with a molar ratio *p*-nitroarene/Pt = 1000. [a]Reaction time: 180 min. [b]Calculated at 20% conversion.

The -CH_3 and -OCH_3 electron-donating groups exerts a destabilizing effect on the transition state of the rate-limiting reaction to produce the corresponding *p*-AN, thus explaining the sensitivity of this reaction to these substituents. However, the electron-

donating effect increased the selectivity to the target product because these groups enhance the cyclization step promoting the SEA in the *ortho* position respect to the -NH_2 group. Thus, our results provide the basis for future studies dealing with electronic nature effects on the catalytic performance of metal-based catalytic systems.

5. CONCLUSIONS.

This PhD research focused on developing a simple and cost-effective strategy for the synthesis of platinum single site and nanoparticle catalysts supported on reduced TiO_2 nanotubes (TNT-R), while establishing clear structure-performance relationships in hydrogenation reactions of both industrial and biomass-derived relevance.

The proposed synthesis methodology successfully induced oxygen vacancies in TiO_2 nanotubes, generating well-defined coordination environments that enabled the stabilization of platinum as isolated single sites at low metal loadings. Comprehensive physicochemical characterization confirmed the coexistence and controlled evolution of Pt species as a function of metal loading. As the Pt content increased from 0.125 to 1.000 wt%, the population of isolated Pt single sites progressively decreased, while the formation of Pt nanoparticles became dominant, highlighting the critical role of metal-support interactions in governing Pt nuclearity, the preparation of different metal contents allows to reveal the influence of the metal loading and the capacity of the support produce single sites and NPs.

The single site-rich catalyst Pt(0.125)/TNT-R demonstrated outstanding catalytic performance in the hydrogenation of nitrobenzene, serving as a model reaction. This system exhibited the highest apparent rate constants, turnover frequencies, and recyclability over six consecutive cycles, together with a broad substrate scope toward substituted nitrobenzenes. Compared to the control catalyst Pt(0.125)/TNT-C, the

enhanced activity and stability clearly validated the initial hypothesis, confirming the beneficial role of oxygen-vacancy-anchored Pt single sites.

Beyond conventional hydrogenation, Pt(0.125)/TNT-R proved to be highly effective in the one-pot reductive amination of nitrobenzene with furfural, enabling the valorisation of a biomass-derived platform molecule. In ethanol, this catalyst delivered the highest activity, selectivity, and recyclability among the studied systems and showed competitive TOF values relative to state-of-the-art catalysts. The system also displayed versatility toward the synthesis of secondary aromatic amines from substituted nitrobenzenes. Detailed characterization revealed that differences in Pt speciation (single sites, and nanoparticles), together with the tailored Lewis acidity of the TNT-R support, play a decisive role in promoting cooperative catalytic pathways. Temperature-dependent kinetic studies further demonstrated that furfural does not competitively inhibit nitrobenzene hydrogenation, reinforcing the robustness of the bifunctional catalytic mechanism.

At higher metal loading, the Pt(1.000)/TNT-R catalyst emerged as the most efficient system for the one-pot conversion of nitrobenzene and acetol into 3-methylindole, a high-value heterocyclic compound. This catalyst exhibited the highest activity and selectivity among all Pt(%)/TNT-R systems and maintained stable performance over ten consecutive reaction cycles. Moreover, it showed versatility toward the synthesis of substituted 3-methylindoles from different nitrobenzene derivatives. In contrast, the control catalyst Pt(1.000)/TNT-C was inactive for this transformation, underscoring the critical role of the reduced TNT support. Spectroscopic analysis identified weak Brønsted acid sites as key

contributors to the selective formation of the indole framework, highlighting the importance of metal-acid synergy.

Post-reaction characterization revealed that catalyst deactivation is primarily associated with the structural evolution of Pt single sites into nanoparticles via Ostwald ripening. Additional experiments demonstrated that water generated as a by-product during reductive amination reactions accelerates this structural transformation, thereby reducing catalyst stability upon recycling. These findings provide fundamental insights into the dynamic nature of single sites catalysts under liquid-phase hydrogenation conditions and establish clear guidelines for future catalyst design strategies aimed at improving hydrothermal stability.

Overall, this thesis demonstrates that rational control over Pt nuclearity and support surface chemistry enables the design of highly active, selective, and recyclable catalysts for both conventional hydrogenation and biomass-assisted one-pot synthesis routes, contributing valuable knowledge to the field of single sites catalysis and sustainable chemical transformations.

This thesis lays a solid foundation for rationally designing singles site-nanoparticle catalysts with tuneable nuclearity and tailored support chemistry. Moving forward, combining structural stabilization, expanded reaction scope, mechanistic insight, and industrial applicability will enable the development of highly efficient, robust, and sustainable catalytic systems, pushing the frontiers of single site catalysis and biomass-based chemical transformations.

6. SCIENTIFIC PRODUCTION.

Articles directly related to co-direction agreement between the university of Concepcion and Toulouse-INP.

- **E. Leal-Villarroel**, D. González-Vera, M.E. Domine, D. Gómez, P. Serp, C.H. Campos, C.C. Torres, Platinum single sites supported on defected hydrogen-titanate nanotubes as selective catalyst for tandem synthesis of 3-methylindoles from nitrocompounds and acetol, Catalysis Today, 460 (2025).
- **E. A. Leal-Villarroel**, C. Marcelot, C. C. Torres, K. Soulantica, C. H. Campos, P. Serp. Toward decorrelation of surface oxygen groups from metal dispersion effects in Pd/C hydrogenation catalysts. Catalysis Science & Technology, **15**, 2034 (2025).

Other papers in collaboration:

- S. Bedoya, D. González-Vera, **E. Leal-Villarroel**, F. Gracia, M. E. Domine, G. Pecchi, C. C. Torres, C. H. Campos. Organo-modified halloysite nanotubes as supports for gold nanoparticles as highly recyclable catalyst for hydrogenation of nitroarenes. Inorganic Chemistry Communications 182 (2025) 115559.
- D. González-Vera, **E. Leal-Villarroel**, T. M. Bustamante, J.N. Díaz de León, L. Camarena, M. E. Domine, C. C. Torres, C. H. Campos. Bimetallic Nickel and Cobalt nanoparticles supported on TiO_2 as catalyst for the synthesis of 2-substituted benzimidazole by reductive amination-cyclization of 2-nitroaniline and aldehydes. Catalyst Today 459 (2025).

- S. Bedoya, D. González-Vera, **E. A. Leal-Villarroel**, J. N. Díaz de León, M. E. Domine, G. Pecchi, C. C. Torres, C. H. Campos. Palladium Nanoparticles Immobilized on the Amine-Functionalized Lumen of Halloysite for Catalytic Hydrogenation Reactions. Catalyst 15 (2025).

Participation in congress, schools and international events:

- **E. Leal-Villarroel**, C. C. Torres, C. H. Campos, L. E. Arteaga-Perez, P. Serp. Single Atom Systems – Pt Nanoparticles Supported on Partially Reduced Titanium Nanotubes for the Selective Hydrogenation of Nitroarenes. Oral presentation, XIII Chilean Catalysis and Adsorption conference, Linares 19-21, Nov, 2025, Chile.
- **E. A. Leal-Villarroel**, C. Marcelot, C. C. Torres, K. Soulantica, C. H. Campos, P. Serp. Pd/CNT Catalysts For Selective Hydrogenation Of Alkynes: Role Of Surface Oxygenated Functional Groups In Dispersion And Activity. **Poster** presentation, XIII Chilean Catalysis and Adsorption conference, Linares 19-21, Nov, 2025, Chile.
- **E. Leal-Villarroel**, C. C. Torres, C. H. Campos, P. Serp. Platinum Single Atom Catalysts supported on titania nanotubes for the Hydrogenation of Nitroarenes. **Oral presentation,** XXIX Iberoamerican congress of chemistry, 22-27 September, 2024, Bilbao, Spain.
- Assistance to Summer School, Catalyst From Understanding To Aplications 2024, Albi, France", **Flash oral presentation and poster presentation**. 17-21, June, 2024, Albi, France.

- **E. Leal-Villarroel**, C. C. Torres, C. H. Campos, P. Serp. Iridium nanoparticles deposited onto nanotubes supports for the hydrogenation of nitrobenzene: Effect of the support nature. **Poster presentation**, XV European congress on catalysis, August 27-september 1, 2023, Prague, Czech Republic.
- Assistance to Grow 4energy summer school" Technische Hochschule Deggendorf, 20-28 September, 2022 – 28/08/222, Deggendor, Germany.

7. SUPPORTING INFORMATION.

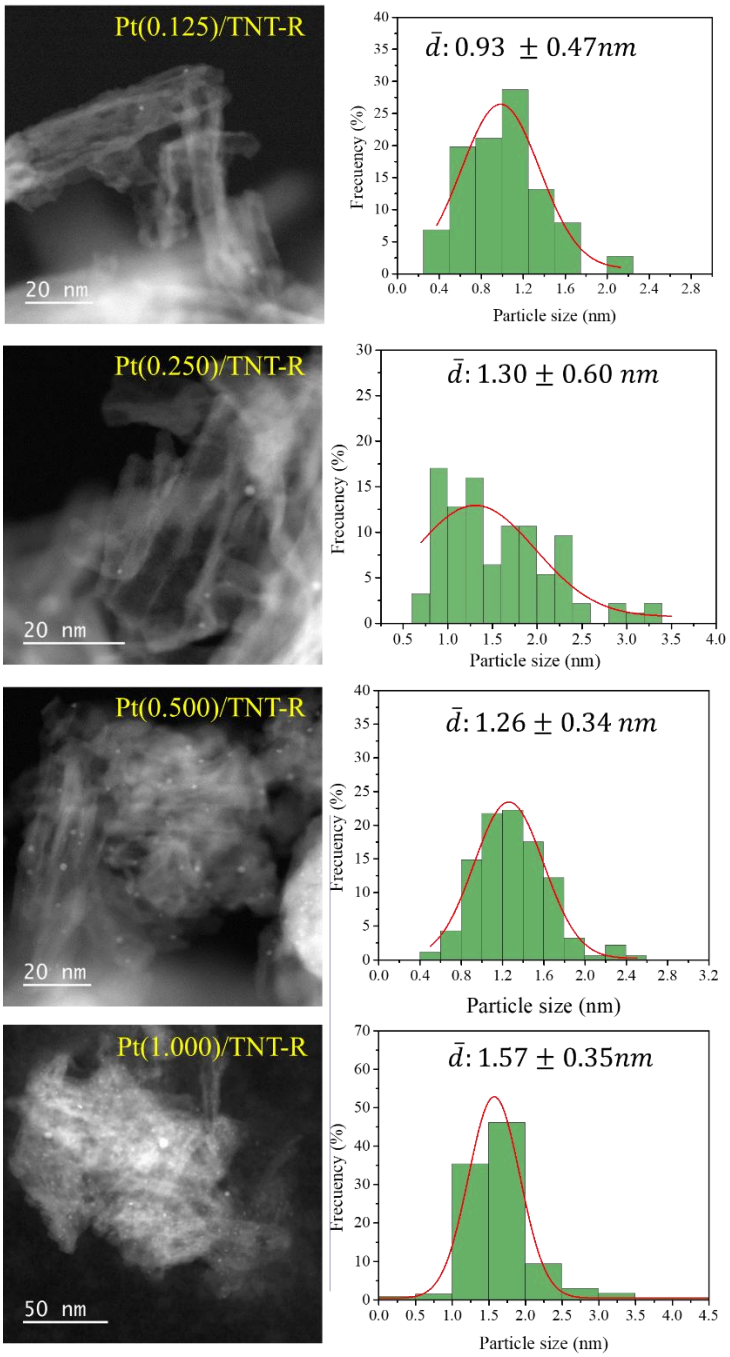

Figure S1. Particle size determination from HR-TEM analyses for the Pt(%) TNT-R catalyst.

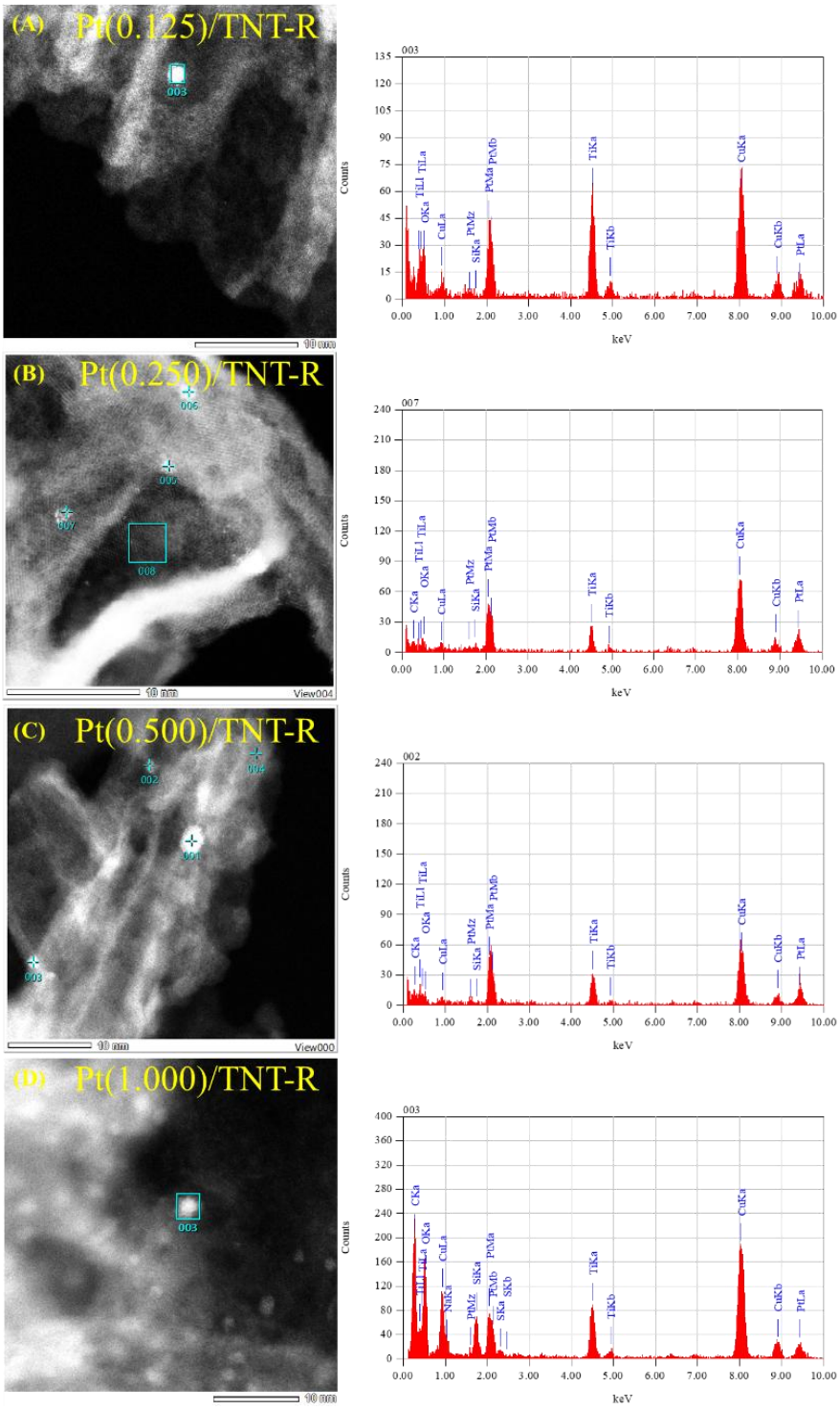

Figure S2. EDX analyses for the Pt(%)/TNT-R catalyst.

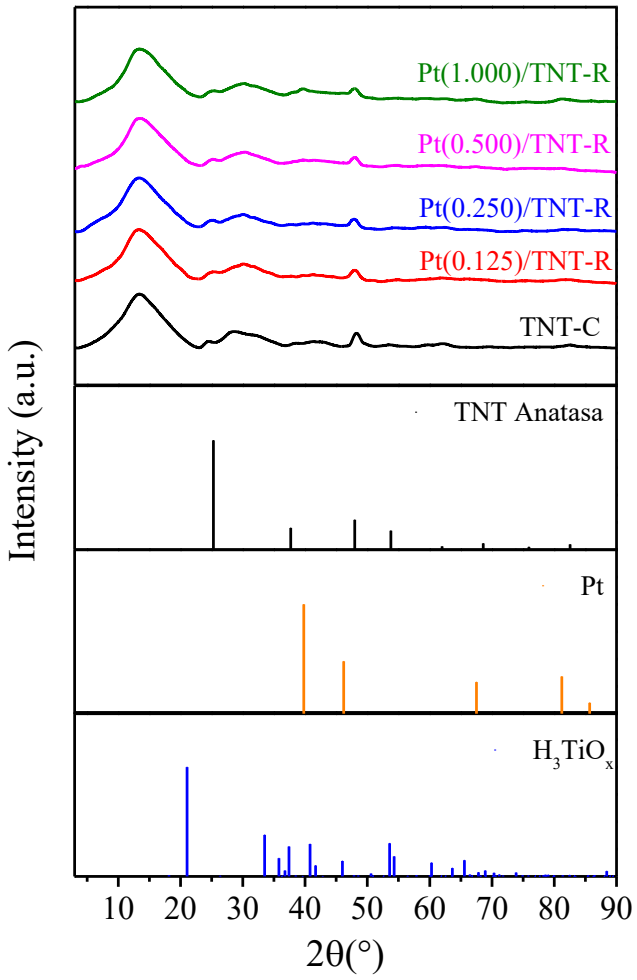

Figure S3. XRD analyses for the TNT-C support and representative Pt(%)/TNT-R catalysts.

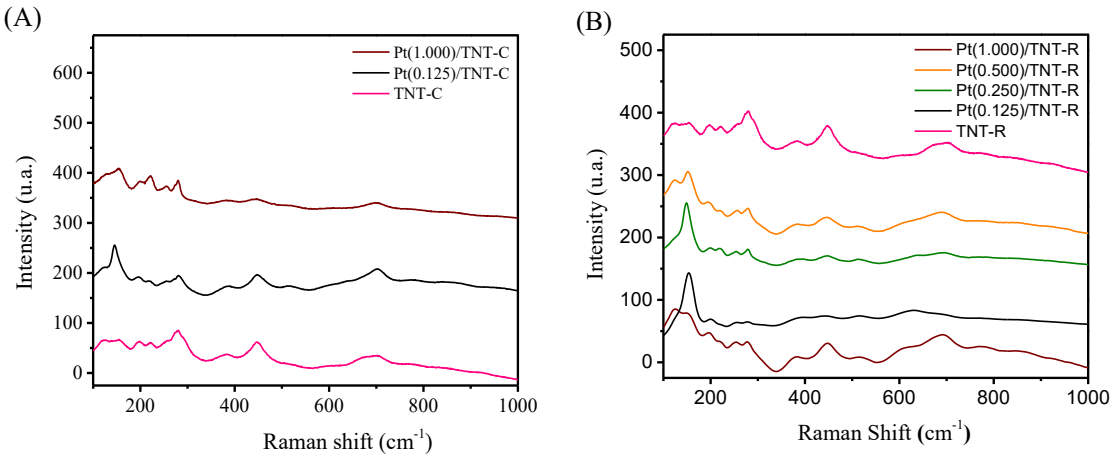

Figure S4. Raman analyses (A) for TNT-C and Pt(%)/TNT-C, (B) for TNT-R and Pt(%)/TNT-R catalysts.

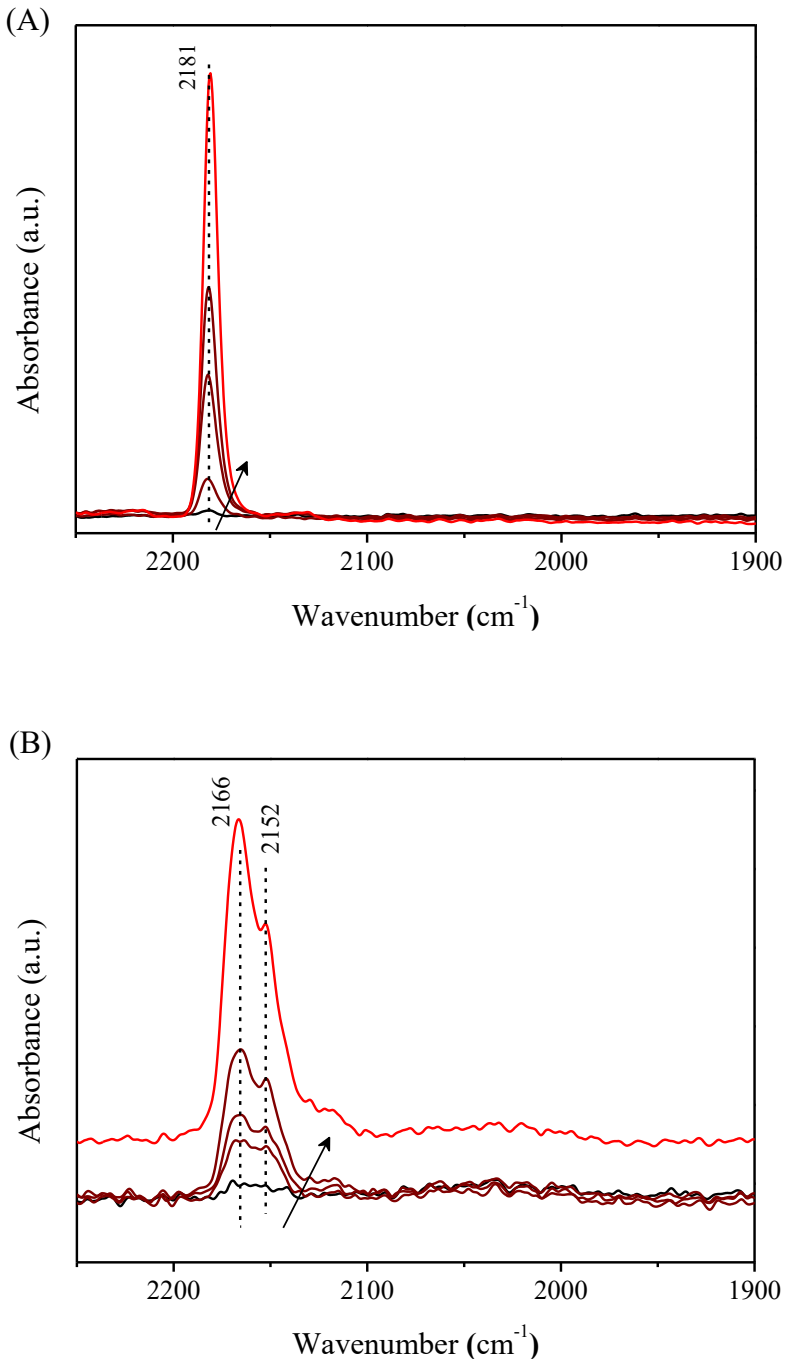

Figure S5. Low CO FT-IR at -80°C adsorption evolution spectra for (A) TNT-C and (B) Pt(0.125)/TNT-R.

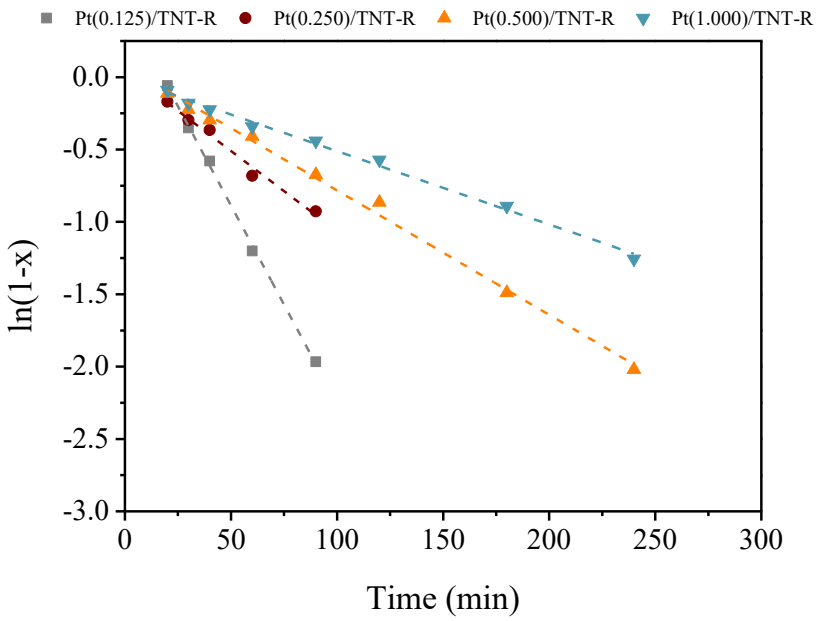

Figure S6. Pseudo-first order adjustment for the NB hydrogenation over Pt(0.125)/TNT-R. 30°C, 10 bar H_2, 700 rpm, 50 mg of catalyst, 30 mL ethanol, Pt:NB: 1:6000.

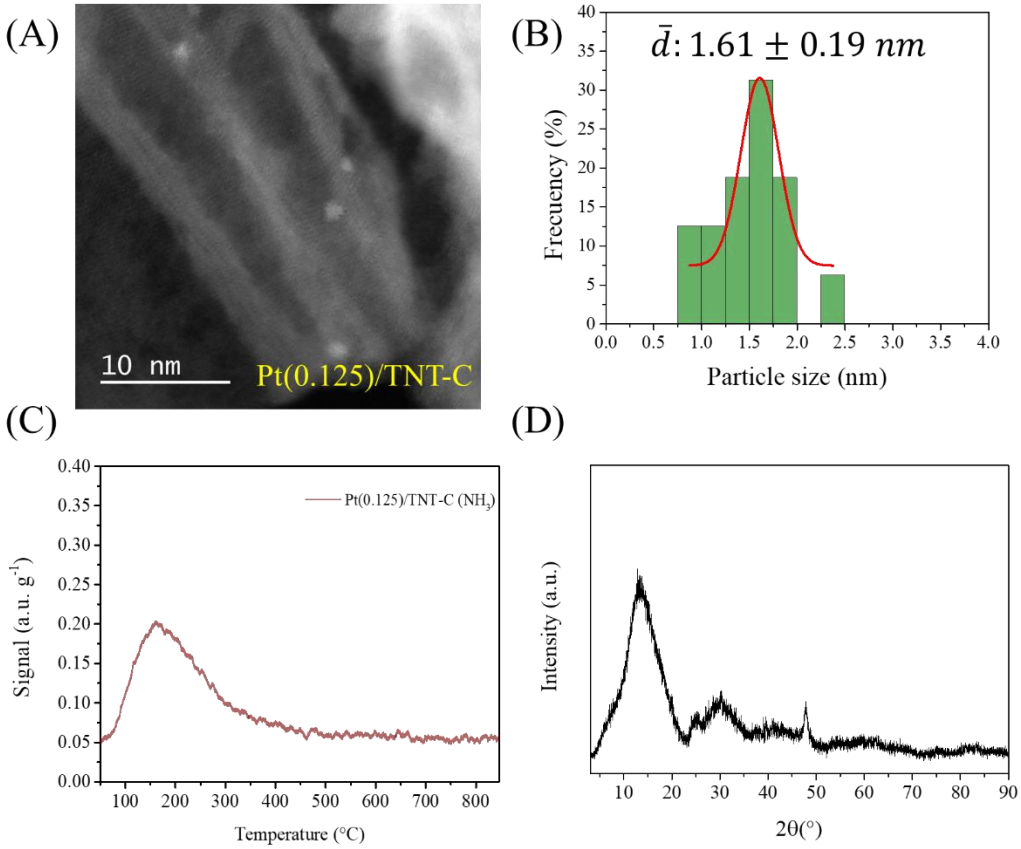

Figure S7. Characterization for the Pt(0.125)/TNT-C catalyst. (A) HR-TEM micrograph, (B) particle size distribution, (C) ammonia TPD, and (D) DRX profile.

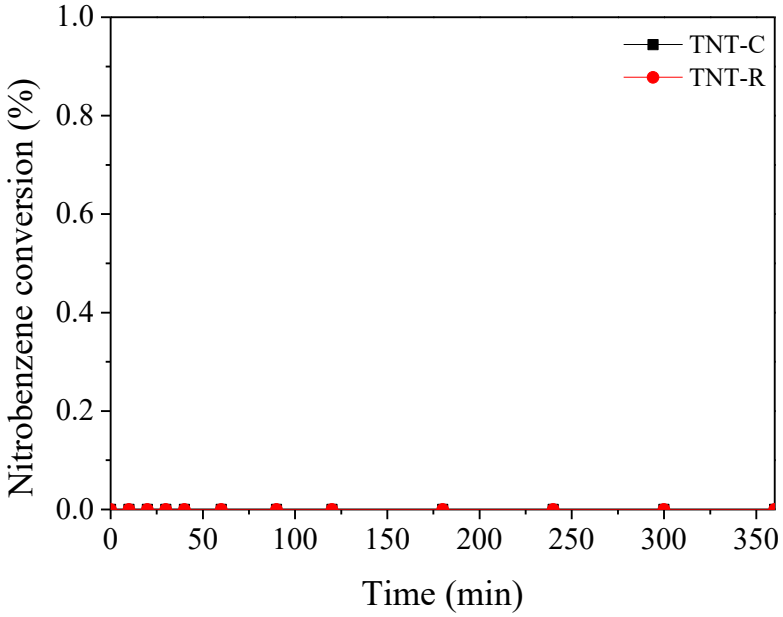

Figure S8. Control test for the nitrobenzene hydrogenation over TNT-C and TNT-R support in the absence of Pt. 30°C, 10 bar H_2, 700 rpm, 50 mg of catalyst, 30 mL ethanol.

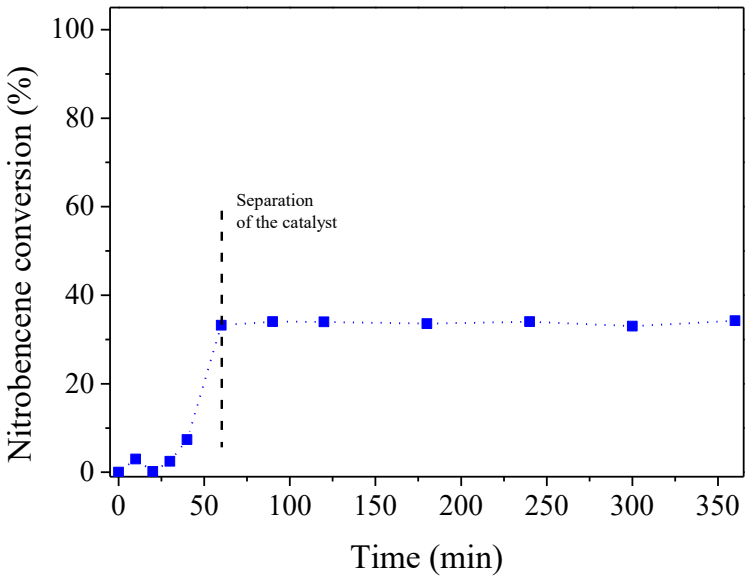

Figure S9. A hot filtration test was conducted for Pt(0.125)/TNT-R in NB hydrogenation, in which the catalyst was separated from the reaction mixture 60 minutes after the reaction commenced.

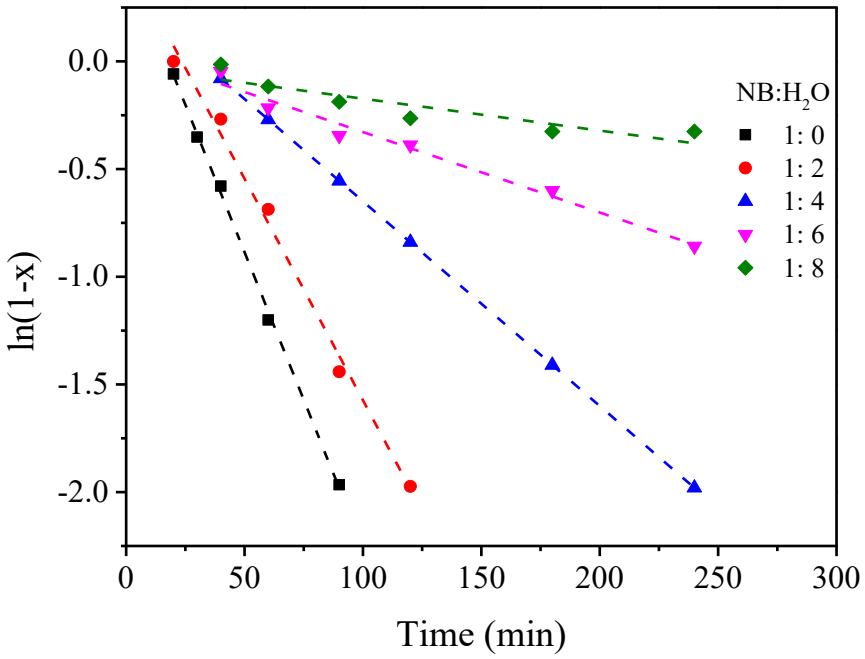

Figure S10. Pseudo-first-order correction applied to account for the effect of the water-to-NB molar ratio.

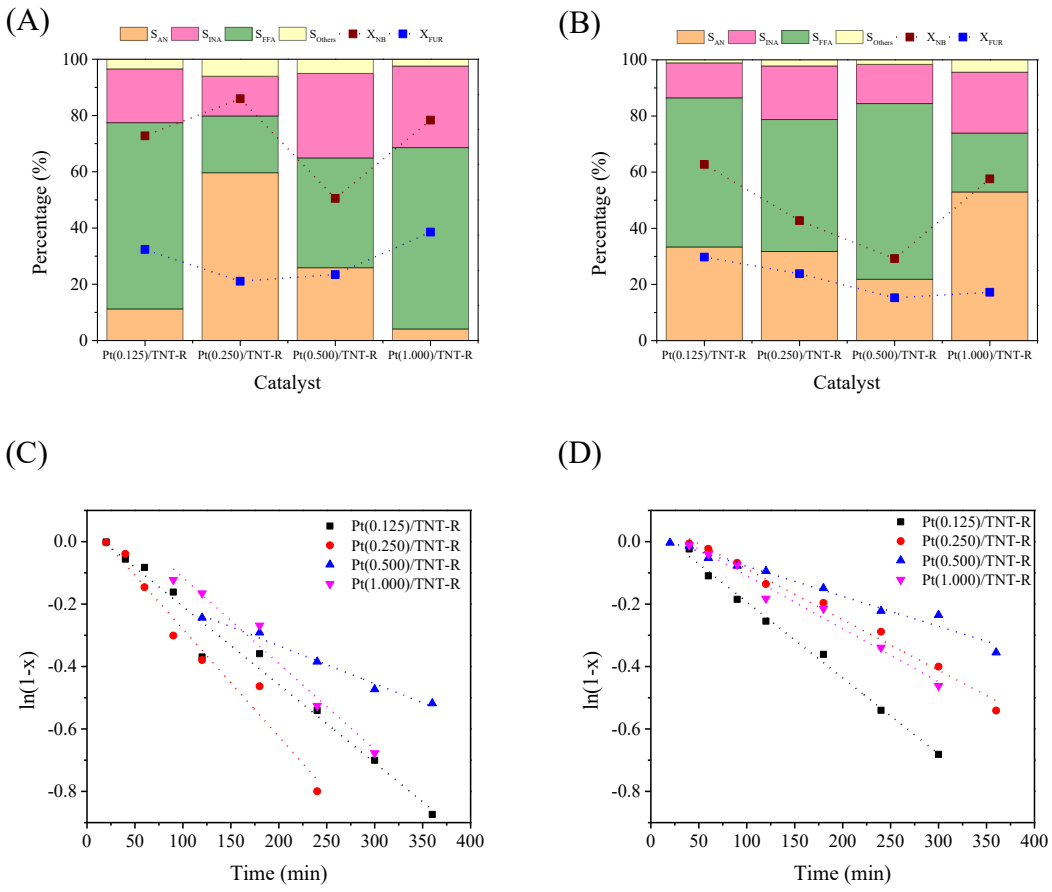

Figure S11. Study of the solvent effect on the one-pot synthesis of nitrobenzene and furfural over Pt(%)/TNT-R catalysts: (A) in ethanol, (B) in ethyl acetate, and (C) and (D) pseudo-first-order adjustment for NB conversion in ethanol and ethyl acetate, respectively. 30°C, 10 bar H_2, 700 rpm, 50 mg of catalyst, 30 mL solvent, Pt:NB:FUR 1:6000.

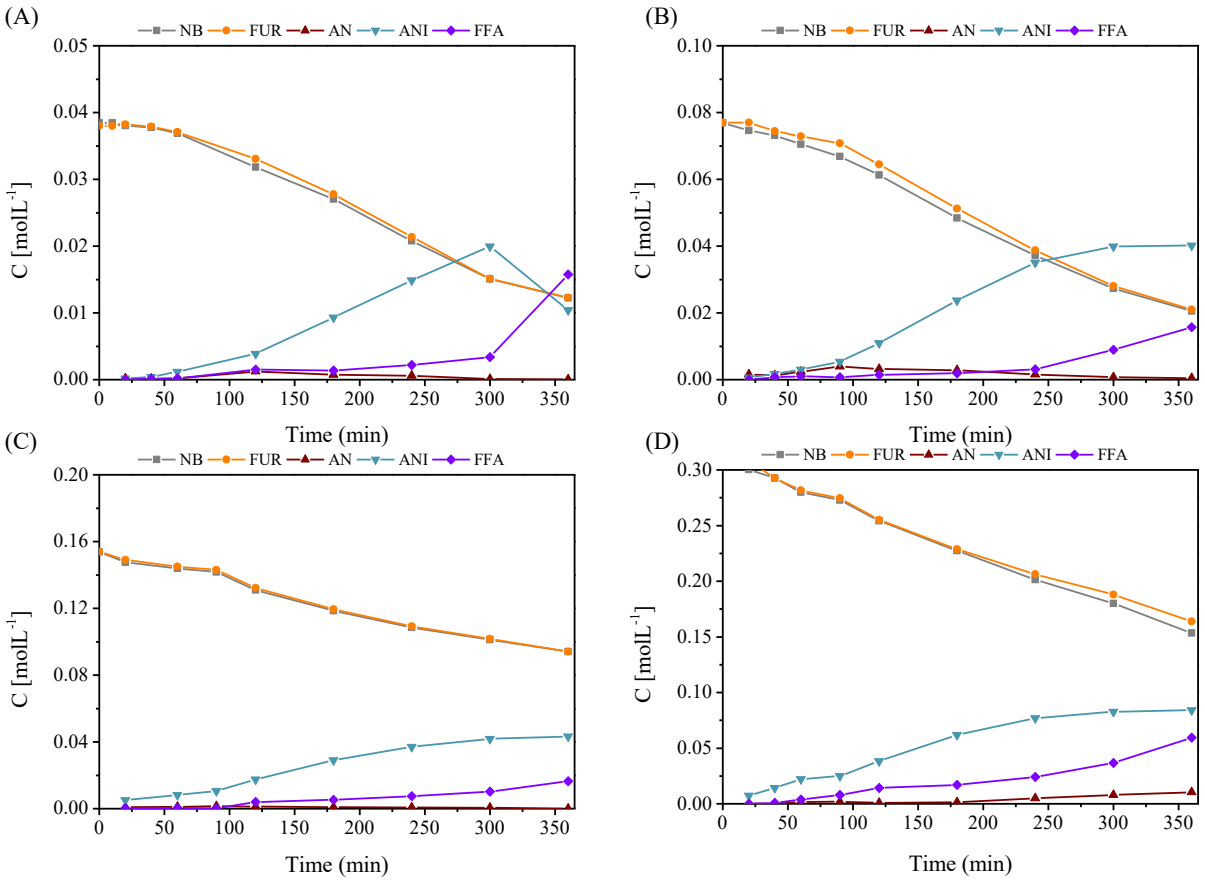

Figure S12. Product distribution for the one-pot synthesis of FFA from NB and FUR. (A) Pt(0.125)/TNT-R, (B) Pt(0.250)/TNT-R, (C) Pt(0.500)/TNT-R and (D) Pt(1.000)/TNT-R. 30°C, 10 bar H_2, 700 rpm, 50 mg of catalyst, 30 mL ethanol, Pt:NB:FUR 1:6000.

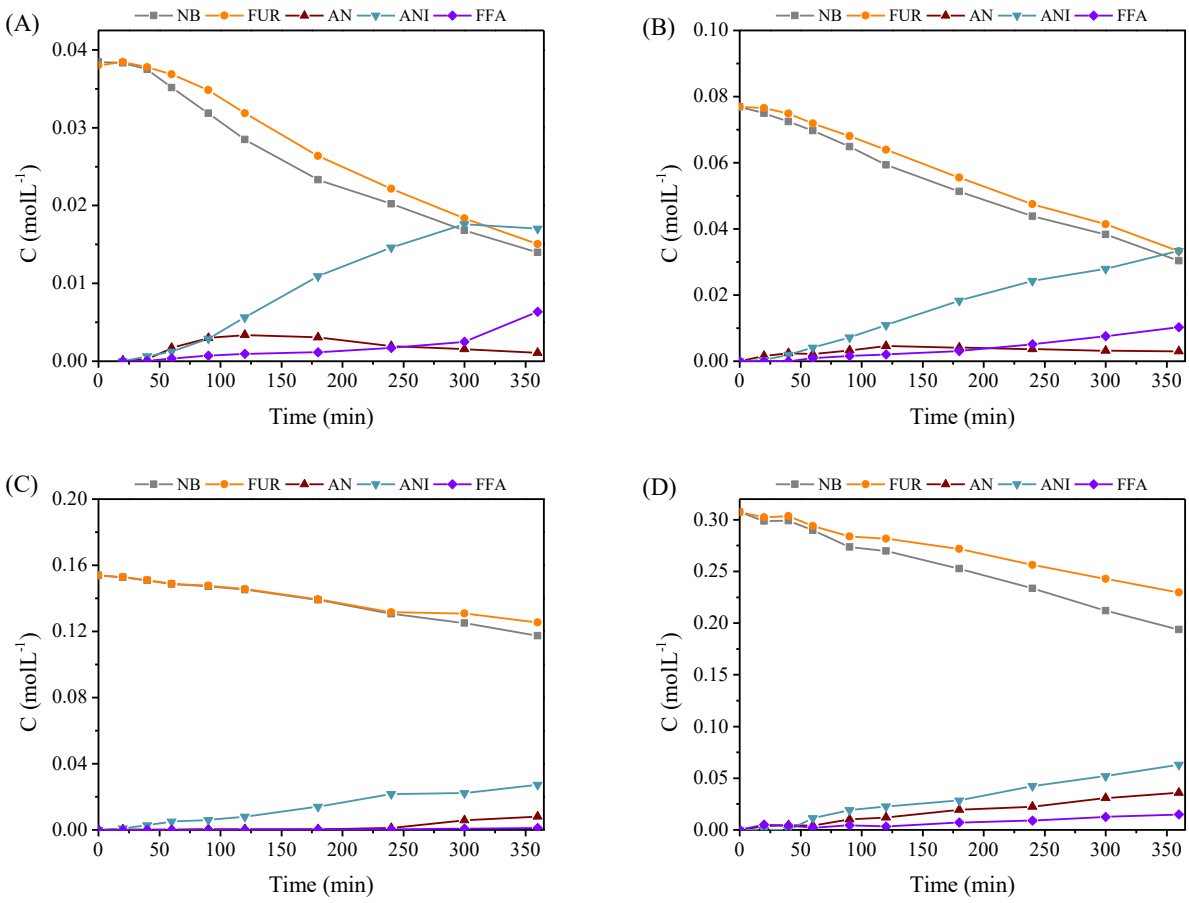

Figure S13. Product distribution for the one-pot synthesis of FFA from NB and FUR. (A) Pt(0.125)/TNT-R, (B) Pt(0.250)/TNT-R, (C) Pt(0.500)/TNT-R and (D) Pt(1.000)/TNT-R. 30°C, 10 bar H_2, 700 rpm, 50 mg of catalyst, 30 mL ethyl acetate, Pt:NB:FUR 1:6000.

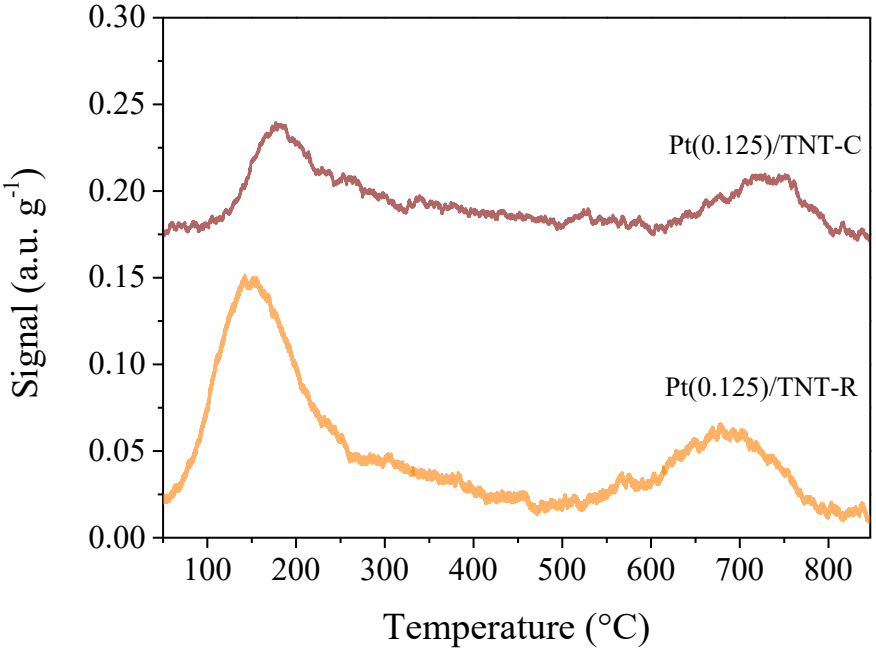

Figure S14. Ammonia TPD for Pt(0.125)/TNT-R and Pt(0.125)/TNT-C.

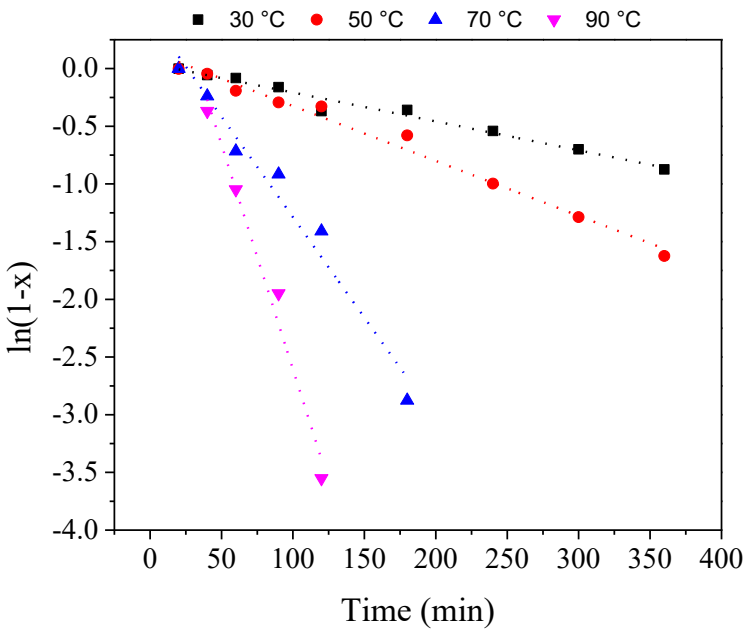

Figure S15. Investigation of the effect of temperature on the reaction between NB and FUR. 10 bar H_2, Pt(0.125)/TNT-R 50 mg, 30 mL of ethanol Pt:NB:FUR 1:6000:6000.

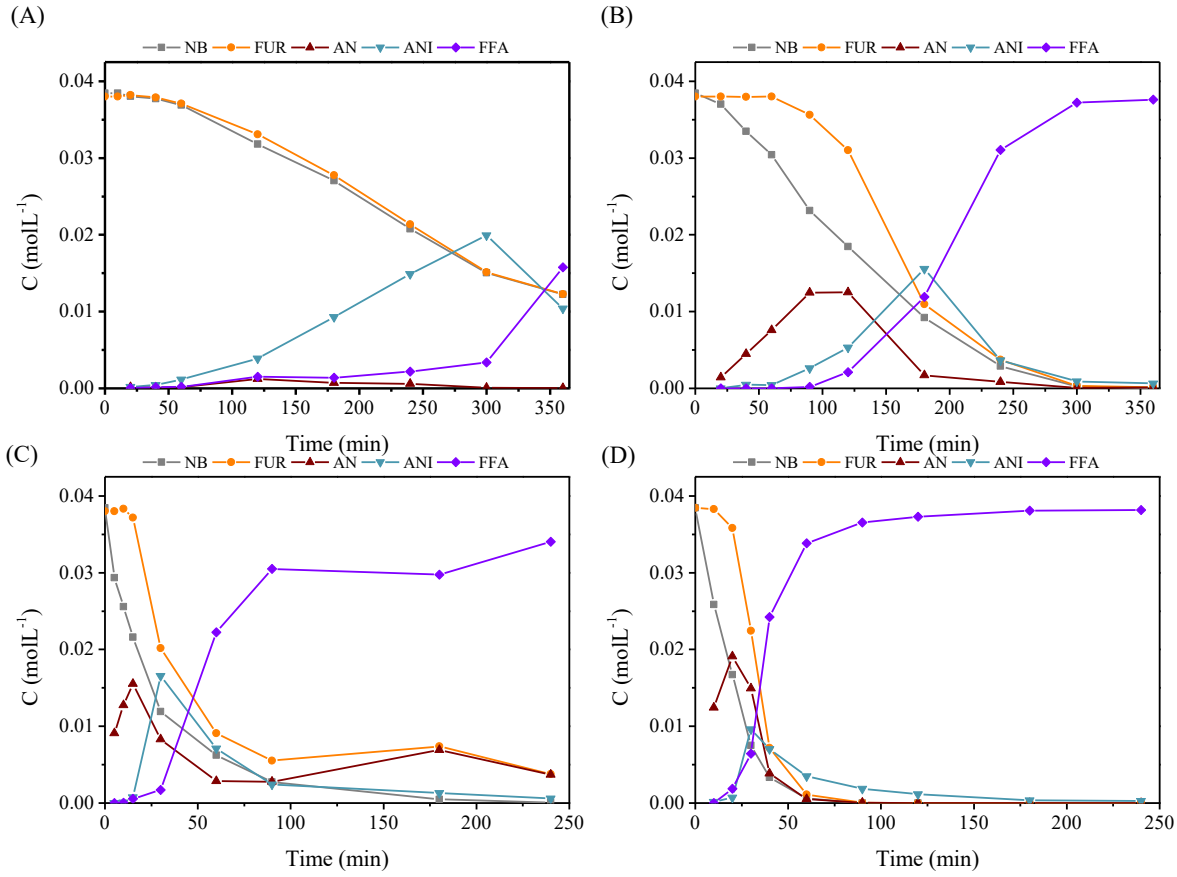

Figure S16. Product distribution of the hydrogenation of FUR and NB to produce FFA, at different temperatures (A) 30°C, (B) 50°C, (C) 70°C and (D) 90°C. 10 bar H_2, Pt(0.125)/TNT-R 50 mg, 30 mL of ethanol Pt:NB:FUR 1:6000:6000.

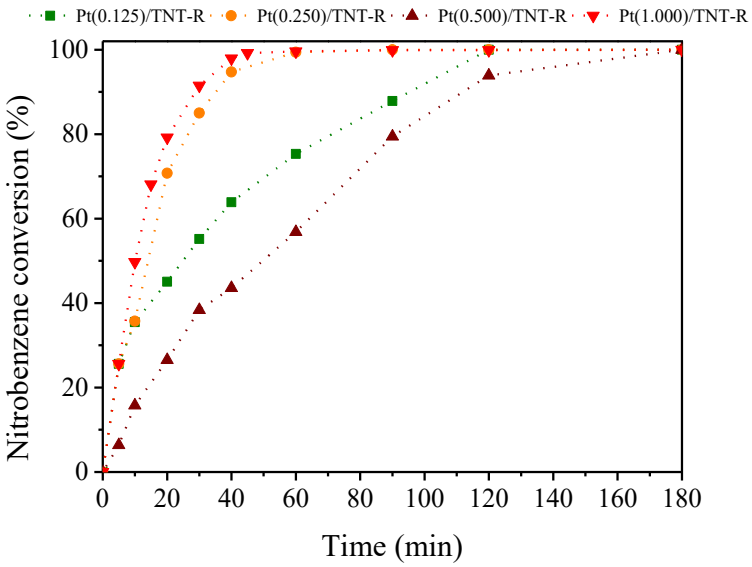

Figure S17. Nitrobenzene conversion for the one-pot synthesis of 3-M. Ethyl acetate 50 mL, 50 mg of catalyst, 100°C, 10 bar H_2, Pt:NB 1:1000, AC:BN 2:1, 700 rpm.

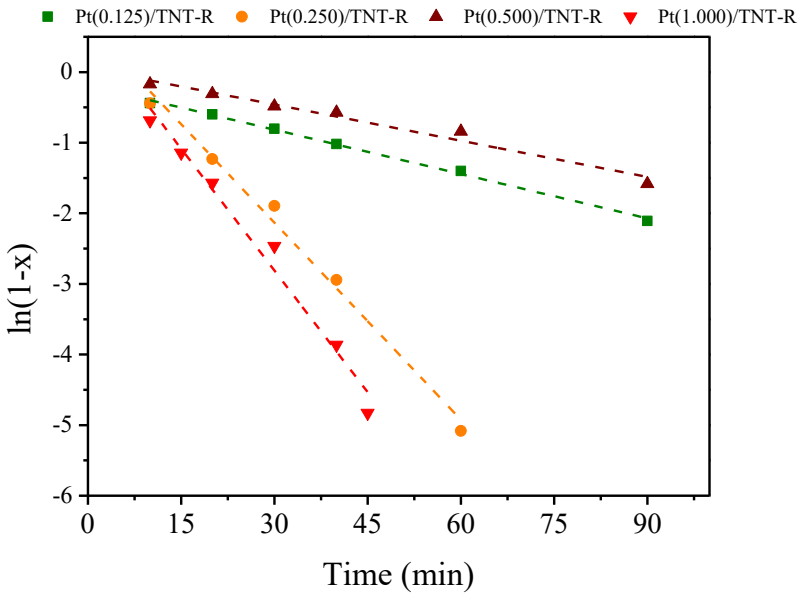

Figure S18. First order adjustment for nitrobenzene conversion for the one-pot synthesis of 3-M. Ethyl acetate 50 mL, 50 mg of catalyst, 100°C, 10 bar H_2, Pt:NB 1:1000, AC:BN 2:1, 700 rpm.

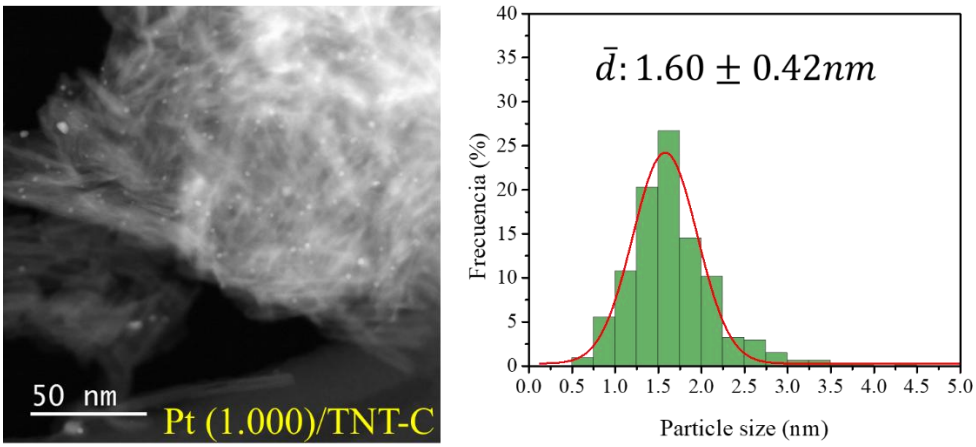

Figure S19. HR-TEM characterization for the Pt(1.000)/TNT-C catalyst and particle size distribution.

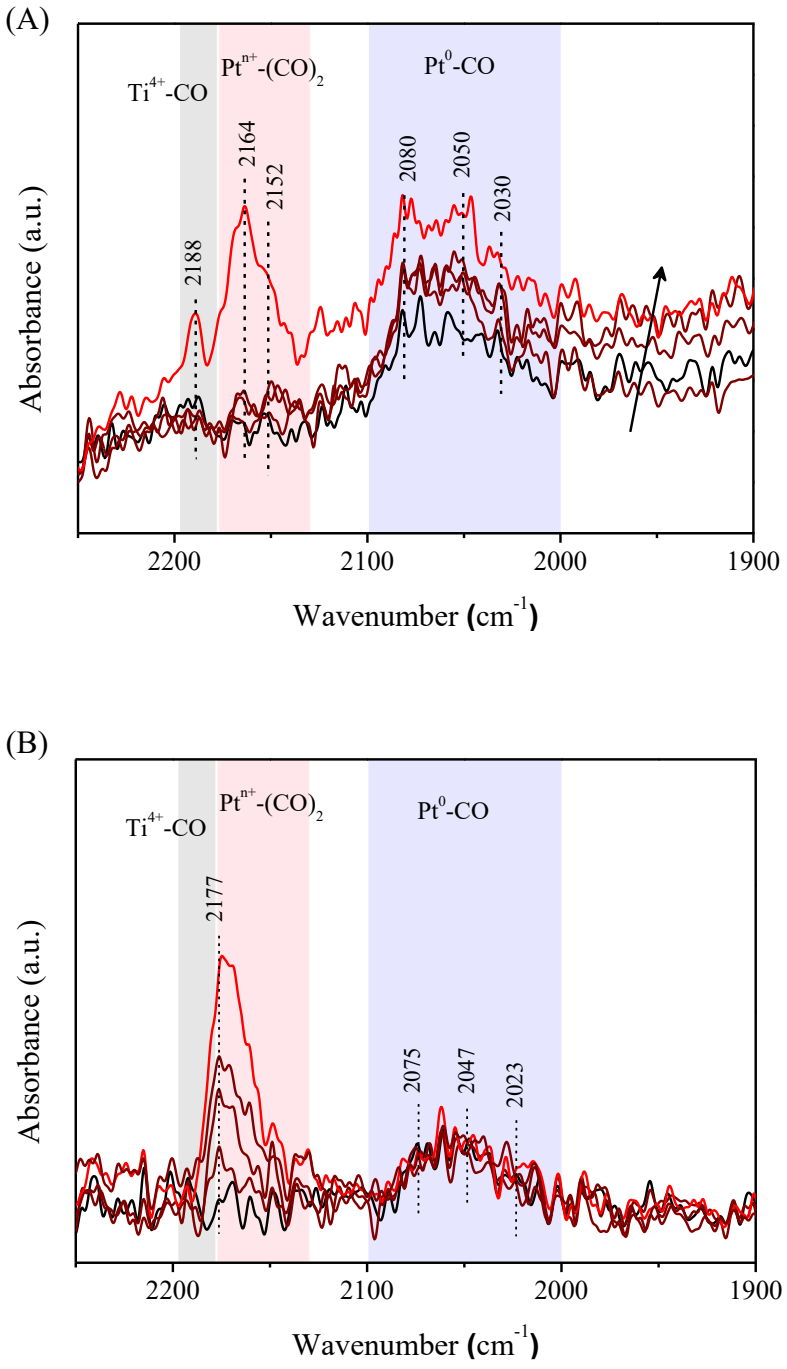

Figure S20. CO low temperature FT-IR (FT-IR CO) for (A) Pt(1.000)/TNT-R, (B) Pt(1.000)/TNT-C.

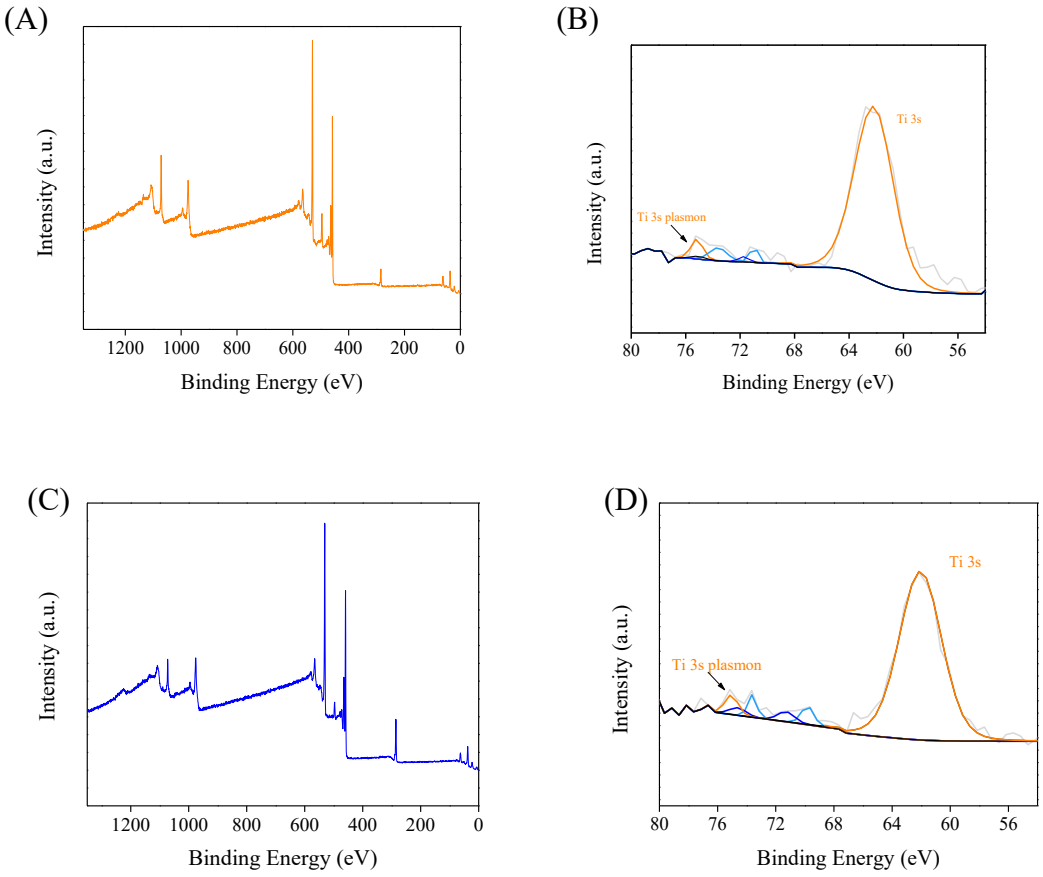

Figure S21. XPS survey for the Pt(1.000) catalyst (A) complete survey for Pt(1.000)/TNT-R and (B) to illustrate the Ti 3s plasmon and the overlapping with the Pt signal. (C) and (D) the equivalent for Pt(1.000)/TNT-C.

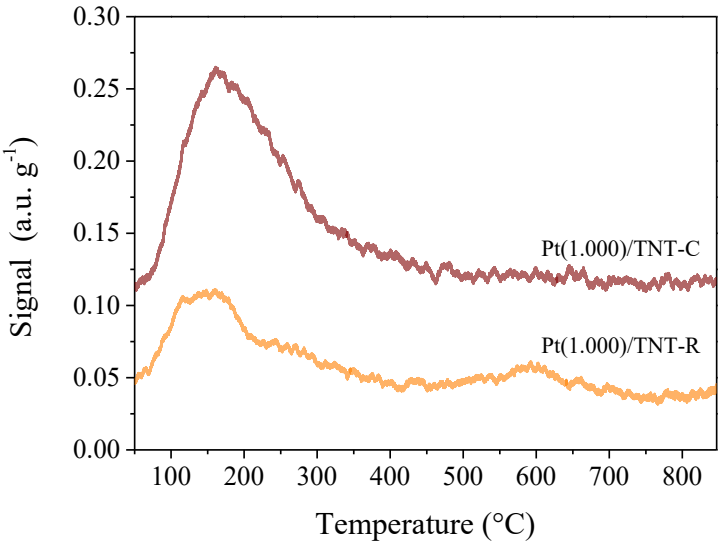

Figure S22. Ammonia TPD for the Pt(1.000) catalyst on TNT-R and TNT-C.

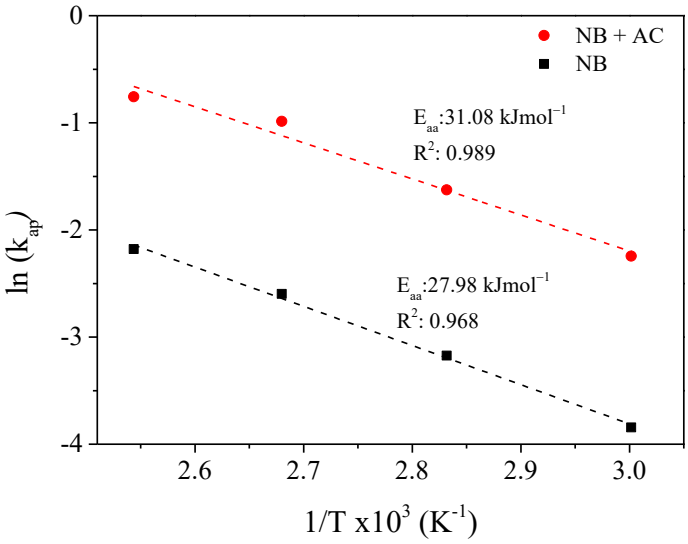

Figure S23. Arrhenius plot for the one-pot synthesis of 3-ML from NB and AC, derived from NB conversion measurements conducted both with and without AC. 10 bar of H_2 pressure, 50 mg of catalyst with a molar ratio Nitrobenzene/Pt = 1000. NB:AC 2:1.

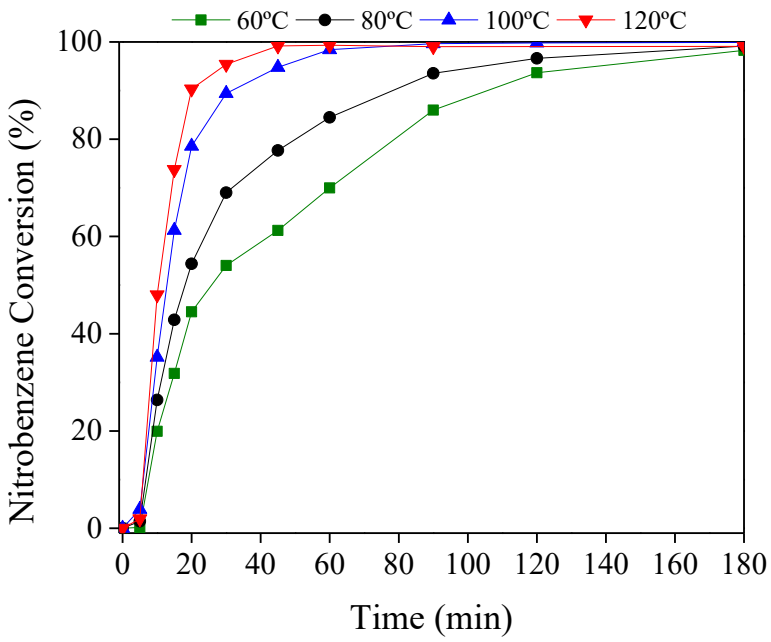

Figure S24. Conversion of nitrobenzene at different temperatures. 10 bar of H_2 pressure, 100°C of temperature, 50 mg of catalyst with a molar ratio Nitrobenzene/Pt = 1000, NB:AC 2:1

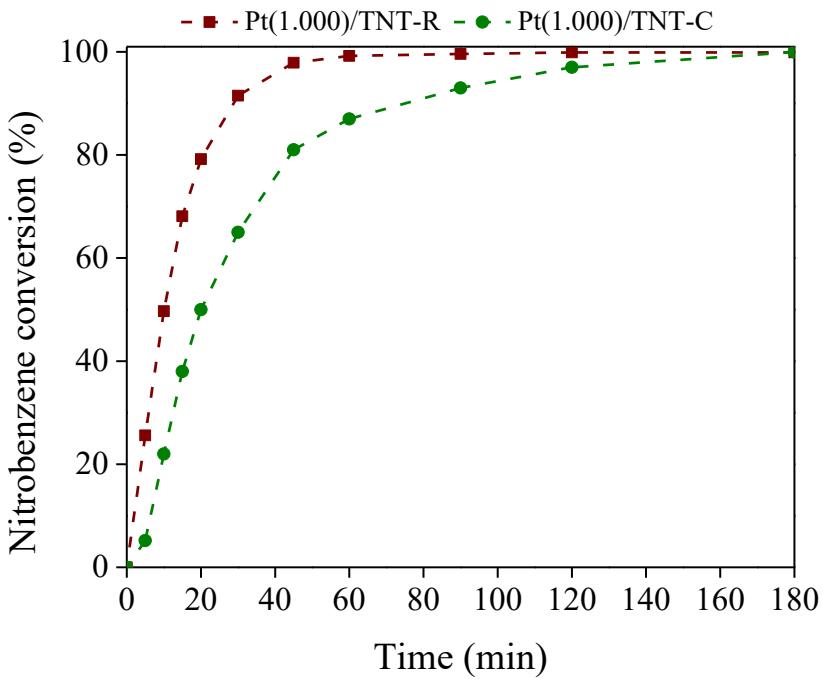

Figure S25. Nitrobenzene conversion for the one-pot synthesis of 3-M. Ethyl acetate 50 mL, 50 mg of catalyst, 100°C, 10 bar H_2, Pt:NB 1:1000, AC:BN 2:1, 700 rpm.

Table S1. Band assignments for pyridine adsorbed on Pt catalyst.

Catalyst	Pyr species[α]	η_{CCN} cm^{-1}		I_{LPy}/I_{HPy} 1606/1591
		η_{19b}	η_{8a}	
Pt(1.000)/TNT-C	LPy	1445	1606	2.14
	HPy	1440	1592	
	BPy	1542	1640	
Pt(1.000)/TNT-R	LPy	1445	1608	0.65
	HPy	1440	1591	

Table S2. Catalytic data for the temperature effect for Pt(1.000)/TNT-R on the 3-ML synthesis from NB and AC.

T (K)	X_{NB} (%)[a]	$S_{3\text{-}ML}$ (%)		S_{AN} (%)		k_{app} min^{-1}	TOF min^{-1}
60	70.0	21.7[b]	38.2[c]	73.5[b]	56.8[c]	0.0214	61
80	84.5	19.3 [b]	44.3[c]	76.9[b]	51.7[c]	0.0309	88
100	99.2	18.6 [b]	50.3[c]	82.1[b]	46.9[c]	0.0837	239
120	99.3	10.8 [b]	32.7[c]	82.5[b]	60.3[c]	0.1131	323

[a]Reaction time: 60 min. [b]Calculated at 40 % conversion. [c]Calculated at 100 % conversion.

8. REFERENCES

[1] F. Poovan, V.G. Chandrashekhar, K. Natte, R.V. Jagadeesh, Synergy between homogeneous and heterogeneous catalysis, Catalysis Science & Technology, 12 (2022) 6623-6649.

[2] X. Hu, A.C.K. Yip, Heterogeneous Catalysis: Enabling a Sustainable Future, Frontiers in Catalysis, Volume 1 - 2021 (2021) 667675.

[3] C. Descorme, P. Gallezot, C. Geantet, C. George, Heterogeneous Catalysis: A Key Tool toward Sustainability, ChemCatChem, 4 (2012) 1897-1906.

[4] B. Qiao, A. Wang, X. Yang, L.F. Allard, Z. Jiang, Y. Cui, J. Liu, J. Li, T. Zhang, Single-atom catalysis of CO oxidation using Pt_1/FeO_x, Nature Chemestry, 3 (2011) 634-641.

[5] Z. Zhang, Y. Chen, L. Zhou, C. Chen, Z. Han, B. Zhang, Q. Wu, L. Yang, L. Du, Y. Bu, P. Wang, X. Wang, H. Yang, Z. Hu, The simplest construction of single-site catalysts by the synergism of micropore trapping and nitrogen anchoring, Nature Communactions, 10 (2019) 1657.

[6] J. Xia, B. Wang, J. Di, Y. Li, S.-Z. Yang, H. Li, S. Guo, Construction of single-atom catalysts for electro-, photo- and photoelectro-catalytic applications: State-of-the-art, opportunities, and challenges, Materials Today, 53 (2022) 217-237.

[7] N. Zhang, C. Ye, H. Yan, L. Li, H. He, D. Wang, Y. Li, Single-atom site catalysts for environmental catalysis, Nano Research, 13 (2020) 3165-3182.

[8] S. Ding, M.J. Hülsey, J. Pérez-Ramírez, N. Yan, Transforming Energy with Single-Atom Catalysts, Joule, 3 (2019) 2897-2929.

[9] X. Li, L. Liu, X. Ren, J. Gao, Y. Huang, B. Liu, Microenvironment modulation of single-atom catalysts and their roles in electrochemical energy conversion, Science Advances, 6 (2020) eabb6833.

[10] Y. Wang, J. Mao, X. Meng, L. Yu, D. Deng, X. Bao, Catalysis with Two-Dimensional Materials Confining Single Atoms: Concept, Design, and Applications, Chemical Reviews, 119 (2019) 1806-1854.

[11] S. Chae, Y. Chen, J. Yang, J. Su, The stability of single-atom catalysts in thermocatalysis, Surface Science and Technology, 2 (2024) 18.

[12] H. Yan, H. Cheng, H. Yi, Y. Lin, T. Yao, C. Wang, J. Li, S. Wei, J. Lu, Single-Atom Pd_1/Graphene Catalyst Achieved by Atomic Layer Deposition: Remarkable Performance in Selective Hydrogenation of 1,3-Butadiene, Journal of the American Chemical Society, 137 (2015) 10484-10487.

[13] L. Wang, E. Guan, J. Zhang, J. Yang, Y. Zhu, Y. Han, M. Yang, C. Cen, G. Fu, B.C. Gates, F.S. Xiao, Single-site catalyst promoters accelerate metal-catalyzed nitroarene hydrogenation, Nature Communications, 9 (2018) 1362.

[14] W. Li, Z. Guo, J. Yang, Y. Li, X. Sun, H. He, S. Li, J. Zhang, Advanced Strategies for Stabilizing Single-Atom Catalysts for Energy Storage and Conversion, Electrochemical Energy Reviews, 5 (2022) 9.

[15] L. Cheng, Q. Wu, H. Sun, Y. Tang, Q. Xiang, Toward Functionality and Deactivation of Metal-Single-Atom in Heterogeneous Photocatalysts, Advanced Materials, 36 (2024) e2406807.

[16] L. Zhang, Y. Ren, W. Liu, A. Wang, T. Zhang, Single-atom catalyst: a rising star for green synthesis of fine chemicals, National Science Review, 5 (2018) 653-672.

[17] T.N. Ye, Z. Xiao, J. Li, Y. Gong, H. Abe, Y. Niwa, M. Sasase, M. Kitano, H. Hosono, Stable single platinum atoms trapped in sub-nanometer cavities in $12CaO{\cdot}7Al_2O_3$ for chemoselective hydrogenation of nitroarenes, Nature Communications, 11 (2020) 1020.

[18] X. Wang, J.A. van Bokhoven, D. Palagin, Ostwald ripening versus single atom trapping: towards understanding platinum particle sintering, Physical Chemistry Chemical Physics, 19 (2017) 30513-30519.

[19] E.D. Goodman, J.A. Schwalbe, M. Cargnello, Mechanistic Understanding and the Rational Design of Sinter-Resistant Heterogeneous Catalysts, ACS Catalysis, 7 (2017) 7156-7173.

[20] E. Leal-Villarroel, D. González-Vera, M.E. Domine, D. Gómez, P. Serp, C.H. Campos, C.C. Torres, Platinum single sites supported on defected hydrogen-titanate nanotubes as selective catalyst for tandem synthesis of 3-methylindoles from nitrocompounds and acetol, Catalysis Today, 460 (2025).

[21] J. Luo, G.I.N. Waterhouse, L. Peng, Q. Chen, Recent progress in high-loading single-atom catalysts and their applications, Industrial Chemistry & Materials, 1 (2023) 486-500.

[22] J. Guo, H. Liu, D. Li, J. Wang, X. Djitcheu, D. He, Q. Zhang, A minireview on the synthesis of single atom catalysts, RSC Advances, 12 (2022) 9373-9394.

[23] R.C. Contreras, B. Guicheret, B.F. Machado, C. Rivera-Cárcamo, M.A. Curiel Alvarez, B. Valdez Salas, M. Ruttert, T. Placke, A. Favre Réguillon, L. Vanoye, C. de Bellefon, R. Philippe, P. Serp, Effect of mesoporous carbon support nature and pretreatments on palladium loading, dispersion and apparent catalytic activity in hydrogenation of myrcene, Journal of Catalysis, 372 (2019) 226-244.

[24] C.R.-C. P. Serp , R. Philippe and B. Guicheret, Procédé de préparation d'atomes métalliques isolés ou d'un mélange d'atomes métalliques isolés et de nanoparticules métalliques sur matériau carboné, 2019.

[25] D.M. Fernandes, M. Rocha, C. Rivera-Carcamo, P. Serp, C. Freire, Ru single atoms and nanoparticles on carbon nanotubes as multifunctional catalysts, Dalton Transactions, 49 (2020) 10250-10260.

[26] F. Meng, Z. Tian, W. Tian, H. Zhang, Advances in carbon nitride supported single-atom photocatalysts for hydrogen evolution, Current Opinion in Chemical Engineering, 41 (2023).

[27] Y. Li, Y. Feng, D. Zheng, X. Zhao, Y. Zhou, X. Fu, X. Chen, High-performance screening of carbon-nitride single-atom catalysts for oxygen electrode reaction in rechargeable metal–air batteries, Chemical Engineering Journal, 476 (2023).

[28] Y. Zhang, J. Yang, R. Ge, J. Zhang, J.M. Cairney, Y. Li, M. Zhu, S. Li, W. Li, The effect of coordination environment on the activity and selectivity of single-atom catalysts, Coordination Chemistry Reviews, 461 (2022).

[29] S. Kumar, X.T. Cao, Natural bio-sourced polymers: Emerging precursors for the synthesis of single atom catalysts, Coordination Chemistry Reviews, 499 (2024).

[30] Y.-Y. Yu, X.-Q. Gong, CO Oxidation at Rutile TiO_2 (110): Role of Oxygen Vacancies and Titanium Interstitials, ACS Catalysis, 5 (2015) 2042-2050.

[31] C. Coperet, A. Comas-Vives, M.P. Conley, D.P. Estes, A. Fedorov, V. Mougel, H. Nagae, F. Nunez-Zarur, P.A. Zhizhko, Surface Organometallic and Coordination Chemistry toward Single-Site Heterogeneous Catalysts: Strategies, Methods, Structures, and Activities, Chemical Reviews, 116 (2016) 323-421.

[32] C. Rivera-Cárcamo, C. Scarfiello, A.B. García, Y. Tison, H. Martinez, W. Baaziz, O. Ersen, C. Le Berre, P. Serp, Stabilization of Metal Single Atoms on Carbon and TiO_2 Supports for CO_2 Hydrogenation: The Importance of Regulating Charge Transfer, Advanced Materials Interfaces, 8 (2021) 2001777.

[33] S. Gutiérrez-Tarriño, S. Rojas-Buzo, C.W. Lopes, G. Agostini, J.J. Calvino, A. Corma, P. Oña-Burgos, Cobalt nanoclusters coated with N-doped carbon for chemoselective nitroarene hydrogenation and tandem reactions in water, Green Chemistry, 23 (2021) 4490-4501.

[34] R. Huang, C. Cao, J. Liu, L. Zheng, Q. Zhang, L. Gu, L. Jiang, W. Song, Integration of Metal Single Atoms on Hierarchical Porous Nitrogen-Doped Carbon for Highly Efficient Hydrogenation of Large-Sized Molecules in the Pharmaceutical Industry, ACS Applied Materials & Interfaces, 12 (2020) 17651-17658.

[35] M.B. Gawande, P. Fornasiero, R. Zbořil, Carbon-Based Single-Atom Catalysts for Advanced Applications, ACS Catalysis, 10 (2020) 2231-2259.

[36] E. Leal-Villarroel, D. González-Vera, M.E. Domine, D. Gómez, P. Serp, C.H. Campos, C.C. Torres, Platinum single sites supported on defected hydrogen-titanate nanotubes as selective catalyst for tandem synthesis of 3-methylindoles from nitrocompounds and acetol, Catalysis Today, 460 (2025) 115468.

[37] M. Guo, Q. Meng, M.L. Gao, L. Zheng, Q. Li, L. Jiao, H.L. Jiang, Single-Atom Pt Loaded on MOF-Derived Porous TiO_2 with Maximized Pt Atom Utilization for Selective

Hydrogenation of Halonitro-benzene, Angewandte Chemie International Edition, (2024) e202418964.

[38] Z. Wu, I. Hwang, G. Cha, S. Qin, O. Tomanec, Z. Badura, S. Kment, R. Zboril, P. Schmuki, Optimized Pt Single Atom Harvesting on TiO_2 Nanotubes-Towards a Most Efficient Photocatalyst, Small, 18 (2022) e2104892.

[39] C. Wang, S. Mao, Z. Wang, Y. Chen, W. Yuan, Y. Ou, H. Zhang, Y. Gong, Y. Wang, B. Mei, Z. Jiang, Y. Wang, Insight into Single-Atom-Induced Unconventional Size Dependence over CeO_2-Supported Pt Catalysts, Chem, 6 (2020) 752-765.

[40] B.B. Sarma, J. Kim, J. Amsler, G. Agostini, C. Weidenthaler, N. Pfander, R. Arenal, P. Concepcion, P. Plessow, F. Studt, G. Prieto, One-Pot Cooperation of Single-Atom Rh and Ru Solid Catalysts for a Selective Tandem Olefin Isomerization-Hydrosilylation Process, Angewandte Chemie 59 (2020) 5806-5815.

[41] C. Liu, B. Qiao, Stranding isolated Pt single atoms on the CeO_x “nanoislands” over the SiO_2 “microsea”, Joule, 6 (2022) 2688-2691.

[42] M.T. Noman, M.A. Ashraf, A. Ali, Synthesis and applications of nano-TiO_2: a review, Environmental Science and Pollution Research, 26 (2019) 3262-3291.

[43] L. DeRita, J. Resasco, S. Dai, A. Boubnov, H.V. Thang, A.S. Hoffman, I. Ro, G.W. Graham, S.R. Bare, G. Pacchioni, X. Pan, P. Christopher, Structural evolution of atomically dispersed Pt catalysts dictates reactivity, Nature Materials, 18 (2019) 746-751.

[44] J. Wan, W. Chen, C. Jia, L. Zheng, J. Dong, X. Zheng, Y. Wang, W. Yan, C. Chen, Q. Peng, D. Wang, Y. Li, Defect Effects on TiO_2 Nanosheets: Stabilizing Single Atomic Site Au and Promoting Catalytic Properties, Advanced Materials, 30 (2018) 1705369.

[45] T. Kropp, Z. Lu, Z. Li, Y.-H.C. Chin, M. Mavrikakis, Anionic Single-Atom Catalysts for CO Oxidation: Support-Independent Activity at Low Temperatures, ACS Catalysis, 9 (2019) 1595-1604.

[46] X. Pan, M.Q. Yang, X. Fu, N. Zhang, Y.J. Xu, Defective TiO_2 with oxygen vacancies: synthesis, properties and photocatalytic applications, Nanoscale, 5 (2013) 3601-3614.

[47] F.M. Pinto, V.Y. Suzuki, R.C. Silva, F.A. La Porta, Oxygen Defects and Surface Chemistry of Reducible Oxides, Frontiers in Materials, 6 (2019) 260.

[48] G. Han, J.Y. Kim, K.-J. Kim, H. Lee, Y.-M. Kim, Controlling surface oxygen vacancies in Fe-doped TiO_2 anatase nanoparticles for superior photocatalytic activities, Applied Surface Science, 507 (2020).

[49] T.L. Thompson, J.T. Yates, TiO_2-based Photocatalysis: Surface Defects, Oxygen and Charge Transfer, Topics in Catalysis, 35 (2005) 197-210.

[50] H. Iddir, V. Skavysh, S. Öğüt, N.D. Browning, M.M. Disko, Preferential growth of Pt on rutile TiO_2, Physical Review B, 73 (2006) 041403.

[51] V. Çelik, H. Ünal, E. Mete, Ş. Ellialtıoğlu, Theoretical analysis of small Pt particles on rutile TiO_2 (110) surfaces, Physical Review B, 82 (2010) 205113.

[52] T.Y. Chang, Y. Tanaka, R. Ishikawa, K. Toyoura, K. Matsunaga, Y. Ikuhara, N. Shibata, Direct imaging of Pt single atoms adsorbed on TiO_2 (110) surfaces, Nano Letters, 14 (2014) 134-138.

[53] S. Fischer, A.W. Munz, K.-D. Schierbaum, W. Göpel, The geometric structure of intrinsic defects at TiO_2 (110) surfaces: an STM study, Surface Science, 337 (1995) 17-30.

[54] U. Diebold, J. Lehman, T. Mahmoud, M. Kuhn, G. Leonardelli, W. Hebenstreit, M. Schmid, P. Varga, Intrinsic defects on a TiO_2 (110) (1×1) surface and their reaction with oxygen: a scanning tunneling microscopy study, Surface Science, 411 (1998) 137-153.

[55] S. Wendt, R. Schaub, J. Matthiesen, E.K. Vestergaard, E. Wahlström, M.D. Rasmussen, P. Thostrup, L.M. Molina, E. Lægsgaard, I. Stensgaard, B. Hammer, F. Besenbacher, Oxygen vacancies on TiO_2 (110) and their interaction with H_2O and O_2: A combined high-resolution STM and DFT study, Surface Science, 598 (2005) 226-245.

[56] H. Shang, M. Li, H. Li, S. Huang, C. Mao, Z. Ai, L. Zhang, Oxygen Vacancies Promoted the Selective Photocatalytic Removal of NO with Blue TiO_2 via Simultaneous Molecular Oxygen Activation and Photogenerated Hole Annihilation, Environmental Science & Technology, 53 (2019) 6444-6453.

[57] X. Jiang, Y. Zhang, J. Jiang, Y. Rong, Y. Wang, Y. Wu, C. Pan, Characterization of Oxygen Vacancy Associates within Hydrogenated TiO_2: A Positron Annihilation Study, The Journal of Physical Chemistry C, 116 (2012) 22619-22624.

[58] B. Shi, X. Lu, Single-atom catalysts meet electrospinning: a blissful marriage for energy catalysis, Chemical Science, 16 (2025) 17568-17594.

[59] A.R. Supandi, N. Nunotani, N. Imanaka, Particle size effect of ZrO_2 supports on catalytic liquid-phase oxidation of phenol over Pt/CeO_2-ZrO_2-Bi_2O_3/ZrO_2 catalysts, Journal of Asian Ceramic Societies, 8 (2020) 745-752.

[60] X. Chen, L. Liu, P.Y. Yu, S.S. Mao, Increasing Solar Absorption for Photocatalysis with Black Hydrogenated Titanium Dioxide Nanocrystals, Science, 331 (2011) 746-750.

[61] L. Andronic, A. Enesca, Black TiO_2 Synthesis by Chemical Reduction Methods for Photocatalysis Applications, Frontiers in Chemistry, 8 (2020) 565489.

[62] H. Tan, Z. Zhao, M. Niu, C. Mao, D. Cao, D. Cheng, P. Feng, Z. Sun, A facile and versatile method for preparation of colored TiO_2 with enhanced solar-driven photocatalytic activity, Nanoscale, 6 (2014) 10216-10223.

[63] J. Tian, Y. Leng, Z. Zhao, Y. Xia, Y. Sang, P. Hao, J. Zhan, M. Li, H. Liu, Carbon quantum dots/hydrogenated TiO_2 nanobelt heterostructures and their broad spectrum photocatalytic properties under UV, visible, and near-infrared irradiation, Nano Energy, 11 (2015) 419-427.

[64] F. Calle-Vallejo, M.T. Koper, A.S. Bandarenka, Tailoring the catalytic activity of electrodes with monolayer amounts of foreign metals, Chemical Society Reviews, 42 (2013) 5210-5230.

[65] J. Tymoczko, F. Calle-Vallejo, W. Schuhmann, A.S. Bandarenka, Making the hydrogen evolution reaction in polymer electrolyte membrane electrolysers even faster, Nature Communications, 7 (2016) 10990.

[66] L. Aldous, A. Khan, M.M. Hossain, C. Zhao, CHAPTER 8. Electrocatalysis in Ionic Liquids, Catalysis in Ionic Liquids2014, pp. 433-473.

[67] E. Vorobyeva, E. Fako, Z. Chen, S.M. Collins, D. Johnstone, P.A. Midgley, R. Hauert, O.V. Safonova, G. Vile, N. Lopez, S. Mitchell, J. Perez-Ramirez, Atom-by-Atom Resolution of Structure-Function Relations over Low-Nuclearity Metal Catalysts, Angewandte Chemie International Edition, 58 (2019) 8724-8729.

[68] P. Serna, Cooperativity between atoms in supported “Single-Atom Catalysts” and metal clusters, Chemical Engineering Journal, 496 (2024).

[69] P. Serp, Cooperativity in supported metal single atom catalysis, Nanoscale, 13 (2021) 5985-6004.

[70] C. Rivera-Cárcamo, I.C. Gerber, I. del Rosal, B. Guicheret, R. Castro Contreras, L. Vanoye, A. Favre-Réguillon, B.F. Machado, J. Audevard, C. de Bellefon, R. Philippe, P. Serp, Control of the single atom/nanoparticle ratio in Pd/C catalysts to optimize the cooperative hydrogenation of alkenes, Catalysis Science & Technology, 11 (2021) 984-999.

[71] S. Ji, Y. Chen, X. Wang, Z. Zhang, D. Wang, Y. Li, Chemical Synthesis of Single Atomic Site Catalysts, Chemical Reviews, 120 (2020) 11900-11955.

[72] C.-C. Hou, H.-F. Wang, C. Li, Q. Xu, From metal–organic frameworks to single/dual-atom and cluster metal catalysts for energy applications, Energy & Environmental Science, 13 (2020) 1658-1693.

[73] S.E. Sivan, K.H. Kang, S.J. Han, O. Francis Ngome Okello, S.-Y. Choi, V. Sudheeshkumar, R.W.J. Scott, H.-J. Chae, S. Park, U.H. Lee, Facile MOF-derived one-pot synthetic approach toward Ru single atoms, nanoclusters, and nanoparticles dispersed on CeO_2 supports for enhanced ammonia synthesis, Journal of Catalysis, 408 (2022) 316-328.

[74] Y. Zhang, M. Zhang, Y. Zhou, L. Yang, B. Lin, J. Ni, L. Zheng, X. Wang, C.-t. Au, L. Jiang, Insight into the critical role of strong interaction between Ru and Co in RuCo single-atom alloy structure for significant enhancement of ammonia synthesis performance, Journal of Catalysis, 410 (2022) 256-265.

[75] J. Li, Z. Yang, Y. Li, G. Zhang, Advances in single-atom catalysts: Design, synthesis and environmental applications, Journal of Hazardous Materials, 429 (2022) 128285.

[76] H.U. Blaser, C. Malan, B. Pugin, F. Spindler, H. Steiner, M. Studer, Selective Hydrogenation for Fine Chemicals: Recent Trends and New Developments, Advanced Synthesis & Catalysis, 345 (2003) 103-151.

[77] W. Callewaert, B.V. Pessanha, J. Lauwaert, D. Fernandes del Pozo, I. Nopens, P. Baldwin, M. McNamara, J.W. Thybaut, Advancing Nitrobenzene Hydrogenation Process Understanding: A Multiscale Modeling Approach using Industrial Pharmaceutical Production Data, Industrial & Engineering Chemistry Research, 63 (2024) 14029-14042.

[78] B. Lakshminarayana, M. Selvaraj, G. Satyanarayana, C. Subrahmanyam, Switching of support materials for the hydrogenation of nitroarenes: A review, Catalysis Reviews, (2022) 1-84.

[79] A.J. Burke, C.S. Marques, N.J. Turner, G.J. Hermann, Active Pharmaceutical Ingredients in Synthesis: Catalytic Processes in Research and Development, Wiley2018.

[80] Y. Xu, J. Zhang, P. Wang, Y. Fan, Y. Jiang, X. Duan, Y. Li, J. Zhang, Highly efficient and stable Ni-based catalyst for selective conversion of biomass-derived aldehydes and ketones to primary amines, Chemical Engineering Journal, 480 (2024).

[81] E.A. Gelder, S.D. Jackson, C.M. Lok, The hydrogenation of nitrobenzene to aniline: a new mechanism, Chemical Communications, (2005) 522-524.

[82] Z.N. Jaf, M. Altarawneh, H.A. Miran, M.H. Almatarneh, Z.T. Jiang, B.Z. Dlugogorski, Catalytic Hydrogenation of p-Chloronitrobenzene to p-Chloroaniline Mediated by gamma-Mo_2N, ACS Omega, 3 (2018) 14380-14391.

[83] Y. Zhou, Y. Zheng, C. Lu, B. Maity, Y. Chen, T. Ueno, Z. Liu, D. Lu, Apo-ferritin-Caged Pt Nanoparticles for Selective Hydrogenation of p-Chloronitrobenzene, ACS Applied Nano Materials, 6 (2023) 5835-5843.

[84] T. Newhouse, P.S. Baran, R.W. Hoffmann, The economies of synthesis, Chemical Society Reviews, 38 (2009) 3010-3021.

[85] Y. Hayashi, Pot economy and one-pot synthesis, Chemical Science, 7 (2016) 866-880.

[86] M.H. Brijaldo, H.A. Rojas, Y. Xing, F.B. Passos, J.J. Martínez, Pt/Nb_2O_5-Al_2O_3 Catalysts for the Hydrogenation and Reductive Amination of Furfural, Catalysts, 14 (2024) 493.

[87] C. Len, R. Luque, Continuous flow transformations of glycerol to valuable products: an overview, Sustainable Chemical Processes, 2 (2014) 1.

[88] C.H. Zhou, J.N. Beltramini, Y.X. Fan, G.Q. Lu, Chemoselective catalytic conversion of glycerol as a biorenewable source to valuable commodity chemicals, Chemical Society Reviews, 37 (2008) 527-549.

[89] K.E. Salnikova, V.G. Matveeva, Y.V. Larichev, A.V. Bykov, G.N. Demidenko, I.P. Shkileva, M.G. Sulman, The liquid phase catalytic hydrogenation of furfural to furfuryl alcohol, Catalysis Today, 329 (2019) 142-148.

[90] F. Brégier, J. Godard, J. Thiais, S. Bouramtane, A. Moulin, Y. Champavier, A. Mailleau, V. Chaleix, V. Sol, Regioselective reduction of 5-aryl-10,15,20-tris(pyridyl) porphyrin to 5-aryl-10,15,20-tris(pyridyl)dihydroporphyrin (chlorin), Journal of Porphyrins and Phthalocyanines, 23 (2019) 1380-1397.

[91] W.E. Noland, H.V. Kumar, G.C. Flick, C.L. Aspros, J.H. Yoon, A.C. Wilt, N. Dehkordi, S. Thao, A.K. Schneerer, S. Gao, K.J. Tritch, Hydrated ferric sulfate-catalyzed reactions of indole with aldehydes, ketones, cyclic ketones, and chromanones: Synthesis of bisindoles and trisindoles, Tetrahedron, 73 (2017) 3913-3922.

[92] A. Rahman, P. N, N.B. N, H.M. Kumaraswamy, A.N. Rajeshwara, N.D. Satyanarayan, Synthesis and anticancer screening of some novel Pd-catalysed 3-methyl indole based analogues on Mia PaCa-2 cell line, Journal of Molecular Structure, 1264 (2022).

[93] V. Meenakumari, J. Mangaiyarkkarasi, R. Premkumar, R.M. Asath, A.M.F. Benial, N. Thenmozhi, Spectroscopic characterization, quantum chemical and molecular docking investigations on methyl indole-3-carboxylate: A potent cervical cancer drug, Journal of Molecular Structure, 1305 (2024).

[94] D. Li, J. Zhang, Y. Liu, H. Yuan, Y. Chen, Boron doped magnetic catalysts for selective transfer hydrogenation of furfural into furfuryl alcohol, Chemical Engineering Science, 229 (2021).

[95] Y. Fu, P. Sun, G. Li, R. He, L. Shi, N. Xing, Recent advances in the synthetic method and mechanism for the important N-heterocyclic compound of 3-methylindole, Journal of Heterocyclic Chemistry, 59 (2022) 1135-1143.

[96] F. Hochberger-Roa, P.H. García-Ríos, J.G. López-Cortés, M.C. Ortega-Alfaro, J.-C. Daran, M. Gouygou, M. Urrutigoïty, Interrupted Intramolecular Hydroaminomethylation of N-Protected-2-vinyl Anilines: Novel Access to 3-Substitued Indoles or Indoline-2-ols, Molecules, 2022, pp. 1074.

[97] T. Werpy, G. Petersen, Top Value Added Chemicals from Biomass: Volume I -- Results of Screening for Potential Candidates from Sugars and Synthesis Gas, United States, 2004.

[98] H. Qi, J. Yang, F. Liu, L. Zhang, J. Yang, X. Liu, L. Li, Y. Su, Y. Liu, R. Hao, A. Wang, T. Zhang, Highly selective and robust single-atom catalyst Ru_1/NC for reductive amination of aldehydes/ketones, Nature Communications, 12 (2021) 3295.

[99] D.S.S. Jorqueira, L.F. de Lima, S.F. Moya, L. Vilcocq, D. Richard, M.A. Fraga, R.S. Suppino, Critical review of furfural and furfuryl alcohol production: Past, present, and future on heterogeneous catalysis, Applied Catalysis A: General, 665 (2023).

[100] Y. Yang, L. Zhou, X. Wang, L. Zhang, H. Cheng, F. Zhao, Catalytic reductive amination of furfural to furfurylamine on robust ultra-small Ni nanoparticles, Nano Research, 16 (2022) 3719-3729.

[101] K. Han, S. Song, Y. You, X. Fu, X. Li, Synergistic Effect of Electron-Deficient Ru^0 and Lewis Acid Sites on Ru/TiO_2 for Efficient Reductive Amination of Furfural via Promoting Schiff Base Ammonolysis, ACS Catalysis, 15 (2025) 14575-14587.

[102] K. Ravi, J.H. Advani, B.D. Bankar, A.S. Singh, A.V. Biradar, Sustainable route for the synthesis of flower-like Ni@N-doped carbon nanosheets from bagasse and its catalytic activity towards reductive amination of nitroarenes with bio-derived aldehydes, New Journal of Chemistry, 44 (2020) 18714-18723.

[103] G. Singh, J. Kaishyop, G. Singh, M.J. Gazi, A. Bag, C. Samanta, A. Bordoloi, One-Pot direct reductive amination of furfural over Pd@CNTs, Molecular Catalysis, 535 (2023).

[104] P. Subha, Q. Luo, H. Li, P. Sudarsanam, One-pot, in situ reductive catalytic approach for biomass furfural-based secondary amines under ambient conditions, Green Chemistry, 27 (2025) 11794-11808.

[105] A.A. Fernández-Andrade, J.A. Vergara, D. Gómez, D. González-Vera, C.H. Campos, J.M. Rodríguez-Díaz, L.E. Arteaga-Pérez, Exploring the bifunctional role of Pd/ZrO_2-TiO_2 in the production of secondary amines via reductive amination of furfural, Applied Catalysis A: General, 705 (2025).

[106] Y. Chen, C. Xu, C. Liu, X. Li, J. Liu, Y. Cao, J. Yang, Synthesis of 3-Methylindole from Glycerol Cyclization with Aniline over $CuCr/Al_2O_3$ Catalysts Modified by Alkali Earth Oxides, Heteroatom Chemistry, 24 (2013) 263-270.

[107] S. Ayari, M.F. Saglam, E. Şenkuytu, P.B. Erçin, Y. Zorlu, I.F. Sengul, B. Jamoussi, D. Atilla, 3-Methylindole-substituted zinc phthalocyanines for photodynamic cancer therapy, Journal of Porphyrins and Phthalocyanines, 23 (2019) 1371-1379.

[108] W.E. Noland, H.V. Kumar, G.C. Flick, C.L. Aspros, J.H. Yoon, A.C. Wilt, N. Dehkordi, S. Thao, A.K. Schneerer, S. Gao, K.J. Tritch, Hydrated ferric sulfate-catalyzed reactions of indole with aldehydes, ketones, cyclic ketones, and chromanones: Synthesis of bisindoles and trisindoles, Tetrahedron, 73 (2017) 3913-3922.

[109] Y. Fu, P. Sun, G. Li, R. He, L. Shi, N. Xing, Recent advances in the synthetic method and mechanism for the important N-heterocyclic compound of 3-methylindole, Journal of Heterocyclic Chemistry, 59 (2022) 1135-1143.

[110] E. Zgarbová, R. Vrzal, Skatole: A thin red line between its benefits and toxicity, Biochimie, 208 (2023) 1-12.

[111] F. Hochberger-Roa, P.H. García-Ríos, J.G. López-Cortés, M.C. Ortega-Alfaro, J.-C. Daran, M. Gouygou, M. Urrutigoïty, Interrupted Intramolecular Hydroaminomethylation of N-Protected-2-vinyl Anilines: Novel Access to 3-Substitued Indoles or Indoline-2-ols, Molecules, 27 (2022) 1074.

[112] A. Rahman, P. N, N.B. N, H.M. Kumaraswamy, A.N. Rajeshwara, N.D. Satyanarayan, Synthesis and anticancer screening of some novel Pd-catalysed 3-methyl

indole based analogues on Mia PaCa-2 cell line, Journal of Molecular Structure, 1264 (2022) 133211.

[113] V. Meenakumari, J. Mangaiyarkkarasi, R. Premkumar, R.M. Asath, A.M.F. Benial, N. Thenmozhi, Spectroscopic characterization, quantum chemical and molecular docking investigations on methyl indole-3-carboxylate: A potent cervical cancer drug, Journal of Molecular Structure, 1305 (2024) 137711.

[114] K. Ke, F. Wu, L. Ren, Y. Jiao, N. Xing, L. Shi, An efficient catalyst of Cu/MIL-101 modified with CeO_2 for the conversion of biomass-derived glycerol with aniline to 3-methylindole, Catalysis Communications, 136 (2020) 105896.

[115] Y. Qu, Y. Gao, S. Lin, L. Shi, Efficient synthesis of 3-methylindole using biomass-derived glycerol and aniline over ZnO and CeO_2 modified Ag/SBA-15 catalysts, Molecular Catalysis, 493 (2020) 111038.

[116] J. Su, X. Du, K. Ke, Y. Qu, N. Xing, L. Shi, Efficient one-pot synthesis of 3-methylindole from biomass-derived glycerol with aniline over Cu/SiO_2 modified with ZnO and Fe_2O_3 and deep insight into the mechanism, Reaction Kinetics, Mechanisms and Catalysis, 128 (2019) 361-377.

[117] W. Sun, D.-Y. Liu, H.-Y. Zhu, L. Shi, Q. Sun, A new efficient approach to 3-methylindole: Vapor-phase synthesis from aniline and glycerol over Cu-based catalyst, Catalysis Communications, 12 (2010) 147-150.

[118] B.A.O. Zhuo-Ran, C.U.I. Yan-Xi, S.U.N. Peng, S.U.N. Qi, S.H.I. Lei, Vapor-Phase Synthesis of 3-Methylindole from Glycerol and Aniline

over Cu/SiO_2-Al_2O_3 Catalyst Modified by Co or Ni, Acta Physico-Chimica Sinica, 29 (2013) 2444-2450.

[119] C.A. Simoneau, A.M. Strohl, B. Ganem, One-pot synthesis of polysubstituted indoles from aliphatic nitro-compounds under mild conditions, Tetrahedron Letters, 48 (2007) 1809-1811.

[120] C.A. Simoneau, B. Ganem, Multiple component Fischer indole reactions, Tetrahedron, 61 (2005) 11374-11379.

[121] M.H. Mohamad, R. Awang, W.M.Z.W. Yunus, A Review of Acetol: Application and Production, American Journal of Applied Sciences, 8 (2011) 1135-1139.

[122] M.E. Domine, M.C. Hernández-Soto, M.T. Navarro, Y. Pérez, Pt and Pd nanoparticles supported on structured materials as catalysts for the selective reductive amination of carbonyl compounds, Catalysis Today, 172 (2011) 13-20.

[123] C.C. Torres, V.A. Jiménez, C.H. Campos, J.B. Alderete, R. Dinamarca, T.M. Bustamente, B. Pawelec, Gold catalysts supported on TiO_2-nanotubes for the selective hydrogenation of *p*-substituted nitrobenzenes, Molecular Catalysis, 447 (2018) 21-27.

[124] D. Patra, R. Garg, A. Singh, U.K. Gautam, R. Ganesan, B. Gopalan, In situ oxygen vacancy formation at the metal/TiO_2 interface during ammonia borane hydrolysis: a study

of CuCo nanoparticles supported on various colored TiO_2 samples, New Journal of Chemistry, 49 (2025) 1982-1993.

[125] P. Wu, S. Tan, J. Moon, Z. Yan, V. Fung, N. Li, S.Z. Yang, Y. Cheng, C.W. Abney, Z. Wu, A. Savara, A.M. Momen, D.E. Jiang, D. Su, H. Li, W. Zhu, S. Dai, H. Zhu, Harnessing strong metal-support interactions via a reverse route, Nature Communications, 11 (2020) 3042.

[126] S.J. Tauster, S.C. Fung, R.L. Garten, Strong metal-support interactions. Group 8 noble metals supported on titanium dioxide, Journal of the American Chemical Society, 100 (1978) 170-175.

[127] P. Jing, T. Gan, H. Qi, B. Zheng, X. Chu, G. Yu, W. Yan, Y. Zou, W. Zhang, G. Liu, Synergism of Pt nanoparticles and iron oxide support for chemoselective hydrogenation of nitroarenes under mild conditions, Chinese Journal of Catalysis, 40 (2019) 214-222.

[128] A.A. Fernández-Andrade, J.A. Vergara, D. Gómez, D. González-Vera, C.H. Campos, J.M. Rodríguez-Díaz, L.E. Arteaga-Pérez, Exploring the bifunctional role of Pd/ZrO2-TiO2 in the production of secondary amines via reductive amination of furfural, Applied Catalysis A: General, 705 (2025) 120455.

[129] T.M. Bustamante, S. Bedoya, Y. Rodríguez-Aballi, D. Sanhueza-Rosales, J.N.D. de León, C.H. Campos, Enhanced ruthenium utilization via succinamic acid-functionalized SiO_2 supports for efficient hydrogen storage in toluene-based LOHC systems, Applied Catalysis A: General, 707 (2025) 120518.

[130] M.V. Morales, J.M. Conesa, A.J. Galvin, A. Guerrero-Ruiz, I. Rodríguez-Ramos, Selective hydrogenation reactions of 5-hydroxymethylfurfural over Cu and Ni catalysts in water: Effect of Cu and Ni combination and the reagent purity, Catalysis Today, 423 (2023) 114021.

[131] D. Nanda Gopala Krishna, R.P. George, J. Philip, Role of Oxygen Vacancy Formation Energy and Insulating Behavior in Darkening of White Amorphous TiO_2, The Journal of Physical Chemistry C, 125 (2021) 16136-16146.

[132] J.L. Di Wu, Xiaoning Zhao, Aidong Li, Yanfeng Chen, and Naiben Ming, Sequence of Events for the Formation of Titanate Nanotubes, Nanofibers, Nanowires, and Nanobelts, Chemestry of Materials, 18 (2005) 6.

[133] K. Lee, A. Mazare, P. Schmuki, One-dimensional titanium dioxide nanomaterials: nanotubes, Chemical Reviews, 114 (2014) 9385-9454.

[134] R. Dinamarca, R. Espinoza-González, C.H. Campos, G. Pecchi, Magnetic Fe_2O_3–SiO_2–MeO_2–Pt (Me = Ti, Sn, Ce) as Catalysts for the Selective Hydrogenation of Cinnamaldehyde. Effect of the Nature of the Metal Oxide, Materials, 2019, pp. 413.

[135] M. Machreki, T. Chouki, G. Tyuliev, M. Fanetti, M. Valant, D. Arcon, M. Pregelj, S. Emin, The Role of Lattice Defects on the Optical Properties of TiO_2 Nanotube Arrays for Synergistic Water Splitting, ACS Omega, 8 (2023) 33255-33265.

[136] L.L. Wanbiao Hu, Guangshe Li, Jian Meng and Wenming Tong, Synthesis of Titanate-Based Nanotubes for One-Dimensionally Confined Electrical Properties, The Journal of Physical Chemistry C, 113 (2009) 6.

[137] B. Abida, L. Chirchi, S. Baranton, T.W. Napporn, H. Kochkar, J.-M. Léger, A. Ghorbel, Preparation and characterization of Pt/TiO_2 nanotubes catalyst for methanol electro-oxidation, Applied Catalysis B: Environmental, 106 (2011) 609-615.

[138] M.M. Mohamed, M. Khairy, S. Eid, Activity and stability studies of titanates and titanate-carbon nanotubes supported Ag anode catalysts for direct methanol fuel cell, Journal of Power Sources, 304 (2016) 255-265.

[139] L. Qian, Z.-L. Du, S.-Y. Yang, Z.-S. Jin, Raman study of titania nanotube by soft chemical process, Journal of Molecular Structure, 749 (2005) 103-107.

[140] M. Giarola, A. Sanson, F. Monti, G. Mariotto, M. Bettinelli, A. Speghini, G. Salviulo, Vibrational dynamics of anatase TiO_2: Polarized Raman spectroscopy andab initiocalculations, Physical Review B, 81 (2010).

[141] B. Taudul, F. Tielens, M. Calatayud, On the Origin of Raman Activity in Anatase TiO_2 (Nano)Materials: An Ab Initio Investigation of Surface and Size Effects, Nanomaterials (Basel), 13 (2023).

[142] C. Molinet-Chinaglia, L. Piccolo, S. Loridant, Investigating the Dynamics of Pt/CeO_2 Catalysts at the Powder Agglomerate Scale by Combining In Situ Hyperspectral Raman Imaging and SEM-EDX Analysis, ChemCatChem, 15 (2023) e202300627.

[143] C.J.K. A.A.H. Wenyong Lin, I. E. Wachs, Probing Metal-Support Interactions under Oxidizing and Reducing Conditions: In Situ Raman and Infrared Spectroscopic and Scanning Transmission Electron Microscopic-X-ray Energy-Dispersive Spectroscopic Investigation of Supported Platinum Catalysts, Journal of Physics Chemistry C, 112 (2008) 10.

[144] J. Zheng, G. Ji, P. Zhang, X. Cao, B. Wang, L. Yu, Z.J. Xu, Facile Aluminum Reduction Synthesis of Blue TiO_2 with Oxygen Deficiency for Lithium-Ion Batteries, Chemistry, 21 (2015) 18309-18315.

[145] J.E.Y. Vinodkumar Etacheri, Bart M. Bartlett, Chemically Bonded TiO_2–Bronze Nanosheet/Reduced Graphene Oxide Hybrid for High-Power Lithium Ion Batteries, ACS Nano, 8 (2014) 9.

[146] A.G.A. Deanna C. Hurum, Kimberly A. Gray, Explaining the Enhanced Photocatalytic Activity of Degussa P25 Mixed-Phase TiO_2 Using EPR, Journal Of Physical Chemistry B, 107 (2003) 5.

[147] O. Al-Madanat, B.N. Nunes, Y. AlSalka, A. Hakki, M. Curti, A.O.T. Patrocinio, D.W. Bahnemann, Application of EPR Spectroscopy in TiO_2 and Nb_2O_5 Photocatalysis, Catalysts, 11 (2021).

[148] Y. AlSalka, O. Al-Madanat, M. Curti, A. Hakki, D.W. Bahnemann, Photocatalytic H_2 Evolution from Oxalic Acid: Effect of Cocatalysts and Carbon Dioxide Radical Anion on the Surface Charge Transfer Mechanisms, ACS Applied Energy Materials, 3 (2020) 6678-6691.

[149] E. Ivanova, M. Mihaylov, F. Thibault-Starzyk, M. Daturi, K. Hadjiivanov, FTIR spectroscopy study of CO and NO adsorption and co-adsorption on Pt/TiO_2, Journal of Molecular Catalysis A: Chemical, 274 (2007) 179-184.

[150] K.I. Hadjiivanov, G.N. Vayssilov, Characterization of oxide surfaces and zeolites by carbon monoxide as an IR probe molecule, Advances in Catalysis, Academic Press2002, pp. 307-511.

[151] P. Bazin, O. Saur, J.C. Lavalley, M. Daturi, G. Blanchard, FT-IR study of CO adsorption on Pt/CeO_2: characterisation and structural rearrangement of small Pt particles, Physical Chemistry Chemical Physics, 7 (2005) 187-194.

[152] M. Mihaylov, K. Chakarova, K. Hadjiivanov, O. Marie, M. Daturi, FTIR Spectroscopy Study of CO Adsorption on Pt−Na−Mordenite, Langmuir, 21 (2005) 11821-11828.

[153] J. Audevard, J. Navarro-Ruiz, V. Bernardin, Y. Tison, A. Corrias, I. Del Rosal, A. Favre-Réguillon, R. Philippe, I.C. Gerber, P. Serp, Adjustment of the Single Atom/Nanoparticle Ratio in Pd/CNT Catalysts for Phenylacetylene Selective Hydrogenation, ChemCatChem, 15 (2023) e202300036.

[154] L. Vanoye, B. Guicheret, C. Rivera-Cárcamo, R. Castro Contreras, C. de Bellefon, V. Meille, P. Serp, R. Philippe, A. Favre-Réguillon, Process intensification of the catalytic hydrogenation of squalene using a Pd/CNT catalyst combining nanoparticles and single atoms in a continuous flow reactor, Chemical Engineering Journal, 441 (2022).

[155] Y. Yu, X. Dong, P. Chen, Q. Geng, H. Wang, J. Li, Y. Zhou, F. Dong, Synergistic Effect of Cu Single Atoms and Au-Cu Alloy Nanoparticles on TiO_2 for Efficient CO2 Photoreduction, ACS Nano, 15 (2021) 14453-14464.

[156] M. Turáková, T. Salmi, K. Eränen, J. Wärnå, D.Y. Murzin, M. Králik, Liquid phase hydrogenation of nitrobenzene, Applied Catalysis A: General, 499 (2015) 66-76.

[157] H. Jiang, G. Yuan, Z. Cui, Z. Zhao, Z. Dong, J. Zhang, Y. Cong, X. Li, Effects of Support Types and Their Porosity Characteristics on the Catalytic Performance of Ni-Based Catalysts in Nitrobenzene Hydrogenation to Aniline, Industrial & Engineering Chemistry Research, 62 (2023) 13355-13367.

[158] J. Wang, Z. Yuan, R. Nie, Z. Hou, X. Zheng, Hydrogenation of Nitrobenzene to Aniline over Silica Gel Supported Nickel Catalysts, Industrial & Engineering Chemistry Research, 49 (2010) 4664-4669.

[159] F. Lu, K. Lu, G. Zhao, S. Zhou, B. He, Y. Zhang, J. Xu, Y. Li, X. Liu, L. Chen, A PtPdCoCuNi high-entropy alloy nanocatalyst for the hydrogenation of nitrobenzene, RSC Advances, 12 (2022) 19869-19874.

[160] J. Wu, L. Wang, S. Xu, Y. Cao, Z. Han, H. Li, Sequential hydrogenation of nitroaromatics to alicyclic amines via highly-dispersed Ru-Pd nanoparticles anchored on air-exfoliated C_3N_4 nanosheets, RSC Advances, 13 (2023) 2024-2035.

[161] D. Combita, P. Concepción, A. Corma, Gold catalysts for the synthesis of aromatic azocompounds from nitroaromatics in one step, Journal of Catalysis, 311 (2014) 339-349.

[162] A.L. Nuzhdin, I.A. Shchurova, M.V. Bukhtiyarova, E.Y. Gerasimov, A.V. Bukhtiyarov, S.V. Sysolyatin, G.A. Bukhtiyarova, Hydrogenation of Dinitrobenzenes to Corresponding Diamines Over Cu–Al Oxide Catalyst in a Flow Reactor, Catalysis Letters, 154 (2023) 295-302.

[163] E.V. Shuvalova, O.A. Kirichenko, L.M. Kustov, Nickel catalysis for hydrogenation of *p*-dinitrobenzene to *p*-phenylenediamine, Russian Chemical Bulletin, 66 (2017) 34-38.

[164] R.W. Layer, The Chemistry of Imines, Chemical Reviews, 63 (1963) 489-510.

[165] D. Ball, Kinetics of Consecutive Reactions: First Reaction, First-Order; Second Reaction, Zeroth Order, Journal of Chemical Education, 75 (1998) 917.

[166] T. Lee, S. Liou, H. Bai, Comparison of titania nanotubes and titanium dioxide as supports of low-temperature selective catalytic reduction catalysts under sulfur dioxide poisoning, Journal of the Air & Waste Management Association, 67 (2017) 292-305.

[167] A.S. Al-Dughaither, H. de Lasa, HZSM-5 Zeolites with Different SiO_2/Al_2O_3 Ratios. Characterization and NH_3 Desorption Kinetics, Industrial & Engineering Chemistry Research, 53 (2014) 15303-15316.

[168] A. García-Ortiz, J.D. Vidal, M.J. Climent, P. Concepción, A. Corma, S. Iborra, Chemicals from Biomass: Selective Synthesis of N-Substituted Furfuryl Amines by the One-Pot Direct Reductive Amination of Furanic Aldehydes, ACS Sustainable Chemistry & Engineering, 7 (2019) 6243-6250.

[169] A. Mermer, T. Keles, Y. Sirin, Recent studies of nitrogen containing heterocyclic compounds as novel antiviral agents: A review, Bioorganic Chemestry, 114 (2021) 105076.

[170] A.P. Taylor, R.P. Robinson, Y.M. Fobian, D.C. Blakemore, L.H. Jones, O. Fadeyi, Modern advances in heterocyclic chemistry in drug discovery, Organic & Biomolecular Chemistry, 14 (2016) 6611-6637.

[171] J.A. Anderson, F.K. Chong, C.H. Rochester, IR study of CO adsorption on Pt, Re and $Pt–Re/Al_2O_3$ catalysts before and after coking, Journal of Molecular Catalysis A: Chemical, 140 (1999) 65-80.

[172] D. Liu, G.-H. Que, Z.-X. Wang, Z.-F. Yan, In situ FT-IR study of CO and H_2 adsorption on a Pt/Al_2O_3 catalyst, Catalysis Today, 68 (2001) 155-160.

[173] A. Bourane, O. Dulaurent, D. Bianchi, Heats of Adsorption of Linear and Multibound Adsorbed CO Species on a Pt/Al_2O_3 Catalyst Using in Situ Infrared Spectroscopy under Adsorption Equilibrium, Journal of Catalysis, 196 (2000) 115-125.

[174] J. Pritchard, A. Ciftci, M.W.G.M. Verhoeven, E.J.M. Hensen, E.A. Pidko, Supported Pt-Re catalysts for the selective hydrogenation of methyl and ethyl esters to alcohols, Catalysis Today, 279 (2017) 10-18.

[175] S.-M. Wu, L. Wu, N. Denisov, Z. Badura, G. Zoppellaro, X.-Y. Yang, P. Schmuki, Pt Single Atoms on TiO_2 Can Catalyze Water Oxidation in Photoelectrochemical Experiments, Journal of the American Chemical Society, 146 (2024) 16363-16368.

[176] C.M. Pecoraro, H. Sopha, S. Wu, H. Kim, Y. Wang, J. Macak, M. Santamaria, P. Schmuki, Platinum single atoms on titania aid dye photodegradation whereas platinum nanoparticles do not, Nanoscale, (2025) 3949-3957.

[177] U. Diebold, The surface science of titanium dioxide, Surface Science Reports, 48 (2003) 53-229.

[178] M.S. Lazarus, T.K. Sham, X-ray photoelectron spectroscopy (XPS) studies of hydrogen reduced rutile (TiO_{2-x}) surfaces, Chemical Physics Letters, 92 (1982) 670-674.

[179] B. Bharti, S. Kumar, H.-N. Lee, R. Kumar, Formation of oxygen vacancies and Ti^{3+} state in TiO_2 thin film and enhanced optical properties by air plasma treatment, Scientific Reports, 6 (2016) 32355.

[180] Y. Zhu, D. Liu, M. Meng, H_2 spillover enhanced hydrogenation capability of TiO_2 used for photocatalytic splitting of water: a traditional phenomenon for new applications, Chemical Communications, 50 (2014) 6049-6051.

[181] G. Wang, H. Wang, Y. Ling, Y. Tang, X. Yang, R.C. Fitzmorris, C. Wang, J.Z. Zhang, Y. Li, Hydrogen-Treated TiO_2 Nanowire Arrays for Photoelectrochemical Water Splitting, Nano Letters, 11 (2011) 3026-3033.

[182] W. Zang, J. Lee, P. Tieu, X. Yan, G.W. Graham, I.C. Tran, P. Wang, P. Christopher, X. Pan, Distribution of Pt single atom coordination environments on anatase TiO_2 supports controls reactivity, Nat Commun, 15 (2024) 998.

[183] M.-J. Choi, H. Park, M.H. Engelhard, D. Li, P.V. Sushko, Y. Du, Reevaluation of XPS Pt 4f peak fitting: Ti 3s plasmon peak interference and Pt metallic peak asymmetry in $Pt@TiO_2$ system, Journal of Vacuum Science & Technology A, 42 (2024) 063209.

[184] D.J. Morgan, XPS insights: Asymmetric peak shapes in XPS, Surface and Interface Analysis, 55 (2023) 567-571.

[185] F.A. Stevie, C.L. Donley, Introduction to x-ray photoelectron spectroscopy, Journal of Vacuum Science & Technology A: Vacuum, Surfaces, and Films, 38 (2020) 063204.

[186] E.A. Kozlova, T.P. Lyubina, M.A. Nasalevich, A.V. Vorontsov, A.V. Miller, V.V. Kaichev, V.N. Parmon, Influence of the method of platinum deposition on activity and

stability of Pt/TiO_2 photocatalysts in the photocatalytic oxidation of dimethyl methylphosphonate, Catalysis Communications, 12 (2011) 597-601.

[187] M.M. Maronna, E.C. Kruissink, R.F. Parton, F. Soulimani, B.M. Weckhuysen, W.F. Hoelderich, Spectroscopic study on the active site of a SiO_2 supported niobia catalyst used for the gas-phase Beckmann rearrangement of cyclohexanone oxime to ε-caprolactam, Physical Chemistry Chemical Physics, 18 (2016) 22636-22646.

[188] Y. Cui, X. Zhou, Q. Sun, L. Shi, Vapor-phase synthesis of 3-methylindole from glycerol and aniline over zeolites-supported Cu-based catalysts, Journal of Molecular Catalysis A: Chemical, 378 (2013) 238-245.

[189] T. Nakayama, B. Uno, Electronic inductive and resonance effects of substituents on concerted two-proton-coupled electron transfer between electrogenerated superoxide and hydroquinone derivatives in N,N-dimethylformamide, Chemical Engineering Journal, 491 (2024).

[190] S. Li, X. Yang, L. Zhang, J. An, B. Cai, X. Wang, Effect of fluorine substituents on benzothiadiazole-based D–π–A′–π–A photosensitizers for dye-sensitized solar cells, RSC Advances, 10 (2020) 9203-9209.